University of Nevada, Reno

Informing Code-Compliant Site-Specific Infrastructure Seismic Evaluations with Physics-Based Simulated Ground Motions

A dissertation submitted in partial fulfillment of the
requirements for the degree of Doctor of Philosophy
in
Civil and Environmental Engineering

by
Pezhman Matinrad

Dr. Floriana Petrone / Dissertation Advisor

May 2024

THE GRADUATE SCHOOL

We recommend that the dissertation
prepared under our supervision by

Pezhman Matinrad

entitled

Informing Code-Compliant Site-Specific Infrastructure Seismic Evaluations with Physics-Based Simulated Ground Motions

be accepted in partial fulfillment of the
requirements for the degree of

Doctor of Philosophy

Floriana Petrone, Ph.D.
Advisor

David McCallen, Ph.D.
Committee Member

Keri Ryan, Ph.D.
Committee Member

Mohamed Moustafa, Ph.D.
Committee Member

John Louie, Ph.D.
Graduate School Representative

Markus Kemmelmeier, Ph.D., Dean
Graduate School

May, 2024

ABSTRACT

Site-specific code-compliant approaches for seismic design require the use of a suite of ground motions that are selected and scaled to a target spectrum for performing nonlinear time-history analyses. Suitable sets of ground-motion records shall be selected by appropriately considering the earthquake parameters controlling the hazard at the site, including magnitude, fault distance, tectonic regime, and impulsive character. When tasked with the design at sites residing in the vicinity of a major active fault with site conditions not well represented in the existing catalogs of records, engineers face the challenge of not having a sufficient number of motions. This has led design codes, including ASCE/SEI 7, to contemplate the possibility of supplementing the existing database of records with simulated ground motions. Physics-based ground-motion simulations that incorporate the characteristics of fault rupture, geological structure, and topography are therefore becoming a fundamental resource to support structural design and advance understanding of seismic risk. However, technical guidance on their correct use in engineering applications is yet to be defined. This research provides the technical basis to inform the utilization of simulated motions in code-compliant structural design procedures, with a focus on two aspects: the capability of simulations to enable ‘true’ site-specific structural assessments as compared to approaches relying on catalogs of historical records, and the implications of different methods for modeling soft sediments on the predicted structural responses (simulation-based vs semi-empirical). Results show that utilizing site-specific simulated ground motions that incorporate path, fault geometry, and site-condition effects as opposed to historical records in code-compliant approaches may lead to differences in the structural demands above a factor of 1.5. Such differences are highly spatially variable and difficult to predict. It is also demonstrated that the utilization of hybrid methods combining simulations and empirical factors may lead to significant misestimates of structural responses, requiring the implementation of processing methods specific to the geological characteristics of the domain of interest. Finally, evidence from these analyses is collectively utilized to develop a method for the selection of simulated motions targeting component-specific spectral amplitudes and variability at the site of interest. The analyses and findings of this work are demonstrated utilizing two and three-dimensional archetypal reinforced concrete buildings of different heights.

ACKNOWLEDGMENTS

I would like to express my deepest gratitude to all those who have supported me throughout the journey of completing my PhD dissertation. First and foremost, I am immensely thankful to my supervisor Dr. Floriana Petrone, whose consistent support, guidance, and encouragement have been invaluable. Her expertise and mentorship have not only shaped this dissertation but have also helped me grow and develop as a researcher. I am also grateful to my committee members for their insightful feedback, constructive criticism, and valuable suggestions, which have played a crucial role in improving the quality and rigor of my research. Their expertise and dedication to academic excellence have been instrumental in shaping this study. I extend my heartfelt appreciation to my family for their unconditional love, unwavering support, and endless encouragement throughout this journey. Their belief in me has been the foundation of my success. I am deeply grateful for their presence in my life, and I only wish I could have them close to me to share in this moment of achievement. I would also like to thank all my friends, colleagues, and everyone else who has supported me in various ways during this endeavor. Your encouragement, understanding, and positivity have kept me motivated and inspired me to persevere through challenges. I am truly blessed to have had such amazing support systems, and I am forever grateful for each and every person who has contributed to my journey.

Pezhman Matinrad

University of Nevada, Reno

May 2024

TABLE OF CONTENTS

1 Introduction 1

1.1 Background, Problem Statement, and Objectives 1

1.2 Dissertation Outline 3

1.3 Refereces 5

2 ASCE/SEI 7-compliant site-specific evaluation of the seismic demand posed to reinforced concrete buildings with real and simulated ground motions. 7

2.1 Introduction 8

2.2 Simulated Ground Motions 14

2.3 Building Models Archetypes 16

2.4 Analysis Method 18

2.5 Regional-Scale Maps 28

2.6 Ground-Motion Scale Factors 35

2.7 Localization of Maximum Demand Along The Building Height 37

2.8 Concluding Remarks And Future Work 39

3 ASSESSING THE IMPACT OF REGION SPECIFICITY ON RC BUILDINGS FRAGILITY WITH GROUND-MOTION SIMULATIONS 68

3.1 Introduction 69

3.2 Simulated Ground Motions and Building Structures 71

3.3 Ground-Motion Selection and Scaling 72

3.4 Damage States (DS) Definition and Data Regression 75

3.5 Fragility Functions 77

3.6 Conclusion 78

3.7 References 80

4 Effect of Soft Sediments Modeling on the Seismic Response of a 3D Mid-Rise RC Building: High-Resolution Physics-Based Ground-Motion Simulations versus Empirical Factors 88

4.1 Introduction 89

4.2 Ground-Motion Simulations 93

4.3 Empirical Ground-Motions Models and Simulated Ground-Motion Modification 97

4.4 Building Model 100

4.5 Ground-Motion Intensity Measure Estimates with Different Modelling Approaches 102

4.6 Structural Response at The Regional Scale 109

4.7 Concluding Remarks and Future Work 112

5 Simulated Ground-Motions Selection for Component-Specific Target Spectral Amplitude and Variability 144

5.1 Introduction 144

5.2 Simulated Ground Motions 146

5.3 Archetype Building Models 147

5.4 Six-step procedure for ground-motion selection... 148

5.4.1 Step 1: Determine the site-specific spectra. 150

5.4.2 Step 2: Compute the component-variability ratio (CVR). 150

5.4.3 Step 3. Derive the median and standard deviation of the component-specific target spectrum. 152

5.4.4 Step 4: Process simulated ground motions (if needed) 153

5.4.5 Step 5: Randomly select n sets of ground motions. 154

5.5 Structural Response 155

5.6 References 156

6 Conclusion 169

6.1 Key Observations and Concluding Remarks 169

6.2 Future Work 172

LIST OF TABLES

Table 2.1. Fundamental vibrational periods of the RC buildings. 52

Table 2.2. List of the records utilized for the building analyses at site D and pulse period (T_P) of the fault normal component. 52

Table 3.1. Defined four damage states based on PIDR.. 83

Table 5.1. Characteristics of the considered stations. 160

Table 5.2. Impulsive motions... 160

Table 5.3. Hazard disaggregation based on the NSHM Conterminous U.S. 2018. 161

LIST OF FIGURES

Figure 2.1. Slip distribution of the rupture models utilized to simulate eight M7 earthquake realizations (R1 through R8). The green star represents the location of the hypocenter (Adapted from Petrone et al., 2021 [18]). 53

Figure 2.2. (A) Distribution of the shallow shear-wave velocity (Vs30) in the San Francisco Bay Area computational domain across the stations considered in this study. This distribution follows the USGS 3D velocity model [21]. The black line represents the projection of the Hayward Fault. (B) Pseudo-acceleration spectra of the original (black) and processed (red) ground-motion record at two sample sites where Vs30 < 500-m/sec. 53

Figure 2.3. Workflow established to conduct the regional-scale analyses and compare structural demands as obtained from populations of real and simulated ground motions.54

Figure 2.4. MCE$_R$ design spectrum, real records and simulated motions scaled in the bandwidth 0.2T1 – 2T1 with T1 = 2.93-sec for two sites (A) Site C with $V_{s30,C}$ = 515-m/sec and (B) Site D with $V_{s30,D}$ = 195-m/sec. 55

Figure 2.5. Twenty-story building response statistics obtained from the two separate components of real and simulated motions at (A) site C and (B) site D. 56

Figure 2.6. Site C: MCE$_R$ design spectrum with scaled real and simulated ground motions for the two separate components (A) fault normal and (B) fault parallel. 56

Figure 2.7. Regional-scale map of the median PIDR for the three-story building in the fault normal component as obtained from the (A) real and (B) simulated ground motions. 57

Figure 2.8. Regional-scale map of the median PIDR for the three-story building in the fault parallel component as obtained from the (A) real and (B) simulated ground motions..... 58

Figure 2.9. Regional-scale maps of ρ (ratio of the structural demand obtained from the simulated motions to the structural demand obtained from the real record) for the three-story building in the (A) fault normal and (B) fault parallel component. 59

Figure 2.10. PSA of the two separate components of the real and simulated ground motions scaled with the scale factors obtained from the scaling performed on the RotD100 for the station right on the North tip of the fault: (A) fault normal and (B) fault parallel........... 60

Figure 2.11. Regional-scale map of the median PIDR for the twenty-story building in the fault normal component as obtained from the (A) real and (B) simulated ground motions. 61

Figure 2.12. Regional-scale map of the median PIDR for the twenty-story building in the fault parallel component as obtained from the (A) real and (B) simulated ground motions. 62

Figure 2.13. Displacement time-history of the fault parallel component of simulated motions at a site (A) ~2-km away from the fault and (B) 8-km away from the fault and real records at (C) ~2-km away from the fault and (B) 8-km away from the fault. 63

Figure 2.14. Regional-scale maps of ρ (ratio of the structural demand obtained from the simulated motions to the structural demand obtained from the real records) for the twenty-story building in the (A) fault normal and (B) fault parallel component. 64

Figure 2.15. Variation of mean scale factors applied to the real and simulated motions at each station as a function of distance for the (A) three-story and (B) twenty-story building. 65

Figure 2.16. Regional-scale maps showing the localization of the PIDR along the building height obtained from the fault normal component of the (A) real motions and (B) simulated motions. 66

Figure 2.17. Regional-scale maps showing the localization of the PIDR along the building height obtained from the fault parallel component of the (A) real motions and (B) simulated motions. 67

Figure 3.1. A) The computational domain over San Francisco Bay Area. B) Slip distribution of the rupture models and the hypocentre location for the eight realizations of the simulated ground motions. 84

Figure 3.2. Mean RotD50 spectral acceleration at the fundamental period of the 3-story building. A) Real ground motions B) Simulated ground motions. 84

Figure 3.3.3. Mean RotD50 spectral acceleration at the fundamental period of the 20-story building. A) Real ground motions B) Simulated ground motions. 85

Figure 3.3.4. PIDR versus $S_a(T_1)$ correlation for 3-Story building A) simulated ground motions FN. B) simulated ground motions FP. C) real records FN. D) real records FP. . 86

Figure 3.5. Fragility curves of real and simulated ground motions based on PIDR for 3-Story building considering 3 damage states A) Fault Normal. B) Fault Parallel. 87

Figure 3.6. Fragility curves of real and simulated ground motions based on PIDR for 20-Story building considering 3 damage states A) Fault Normal. B) Fault Parallel. 87

Figure 4.1. (A) 80-km x 120-km computational domain covering the San Francisco Bay Area: the black line represents the projection of the Hayward Fault; the green star indicates the location of the epicenter. (B) Rupture model: slip distribution in cm with the hypocenter indicated by the green star (top row); rise time in sec (middle row); 4-Hz slip rate in cm/sec (bottom row) across the 15-km x 60-km rupture plane. 124

Figure 4.2. Maps of the (A) Time-averaged shear wave velocity in the upper 30-m (Vs30) across the computational domain in m/sec; and (B) Depth to the 1.0-km/sec shear wave velocity (Z1.0) in km across the computational domain. Both parameters follow the USGS model (v.21.1, Aagaard & Hirakawa, 2021). The black line indicates the projection of the segment of the Hayward Fault considered in this study. 125

Figure 4.3. Comparison of simulated ground motions and the NGA-W2 ground-motion models for selected IMs. (A and B) PSA vs spectral periods; and (C and D) PGV vs distance, for the two separate components, FN and FP. 126

Figure 4.4. Velocity profiles obtained from the USGS velocity model (black), the USGS velocity model with a Vs, min of 250-m/sec (green) and a 500-m/sec (red) for two sites in the computational domain. (A) Santa Clara Valley; and (B) Pleasanton-Livermore Valley. The dotted lines represent the actual velocity profile, and the solid lines the velocity profile modeled in SW4. 127

Figure 4.5. Three-dimensional reinforced concrete 10-story building model. (A) Elevation view along the two principal directions, X and Y; (B) Plan view with a schematic of the building deformed shape; (C) Detail of the fiber section model adopted (beams and columns) and materials constitutive laws (steel and concrete). 128

Figure 4.6. Pseudo-Spectral Acceleration at T2 - PSA(T2). Maps for the fault normal component of the ground motions: simulation model with (A) Vs, min = 500-m/sec and (B) Vs, min = 250-m/sec; simulation model with Vs, min = 500-m/sec processed with (C) BSSA14 and (D) BA18 to obtain the same VS30 calculated with Vs, min = 250-m/sec. 129

Figure 4.7. Pseudo Spectral Acceleration ratios (R_{PSA}) of the fault normal component of the ground motions at the fundamental periods of vibration of the ten-story building (T1 = 1.7-sec and T2 = 1.5-sec): (A and D) PSA from the simulation model with Vs, min = 250-m/sec to the PSA from the simulation model with Vs, min = 500-m/sec; (B and E) PSA from the BSSA14 empirical model to the PSA from the simulation model with Vs, min = 500-m/sec; and (C and F) PSA from the BA18 empirical model to the PSA from the simulation model with Vs, min = 500-m/sec. 130

Figure 4.8. Peak Ground Velocity (PGV) maps for the fault normal component of the ground motions: (A) simulation model with Vs, min = 500-m/sec; (B) simulation model with Vs, min = 250-m/sec; (C) simulation model with Vs, min = 500-m/sec processed with BSSA14; and (D) simulation model with Vs, min = 500-m/sec processed with BA18. 131

Figure 4.9. Peak Ground Velocity ratios (R_{PGV}) for the fault normal component of the ground motions: (A) PGV from the simulation model with Vs, min = 250-m/sec to the PSA from the simulation model with Vs, min = 500-m/sec; (B) PGV from the BSSA14 empirical model to the PSA from the simulation model with Vs, min = 500-m/sec; and (C) PGV from the BA18 empirical model to the PSA from the simulation model with Vs, min = 500-m/sec. 132

Figure 4.10. Site in the Santa Clara Valley (SC) characterized by $Vs30_T$ = 250-m/sec, Z1.0 = 0.6-km and Rrup = 19.9-km. (A and C) PSA of the fault normal and fault parallel components; (B) empirical models' transfer functions accounting for both linear and nonlinear effects (blue and black solid lines) and linear effects only (blue and black dotted lines) and simulation models' transfer function (red solid line); (D) velocity time-histories of the fault normal and fault parallel components obtained from the different modeling approaches.. 133

Figure 4.11. Site in the Pleasanton-Livermore Valley (PL) characterized by $Vs30_T$ = 401-m/sec, Z1.0 = 1.46-km and Rrup = 21-km. (A and C) PSA of the fault normal and fault parallel components; (B) empirical models' transfer functions accounting for both linear and nonlinear effects (blue and black solid lines) and linear effects only (blue and black dotted lines) and simulation models' transfer function (red solid line); (D) velocity time-histories of the fault normal and fault parallel components obtained from the different modeling approaches. 134

Figure 4.12. Transfer functions obtained with the considered modeling approaches (RotD50). The thin lines represent the transfer function at each site, and the thick line the median across all sites with $\mathrm{VS30} < 500\ \mathrm{m/sec}$. Black and blue are used for the approach combining the simulations with $\mathrm{Vs,min}$ = 500-m/sec with the BSSA14 and BA18 empirical factors, respectively, and red for the purely simulation-based approach........ 135

Figure 4.13. Vs profiles of arrays of stations sampled on a 10-km grid at increasing distances from the fault (from ~0-km to ~10-km) obtained from the USGS seismic velocity model (Aagaard and Hirakawa, 2021). 136

Figure 4.14. Ten-story building response maps. PIDR obtained from the different methods to model the soft soil. (A) Simulations with $\mathrm{Vs,min}$= 500-m/sec; (B) Simulations with $\mathrm{Vs,min}$= 250-m/sec; (C) Simulations with $\mathrm{Vs,min}$= 500-m/sec processed with BSSA14; and (D) Simulations with $\mathrm{Vs,min}$= 500-m/sec processed with BA18. 137

Figure 4.15. Distribution of the PIDR along the building height and across all modeling approaches and for the sites with $VS30 < 500\ \mathrm{m/sec}$: response from single motion (thin lines), median and standard deviation (thick lines). 138

Figure 4.16. Ratio maps (R_{PIDR}) of the ten-story building response obtained from the different modeling methods. (A) $PIDR_{Sim250}/PIDR_{Sim500}$, (B) $PIDR_{BSSA14}/PIDR_{Sim500}$, (C) $PIDR_{BA18}/PIDR_{Sim500}$ 139

Figure 4.17. Map of torsion for the ten-story building. Peak torsion obtained from the different methods to model the soft soil. (A) Simulations with $\mathrm{Vs,min}$= 500-m/sec; (B) Simulations with $\mathrm{Vs,min}$= 250-m/sec; (C) Simulations with $\mathrm{Vs,min}$= 500-m/sec processed with BSSA14; and (D) Simulations with $\mathrm{Vs,min}$= 500-m/sec processed with BA18. .. 140

Figure 4.18. Pseudo-Spectral Acceleration at T1 - PSA(T1). Maps for the fault parallel component of the ground motions: simulation model with (A) $\mathrm{Vs,min}$ = 500-m/sec and (B) $\mathrm{Vs,min}$ = 250-m/sec; simulation model with $\mathrm{Vs,min}$ = 500-m/sec processed with (C) BSSA14 and (D) BA18 to obtain the same $VS30$ calculated with $\mathrm{Vs,min}$ = 250-m/sec. 141

Figure 4.19. Pseudo Spectral Acceleration ratios (R_{PSA}) of the fault parallel component of the ground motions at the fundamental periods of vibration of the ten-story building (T1 = 1.7-sec and T2 = 1.5-sec): (A and D) PSA from the simulation model with $\mathrm{Vs,min}$ = 250-

m/sec to the PSA from the simulation model with Vs, min = 500-m/sec; (B and E) PSA from the BSSA14 empirical model to the PSA from the simulation model with Vs, min = 500-m/sec; and (C and F) PSA from the BA18 empirical model to the PSA from the simulation model with Vs, min = 500-m/sec. 142

Figure 4.20. Peak Ground Velocity (PGV) maps for the fault parallel component of the ground motions: (A) simulation model with Vs, min = 500-m/sec; (B) simulation model with Vs, min = 250-m/sec; (C) simulation model with Vs, min = 500-m/sec processed with BSSA14; and (D) simulation model with Vs, min = 500-m/sec processed with BA18 . 143

Figure 5.1. 80-km x 120km computational domain covering San Francisco Bay Area: the red line determines the Hayward Fault and the considered stations for the ground motion selection analysis. 162

Figure 5.2. Slip distribution of the rupture models utilized for the twenty-five simulated realizations of a M7 earthquake. The green star indicates the location of the hypocenter. 163

Figure 5.3. PSA of the simulated motions from the twenty-five considered events against the four NGA-W2 ground-motion models. Fault parallel (left); fault normal (right). ... 163

Figure 5.4. Site-specific design spectra for the sites considered in this study. 164

Figure 5.5. Component-specific target spectrum versus the actual spectral acceleration of the simulated ground motions for A) site A, Event. B) site C, Event 2. C) site D, Event 19. 164

Figure 5.6. Component-specific target spectrum with calculated dispersion A) site A. B) site B. C) site C. D) Site D. E) Site E. 165

Figure 5.7. RotD100 of the original and processed simulated ground motions (single motions, median and standard deviation) across all sites. 166

Figure 5.8. Set of eleven selected ground motions (single motions, median and standard deviation, in red); Set of original ground motions (median and standard deviation, in black); component-specific target spectrum (median and standard deviation)........................... 167

Figure 5.9. Comparison of structural response between the selected ground motions and entire the population of the records. 168

1 INTRODUCTION

1.1 Background, Problem Statement, and Objectives

Ground-motion selection stands as a crucial step in structural seismic performance evaluations. Conventional approaches rely on selecting and scaling historical earthquake records to a spectrum targeting an event with a specific rate of occurrence. The existing standards for structural design recommend selecting the ground motions, ensuring they are consistent with the tectonic regime, magnitude, and distance to the fault of the considered site. However, historical data from large-magnitude earthquakes recorded in the proximity of the causative fault (<15 km) is scarce [1–3]. This leads to selecting suites of records that are not necessarily representative of the region of interest, with the effect of potentially introducing biases in the structural response predictions in terms of absolute demand and localization.

Recent research highlighted the limitation of using historical records alone and investigated the potential of simulated ground motions to fill these gaps. Sorensen and Lang [4], and Bruks et al. [5] demonstrated that simulated ground motions, which incorporate the propagation of the wave, physics of fault rupture, and site-specific conditions, can provide different assessment of structural response rather than real ground motions. Bijelic et al. [6] and McCallen et al (2021) [7,8] validated the efficacy of physics-based simulations in evaluating structural collapse risk and regional seismic demand, particularly in regions with complex geological characteristics, such as sedimentary basins.

Simulated ground motions obtained from physics-based wave propagation models have emerged as a powerful and promising resource to support earthquake engineering analyses and assessments. These models offer the ability to generate synthetic records for any conceivable scenario, including magnitude, faulting mechanism, and site conditions.

However, the execution of fully deterministic wave-propagation models still requires significant computational resources and remains tied to the utilization of high-performance computers. Techniques to optimize the mesh grid refinement and computational load of the analysis have been developed to consider both accuracy and efficiency in the physics-based model [9,10]. For instance, McCallen et al. [7,8] implemented a mesh refinement scheme in SW4 that adapts the computational grid size to the depth-dependent wavelength, enhancing the efficiency of large-scale simulations[11].

Also, the characteristics of simulated ground motions and thus their utilization in different engineering applications (long-span bridges, buildings, power plants, etc.), depend on the features of the models utilized to generate them, including frequency resolution and minimum shear-wave velocity. A full understanding of these aspects is essential for structural engineers to ensure the correct use of synthetic motions in civil engineering applications. Nevertheless, technical guidance on the utilization of simulated ground motions in structural performance assessments is yet to be developed.

In this context, this research aims to identify some of the key features of the simulation models and resulting ground motions that can most largely affect structural responses. A suite of M7 Hayward Fault strike-slip earthquakes simulated in the San Francisco Bay Area and three archetypal reinforced concrete special moment resisting frame buildings are utilized as case study. The work presented in this dissertation focuses on the following specific objectives:

Objective No.1: evaluate the differences introduced by the use of site-specific simulated records as opposed to historical records in ASCE/SEI 7-compliant seismic structural assessments and identify the ground-motion features primarily driving such differences to better inform ground-motion selection.

Objective No.2: identify the implications of different soft sediment modeling approaches on structural performance predictions. Specifically, two approaches are investigated: one relying on the use of physics-based wave-propagation models that can resolve minimum shear wave velocities typical of sedimentary basins and soft sediments, and one that combines simulated ground motions obtained from models that resolve high(er) shear-wave velocities with empirical correction factors.

Objective No.3: propose a method for selecting simulated ground motions, targeting (i) spectral amplitudes, (ii) spectral variability, and (iii) component-specificity once a large population of simulated records is available.

1.2 Dissertation Outline

This dissertation includes six chapters, four of which are standalone papers. Chapter 1 provides an overview of the background, problem statement, objectives, and outline of the dissertation. Chapter 2 presents a comprehensive assessment of the difference introduced by the use of simulated and real ground motions when following ASCE/SEI-compliant methods. This chapter of the dissertation was published in the Earthquake Engineering and Structural Dynamics journal in August 2023.

Chapter 3 takes a step forward and analyzes the impact of region specificity on reinforced concrete buildings' fragility. This chapter of the dissertation is a standalone paper accepted to be published in the 18th World Conference of Earthquake Engineering (WCEE2024) Proceedings (July 2024).

Chapter 4 investigates the effects of soft soil sediment modeling approaches and evaluates alternate solutions for incorporating the effects of soft sediments into simulated ground motions that resolve higher shear wave velocities. This Chapter of the dissertation is a standalone paper currently under review in the Earthquake Spectra journal. The revision of this paper was submitted to the journal, and it is waiting for the final decision.

Chapter 5 utilizes the evidence from the work described in the previous chapters to develop a selection method for simulated ground motions that concurrently accounts for hazard-informed target amplitudes, variability, and component specificity. This chapter of the dissertation is a standalone paper ready to be submitted to the Earthquake Engineering and Structural Dynamics journal.

Finally, Chapter 6 offers a summary of the main research findings.

All the research papers have Pezhman Matinrad and Dr. Floriana Petrone as co-authors.

1.3 Refereces

1. Smerzini C, Amendola C, Paolucci R, Bazrafshan A. Engineering validation of BB-SPEEDset, a data set of near-source physics-based simulated accelerograms. *Earthquake Spectra* 2023; **40**(1): 420–445. DOI: 10.1177/87552930231206766.

2. Petrone F, Abrahamson N, McCallen D, Pitarka A, Rodgers A. Engineering evaluation of the EQSIM simulated ground-motion database: The San Francisco Bay Area region. *Earthquake Engineering & Structural Dynamics* 2021; **50**(15): 3939–3961.

3. ASCE/SEI 7-22. *Minimum Design Loads and Associated Criteria for Buildings and Other Structures*. ASCE/SEI 7. American Society of Civil Engineers; 2021. DOI: 10.1061/9780784415788.

4. Sørensen MB, Lang DH. Incorporating Simulated Ground Motion in Seismic Risk Assessment: Application to the Lower Indian Himalayas. *Earthquake Spectra* 2015; **31**(1): 71–95. DOI: 10.1193/010412EQS001M.

5. Burks LS, Zimmerman RB, Baker JW. Evaluation of hybrid broadband ground motion simulations for response history analysis and design. *Earthquake Spectra* 2015; **31**(3): 1691–1710.

6. Bijelić N, Lin T, Deierlein GG. Quantification of the influence of deep basin effects on structural collapse using SCEC CyberShake earthquake ground motion simulations. *Earthquake Spectra* 2019; **35**(4): 1845–1864.

7. McCallen D, Petrone F, Miah M, Pitarka A, Rodgers A, Abrahamson N. EQSIM—A multidisciplinary framework for fault-to-structure earthquake simulations on exascale computers, part II: Regional simulations of building response. *Earthquake Spectra* 2021; **37**(2): 736–761. DOI: 10.1177/8755293020970980.

8. McCallen D, Petersson A, Rodgers A, Pitarka A, Miah M, Petrone F, *et al.* EQSIM—A multidisciplinary framework for fault-to-structure earthquake simulations on exascale computers part I: Computational models and workflow. *Earthquake Spectra* 2021; **37**(2): 707–735. DOI: 10.1177/8755293020970982.

9. Taborda R, López J, Karaoglu H, Urbanic J, Bielak J. Speeding up finite element wave propagation for large-scale earthquake simulations. *Parallel Data Laboratory Tech Rept CMUPDL* 2010; **10**: 109.

10. Bao H, Bielak J, Ghattas O, Kallivokas LF, O'hallaron DR, Shewchuk JR, *et al.* Earthquake ground motion modeling on parallel computers. *Proceedings of the 1996 ACM/IEEE conference on Supercomputing*, 1996.

11. Sjögreen B, Petersson NA. A fourth order accurate finite difference scheme for the elastic wave equation in second order formulation. *Journal of Scientific Computing* 2012; **52**: 17–48.

2 ASCE/SEI 7-COMPLIANT SITE-SPECIFIC EVALUATION OF THE SEISMIC DEMAND POSED TO REINFORCED CONCRETE BUILDINGS WITH REAL AND SIMULATED GROUND MOTIONS.

This chapter of the dissertation is published in the journal of Earthquake Engineering and Structural Dynamics in 2023.

Abstract

State-of-the-art seismic design and assessment methodologies rely on the utilization of ground-motion records scaled to site-specific risk-targeted spectra to perform nonlinear time-history analyses and estimate mean structural demands. Motivated by the discrepancies in structural response estimates resulting from different selection and scaling methods, this study assesses the implications of utilizing site-specific simulated ground motions from 3-D physics-based wave-propagation models as opposed to historical records from worldwide catalogs in ASCE/SEI7-compliant procedures for seismic performance evaluations. A suite of validated realizations of an M7 Hayward Fault earthquake in the San Francisco Bay Area and two modern reinforced concrete moment-resisting frame buildings are utilized as a case study. The 2014 USGS earthquake hazard and probability maps are employed for the hazard calculations, and the PEER NGA-West2 database is used for the selection of the real ground motions. The building models are coupled with the simulated and real ground motions to perform a total of 30,552 nonlinear time-history analyses. Structural demands obtained from real and simulated motions are examined and compared at the regional-scale in terms of peak interstory drift ratio median and dispersion, and localization along the building height. The correlations between observed structural responses and ground-motion features are discussed to potentially inform current code-compliant methodologies for ground-motion selection. Results show that utilizing site-specific simulated ground motions that incorporate path, fault geometry, and site-condition effects as opposed to historical ground-motion records may lead to differences in the structural demands above 50%. Such differences are highly spatially variable throughout the region and difficult to predict.

Keywords: simulated ground motions, ground-motion selection, site-specific seismic demand assessment, reinforced concrete buildings, ASCE/SEI 7-compliant design, regional-scale analyses

2.1 Introduction

Current site-specific procedures for seismic assessment and design are based on the selection and scaling of a set of ground motions to an intensity measure (usually spectral acceleration) associated with a predefined target hazard to carry out nonlinear time-history analyses (NLTHA).

The selection of the ground-motion records is conventionally conducted using one (or more) catalogs available to the researchers and practitioners' communities, such as the PEER NGA-West 2 [1], the K-NET, KiK-net [2], or the NESS2.0, which is explicitly devoted to establishing datasets of near-source recordings from moderate-to-strong earthquakes and providing a broader basis to select records and constrain empirical models [3]. Yet, while for small-to-medium magnitude earthquakes (<M6.5) at medium-to-long distances (>15-km) a rich population of records is available for selection and utilization with moderate or potentially no scaling, the analysis of buildings at sites located in the near-field of active faults capable of large magnitude earthquakes is still challenged by the scarcity of records. This issue becomes even more critical when interested in assessing structural risk in areas of high seismicity, where large earthquakes are expected, but records from consistent historical events are not available.

In recent years, deterministic physics-based wave propagation models have advanced rapidly gaining recognition for their potential to supplement empirical data. There are conceptual benefits associated with the utilization of simulated ground motions that go beyond the need to augment empirical data. Earthquake simulation models, in fact, are able to incorporate the fundamentals of physics of earthquake fault rupture, wave propagation, and local surficial site response, thus allowing to evaluate structural response in a more reliable manner and capture the site specificity of the demand posed to the built environment.

A number of studies have investigated the distribution of the seismic risk posed to various types of structures with the use of ground-motion simulations. This was motivated by a twofold objective: validating the simulated motions for use in engineering domain and providing insight into the parameters that have the largest effect on structural response with effect on loss and damage estimates at the regional scale. For example, Sørensen and Lang [3] investigated the implications of utilizing stochastic finite fault ground-motion simulations in earthquake damage and loss estimates, as opposed to the use of ground-motion prediction equations. The city of Dehradun and several scenarios incorporating different magnitude, distance, and azimuth to the source were utilized as a case study. Evidence from their analyses show differences in loss predictions and variability from the two methods, particularly in the near-field and in the direction of rupture propagation. Burks et al. [4] utilized hybrid broadband simulated motions and real records as an input for a three-dimensional building located in Berkeley (CA), with the objective to perform a comparison of building performance as obtained from the two sets of accelerograms and validate the simulated motions for use in ASCE 7-compliant [5-6] procedures. Results show that most of the differences in the structural response can be attributed to differences in the ground-motion directionality and that simulations can be reliably used if they realistically reproduce the ground-motion characteristics outlined in the ASCE 7. Smerzini and Pitilakis [7] carried out a simulation-based urban-scale seismic risk assessment adopting the city of Thessaloniki (Greece) and the 1978 M6.5 as a case study, in which contemporary RC buildings are represented through spectral displacement fragility functions. The study demonstrates the capability of ground-motion simulations to realistically reproduce spatial correlation and predict structural damage. Further studies have been carried out to fully leverage the potential of earthquake simulations to analyze ground motion and structural response sensitivities to the geology structure and radiation pattern. For example, Bijelić et al. [8] utilized physics-based earthquake simulations to assess the effects of deep basin on the structural collapse of different reinforced concrete (RC) structural systems in the Los Angeles area. Results from nonlinear time-history analyses carried out with spectrum and significant duration equivalent basin and non-basin simulated motions show an increase of the risk collapse by 20%. Bijelić et al. [9] utilized ~500,000 CyberShake unscaled simulated ground motions to examine the collapse risk posed to a 20-story building at four sites in the Los Angeles basin and compared results with the classical approach based on the use of recorded motions and probabilistic seismic hazard assessment. They demonstrate that the two approaches give similar estimates of the probability of collapse except for deep basin sites, where the simulation-based probability of collapse is about seven times larger than that predicted by the conventional approach. McCallen et al. [10] utilized broadband motions generated by a M7 strike-slip earthquake over a canonical rock-basin domain to analyze the regional variability and spatial distribution of seismic demand posed to a set of steel moment-resisting frame buildings. Results show the unique capability of simulated motions to capture the site specificity of the risk posed to infrastructure and augment the sparse empirical data near large earthquake sources. Zhong et al. [11] employed broadband simulated ground motions to perform nonlinear time-history analyses of two archetypal tall buildings located in San Francisco, Los Angeles, and San Bernardino. They find that utilizing simulated ground motions can address issues related to scaling, unrealistic spectral shapes, and over conservative spectral variations. Antonietti et al. [12] coupled 3D physics-based earthquake simulations with fragility functions of high-rise buildings for seismic risk estimates, utilizing the metropolitan area of Beijing as a case study. Results show that the simulation-based estimate of the risk has systematic differences when compared with the risk obtained from the use of ground-motion models, particularly in the near-field.

Although the aforementioned studies provide an extensive overview of the potential uses of simulated ground motions in engineering domains and the associated limitations, they mainly focus on a restricted number of sites and earthquake realizations.

Motivated by the possibility contemplated by the ASCE/SEI 7 [5-6] to augment ground-motion records with simulations when enough real ground motions are not available and by the discrepancies in structural response estimates resulting from different selection methods [13], this work evaluates the implications of utilizing site-specific simulated ground motions as opposed to catalogs of historical records in structural assessments at the regional scale. The study utilizes simulated ground motions from multiple realizations of a not-historical earthquake scenario (an M7 Hayward Fault strike-slip earthquake) for a region in which historical motions that would support the selection of records to perform nonlinear time-history (NLTH) analyses are not available (San Francisco Bay Area).

Evidence from the study presented in this paper aims at providing preliminary answers to the following questions: (1) how different is the demand posed to RC building archetypes residing in the San Francisco Bay Area when this is evaluated with conventional methods relying on the use of worldwide historical records or with site-specific motions that incorporate path, fault geometry, and site-condition effects? (2) at what site conditions and distances such differences become larger? (3) what site-specific ground-motion features influence such differences?

Comparisons are carried out on the structural demands obtained from simulated and real motions scaled to a design spectrum obtained from the target hazard level equivalent to 1%

probability of collapse in 50 years at each site in the domain. Ground motions from eight realizations of a M7 Hayward Fault strike-slip earthquake performed over an 80-km x 30-km region in the San Francisco Bay Area generated within the EQSIM computational platform [14] are utilized in combination with detailed structural models of modern three-story and twenty-story RC moment-resisting frame buildings to evaluate structural performance. These buildings are selected to span structural typologies whose dynamic behavior is controlled either by the first fundamental mode of vibration or by a combination of fundamental and higher modes exhibiting high sensitivity to ground-motion long-period features. A total of 30,552 nonlinear time-history analyses are executed over 402 stations, thus providing a statistical basis for a comprehensive comparison of structural performance. Results are shown for the mainland stations only. The demand is herein evaluated in terms of mean and dispersion (i.e., standard deviation) of peak interstory drift ratio (PIDR) and its location along the building height. This is motivated by the fact that the interstory drift is a fundamental engineering parameter utilized in many building codes to quantify structural seismic performance (e.g., ASCE 43-19 [15]).

Results from the regional-scale analyses show differences that attain peaks as large as 50% (or above for selected sites), as either overestimate or underestimate in the median demand. Such differences are markedly site-specific both East and West of the fault and difficult to predict. As expected, the variability of the demand is larger for the historical records than for the simulated motions, with few exceptions, and strongly influenced by motions that incorporate forward-directivity and fling-step effects for the twenty-story building structure.

2.2 Simulated Ground Motions

Eight realizations of an M7 Hayward Fault strike-slip faulting mechanism event were utilized to simulate fully deterministic earthquake ground motions over an 80-km x 30-km x 20-km computational domain encompassing the San Francisco Bay Area. The eight realizations considered in this study differ from each other for the characteristics of the kinematic rupture model, including slip distribution, hypocenter location, and properties of the deterministic large-slip patches (i.e., distribution of the slip within each patch and their location in the rupture plane) [16-17]. Figure **2.1** provides a representation of the slip distribution of the rupture models utilized in the simulations. A description of the fault rupture model properties and their effect on multiple building response proxies can be found in [18], and the presentation of the methodology utilized to evaluate the motions in [19]. Specifically, the motions were validated in terms of median predictions against real ground motions consistent with the simulated scenario and empirical ground-motion models with respect to multiple intensity measures and building response proxies, including pseudo-spectral acceleration (PSA), ground-motion duration, polarization, and inter-period correlation. This suite of realizations provides an initial, yet partial, estimate of the ground-motion aleatory variability expected for an M7 Hayward Fault strike-slip event in the San Francisco Bay Area.

The ground-motion simulations were executed in SW4 (Seismic Waves, fourth order) [20] to resolve frequencies up to 5-Hz with a minimum shear-wave velocity of 500-m/sec. The two horizontal components of the ground motions were recorded and stored on a 2-km grid over the domain surface, leading to a total of 39 x 14 x 8 x 2 = 8,736 simulated time histories (mainland and water) resolved in the components normal and parallel to the fault. The vertical component, while available from the simulations, was not considered in this study.

The computational domain utilizes the USGS 3D velocity model [21] with topography to represent the geology structure of the modeled area. Figure **2.2**-A shows the distribution of the shallow shear wave velocity (Vs30) across the stations of the computational domain where the motions are sampled. The values of Vs30 span across a wide range of speeds, from a minimum of 110-m/sec to a maximum of 3,500-m/sec. To properly represent the features of the motions at sites located on basins with a Vs30 < 500-m/sec, empirical site-correction factors were utilized. These factors are based on the 30-m travel time averaged shear-wave speed at the site of interest as implemented in the ground-motion model of Boore et al. [22], and account for both the linear and nonlinear component of site amplification.

As an example, Figure **2.2**-B shows the 5% damping PSA of the original and processed maximum direction (RotD100) ground motions for two near-field sites (A and B) West of the Hayward Fault. Site A is characterized by a Vs30 = 141-m/sec, and site B by Vs30 = 160-m/sec. At both sites, the softer soil produces an amplification of the PSA amplitudes at long periods caused by soft near-surface sediment effects and a deamplification at short periods caused by a combination of nonlinear site effects and increased damping. Altogether, such effects are expected to affect the response of both the stiff three-story and flexible twenty-story buildings. Given the distribution of the Vs30 across San Francisco

Bay Area region and the cap of 500-m/sec in the computational domain, the site-correction factors were applied to about 64% of the stations (across the entire domain).

2.3 Building Models Archetypes

Two three-dimensional RC buildings were designed to meet the requirements of the ASCE/SEI 7-16 [5] and ACI318-19 [24] specifications and utilized as archetypal structures in this investigation. One three-story building, representative of a stiff structure, and one twenty-story building, representative of a flexible structure, were selected. Special moment-resisting frames were utilized as the lateral force resisting system in the two orthogonal directions for both the internal and external frames. For design purposes, it was assumed that the structures are located West of the Hayward Fault in the San Francisco Bay Area, at a near-field site that is about 2-km away from the fault and is characterized by a Vs30 = 290-m/sec, corresponding to site class D. The site-specific risk-targeted maximum considered earthquake (MCE_R) response spectrum was derived considering the following parameters: risk category II, Cs = 0.051, Ie = 1.0, R = 8, Cd = 5.5, and $\Omega_0 = 3$, TL =8, yielding the spectral acceleration parameters $S_{M1} = 1.65$ $S_{MS} = 1.85$.

The two buildings are characterized by the same layout in plan and elevation. In plan, the 5 bays in the X-direction have a width of 8-m, and the 6 bays in the Y-direction a width of 5-m. In elevation, the first-story height is 4.5-m, and the typical-story height is 3.7-m. The structures utilize concrete with compressive strength of 50-MPa and reinforcing steel with a yield strength of 413-MPa. Table **2.1** lists the first three fundamental vibrational modes in the two horizontal directions for both buildings and the cumulative modal mass participation ratios.

Although the design was carried out on three-dimensional models, the analyses presented in this paper were conducted on two-dimensional frames taken from the original three-dimensional structures. Specifically, for each building, two-dimensional nonlinear models of a typical internal frame in the X-direction were developed in the OpenSees 3.3.0 platform [25]. While the resolution of the simulations (5-Hz) may not fully capture the energy content and richness at frequencies corresponding to the second mode of vibration of the three-story building (4.8-Hz), material softening and degradation occurring under strong motions lead to an elongation of the fundamental periods, towards frequencies that are fully resolved in the simulations. Overall, the limited contribution of the higher modes to the response of a stiff structure and its nonlinear behavior introduce negligible approximations in the response estimates of the three-story building utilized in this study. The models employ elastic elements with concentrated rotational springs with assigned nonlinear moment-curvature relationships. The modified Ibarra-Medina-Krawinkler Ibarra deterioration model [26] with peak-oriented hysteretic response (IMK in OpenSees) was utilized to simulate the plastic hinge rotation capacity and cyclic deterioration. The values of the IMK model parameters were computed utilizing the equations proposed by [27], which are based on regression analysis of RC columns failing in flexure and shear-flexural. The simulations incorporate P-Delta effects. This modeling approach is capable of capturing the fundamental modes of deterioration from initial damage to sidesway collapse. The models are fixed at the base.

2.4 Analysis Method

The objective of this study is to assess the differences in the structural response at the regional-scale as obtained from ASCE 7-compliant procedures that utilize either historical ground-motion records from worldwide catalogs or site-specific simulated motions that incorporate path, fault geometry, and site-condition effects, to eventually provide guidance on the use of simulated ground motions. To this aim, an integrated computational framework was developed in Python [28] and MATLAB [29], as shown in Figure **2.3**, which queries and links data from multiple sources, including USGS [30], PEER NGA-W2 [1], OpenSees [25], and EQSIM [14].

The analysis starts with the selection of the latitude and longitude of site i (with $i = 1,2 \ldots 402$, corresponding to the mainland stations only) in the computational domain, and is followed by the calculation of the shallow shear-wave velocity $V_{S30,i}$ at the site, and the computation of the risk-targeted maximum considered earthquake spectrum (MCE$_R$), target and design. The design spectrum is calculated as 2/3 of the target spectrum. Then, the workflow bifurcates into two branches depending on whether real (left) or simulated (right) motions are utilized, and ends with the calculation of ρ, representing the ratio of the maximum of the median demand from simulated motions to the maximum of the median demand from real motions. For sites of class A, B or C, the MCE$_R$ spectral parameters are obtained directly from the USGS online maps [31], corresponding to a collapse risk of 1% in 50 years; while for sites of class D, E and F the target spectrum is calculated as the lesser of the deterministic and probabilistic ground motions.

Starting from the real accelerograms (left branch of the flowchart), for each site i the seismic-hazard deaggregation is performed with the USGS Unified Hazard Tool [30] and the results are utilized to center the range of variation of the magnitude (M_w) and rupture distance (R_{rup}) employed as search parameters to query the PEER NGA-West2 database [1]. The following search criteria are employed: $M_{w,l/u} = M_{w,i} \mp 1$, where $M_{w,l/u}$ are the lower and upper bounds for the search and $M_{w,i}$ is the magnitude of the event controlling the hazard at site i; $R_{rup,l/u} = [0, R_{rup,i} + 10\ km]$, where $R_{rup,l/u}$ are the lower an upper bounds for the search, and $R_{rup,i}$ is the rupture distance obtained from the hazard deaggregation; and $V_{S30,l/u} = V_{S30,i} \mp 150\ m/sec$, where $V_{S30,l/u}$ are the lower and upper bounds for the search, and $V_{S30,i}$ is the shallow shear-wave velocity calculated in the previous steps.

Once a set of *n* pairs of motions is identified based on the search criteria defined above, the two horizontal components (H1 and H2) are utilized to calculate the maximum-direction spectrum (RotD100). The RotD100 spectra are then scaled to the $\mathrm{MCE}_{\mathrm{R,i}}$ design spectrum in the 0.2T1-2T1 spectral-period bandwidth, with T1 being the fundamental period of the structure under consideration. The upper and lower bounds of this range comprise the higher modes contributing to the building dynamic response and the potential elongation of the fundamental period caused by post-peak softening and reduced effective stiffness.

The final set of k motions (with $k = 11$, corresponding to the minimum number of ground motions according to the ASCE/SEI 7 provisions [5-6]) is selected based on the minimum error observed in approaching the design spectrum in the 0.2T1-2T1 bandwidth and by limiting the number of motions from each earthquake to two. While it is acknowledged that this criterion may not necessarily ensure the sought variability in the selected set of ground motions, it was still deemed appropriate to prevent biases in the final dataset when a visual inspection for the set of motions at each site was not practically possible. This is particularly relevant to near-field motions from large magnitude events, where the datasets of available records tend to be dominated by large arrays of motions recorded, for example, during the Chi-Chi (Taiwan) earthquake in 1999. Considerations on the expected number of motions with impulsive character for pulse periods relevant to the response of the twenty-story building are also incorporated into the search criteria. The model proposed by [32] is utilized. Finally, the maximum scale factor is limited to 10 [33]. However, while this was set up as an upper bound for the selection of the final set of motion, peak values up to about 6 were utilized (see also Figure **2.15**).

The error in matching the design spectrum is calculated as $Err = \sum_{j=1}^{n}\left(ln\left[PSA_{rec}\left(T_j\right)\right] - ln\left[PSA_{MCER}\left(T_j\right)\right]\right)^2$ [34], where $PSA_{rec}\left(T_j\right)$ is the pseudo-spectral acceleration of the n^{th} considered real record at period j, and $PSA_{MCER}\left(T_j\right)$ is the pseudo-spectral acceleration of the MCE$_R$ spectrum at period j. Once the k motions are identified, the two horizontal components of the ground motions (H1 and H2) are rotated to obtain the fault normal and fault parallel components utilizing the equations in [35], that is: $a_{FP} = a_1 \cos(\beta_1) + a_2 \cos(\beta_2)$ and $a_{FN} = a_1 \sin(\beta_1) + a_2 \sin(\beta_2)$, where a_{FP} and a_{FN} are the acceleration time-histories in the fault parallel and fault normal directions, a_1 and a_2 are the accelerations in the original directions, $\beta_1 = \alpha_{strike} - \alpha_1$, and $\beta_2 = \alpha_{strike} - \alpha_2$, with

α_{strike} being the strike of the fault, and α_1 and α_2 the azimuths of the instrument axes. In this work, the NGA-West2 flat-files were utilized to obtain a_{strike}, α_1, and α_2.

The scaled and rotated motions are imported into OpenSees to perform NLTH analyses with the structure under consideration (i.e., the structure with fundamental period T1 that was utilized to scale the ground motions) in the fault normal and fault parallel directions, separately. The engineering demand parameters (EDPs) of interest are recorded and stored. The EDPs considered in this study are the PIDR and the peak floor acceleration. However, any other metrics of interest could be incorporated in the same workflow.

For the sake of conciseness, only the results obtained with the PIDR are presented in this paper. Once the PIDR envelopes are derived (i.e., the PIDR obtained at each floor level throughout the entire time history) for each motion *k* and each component (fault normal and parallel), the lognormal mean and standard deviation at each story *m* are calculated across the k motions. Median and standard deviation are referred to as $(\mu_{lnPIDR})_{R,i,Fx,m}$ and $(\sigma_{lnPIDR})_{R,i,Fx,m}$, respectively, where *R* stands for real ground motion, *i* indicates the station where the calculation is performed, *Fx* is the ground-motion component (either fault normal, FN or fault parallel, FP), and *m* is the story number. Once this process is repeated for all the stations of the computational domain (*i = 1,2…402*) and for the two components of the motion, a total of 402 x 2 = 804 envelopes of median and corresponding standard deviation of the PIDR are obtained.

As for the simulated motions (right branch of the flowchart), the RotD100 is calculated for each (site-specific) pair *j* of fault normal and fault parallel motions (with *j = 1,2…8*, corresponding to the number of earthquake realizations available in this study) and scaled to the site-specific $MCE_{R,i}$ design spectrum (the same calculated earlier in the workflow and utilized to scale the real motions) in the spectral-period bandwidth 0.2T1-2T1 specific to the structure under consideration. It should be mentioned that, whenever possible, scaling the simulated motions should be avoided to preserve the true site-specific character of the motions. In this study, although the seismic hazard at most of the sites in the computational domain represented in Figure **2.2** is controlled by Hayward Fault earthquakes with M>7 or, for sites closer to the Western edge of the domain, by San Andreas Fault earthquakes with magnitude M>7, only realizations of a M7 Hayward Fault strike-slip event were available. For this reason, the simulated ground motions, yet being site-specific, were scaled. A discussion on the scale factors applied to real and simulated motions is presented in a separate section of this paper. It will be a long-term objective of this type of analysis to sample the final set of simulated motions (11 or more) across populations of simulated motions that cover a wide range of earthquake scenarios and realizations (including perturbations to the fault rupture model, faulting mechanism, magnitude, etc.) relevant to the sites under consideration. It is envisioned that if $j>11$, an approach similar to that employed for the selection of the final set of real motions can be utilized.

Once scaled, the fault normal and fault parallel components of the motions are imported into OpenSees to carry out NLTH analyses, the EDPs time-histories (PIDR in this case) are recorded and stored at all floors, and the lognormal mean $(\mu_{lnPIDR})_{S,i,Fx,m}$ and standard deviation $(\sigma_{lnPIDR})_{S,i,Fx,m}$ of the PIDR envelopes across the j realizations are computed.

The meaning of the subscripts in the median and standard deviation remains the same as described above, with the only difference that S here stands for simulated ground motions. This process is then repeated across all *i* stations of the computational domain and for the two separate components of the ground motions, yielding a total of 402 x 2 = 804 envelopes of median and corresponding standard deviation of the PIDR.

The differences in the structural response as obtained from real and simulated ground motions is expressed as function of ρ for the two separate components:

$$\rho_{Fx,i} = \frac{\max\left[\exp\left(\mu_{lnPIDR}\right)_{S,i,Fx,m}\right]}{\max\left[\exp\left(\mu_{lnPIDR}\right)_{R,i,Fx,m}\right]} \tag{1}$$

where $\max\left[\exp(\mu_{lnPIDR})_{S,Fx,i}\right]$ is the maximum of the exponential of the median PIDR across all *m* stories at site *i* as obtained from the simulated motions in the x direction (either fault normal or fault parallel), and $\max\left[\exp(\mu_{lnPIDR})_{R,Fx,i}\right]$ is the maximum of the exponential of the median PIDR across all *m* stories at site *i* as obtained from the real motions in the x direction. This process is iteratively repeated across all sites, providing the distribution of the demand ratio, ρ_{Fx}, across the computational domain.

In the following, two sites (C and D) will be utilized to showcase the application of the analysis method summarized in the flowchart of Figure **2.3**.

Site C is located about 9-km West of the Hayward Fault ($R_{rup,C}$ = 9-km, black square in Figure **2.2**) and is characterized by $V_{s30,C}$ = 515-m/sec, corresponding to very dense soil (class C); while site D is placed about 18-km West of the Hayward Fault ($R_{rup,D}$ = 18-km, black square in Figure **2.2**) with $V_{s30,D}$ = 195-m/sec, corresponding to stiff soil (class D).

Figure **2.4**-A shows the MCE_R design spectrum (red line) for site C, whose spectral acceleration parameters were obtained from the USGS maps for stiffer sites [30]. The seismic hazard deaggregation at site C indicated that a M7.21 Hayward Fault event at a distance of 10.91-km from the rupture is the controlling earthquake. The search criteria defined above to query the PEER NGA-W2 database [1] yielded 101 motions. After calculating the RotD100 from H1 and H2 and scaling the motions to approach the $MCE_{R,C}$ design spectrum in the bandwidth 0.2T1-2T1, with T1 = 2.93-sec for the 20-story building, the final set of 11 records was selected based on the criteria explained above (black lines). Finally, the RotD100 was calculated from the fault normal and parallel components of the simulated motions and scaled in the same 0.2T1-2T1 bandwidth (blue lines).

Figure **2.4**-B shows the results of the same type of analysis conducted on site D. The main difference between these two sites resides in the way the $MCE_{R,D}$ spectrum was derived. Since site D is characterized by Vs30 < 320-m/sec, the design spectrum was obtained as the lesser of the of the deterministic and probabilistic spectra, per ASCE/SEI 7 provisions [5-6], where the deterministic spectrum was calculated as the mean of the prediction of the spectral accelerations obtained from four NGA-W2 ground-motion models in the 0 to 10-sec bandwidth [23] [36-38]. Moreover, the empirical site-correction factors were applied to the simulated ground motions of site D since $V_{s30,D}$ < 500-/sec.

For both sites, the real records were rotated to obtain the fault normal and fault parallel components, and imported into OpenSees to perform fully nonlinear time-history analysis. Figure **2.5** shows the PIDR envelopes (single responses, median and standard deviation) obtained from real (black lines) and simulated (blue lines) motions at site C (Figure **2.5**-A) and D (Figure **2.5**-B) for the two separate components.

Once the building response data are available, ρ at site C is computed as $\rho_{FN,C} = \frac{\max[\exp(\mu_{lnPIDR})_{S,FN}]}{\max[\exp(\mu_{lnPIDR})_{R,FN}]} = \frac{1.06}{0.91} = 1.16$ and $\rho_{FP,C} = \frac{\max[\exp(\mu_{lnPIDR})_{S,FP}]}{\max[\exp(\mu_{lnPIDR})_{R,FP}]} = \frac{1.01}{0.78} = 1.29$; while at site D, $\rho_{FN,D} = 0.61$ and $\rho_{FP,D} = 1.107$. These values are stored and utilized to generate regional-scale maps of ρ_{Fx}, which will be presented and discussed in the next section of this paper. The data obtained from this analysis are also employed to assess the differences in the dispersion of the structural response obtained from the two sets of ground motions and the localization of the PIDR along the building height.

Results at site C indicate that the median demand posed by the simulated ground motions is larger than that posed by the real records for both components, with the maximum drift ratio localized at the upper stories of the building. Such distribution of the demand is attributed to the effect of the large simulated PSA amplitudes corresponding to higher vibrational modes of the structure, particularly in the fault parallel component, and the low simulated PSA amplitudes at the fundamental period of the structure, particularly for the fault normal component. See the spectra for the separate components represented in Figure **2.6**. Although drawing correlations between elastic spectra and the response of buildings subject to strong motions is challenged by the expected significant structure nonlinearities, this type of analysis can still provide insight into the expected different responses induced by sets of motions with remarkably different spectral shapes.

At site D, the peak median demand is localized along the first third of the building height for both sets of motions and components. The analysis of the velocity time-histories demonstrates that a number of motions have an impulsive character with amplitudes larger for the real records than for the simulated motions. **Error! Reference source not found.** l ists the ground motions utilized for the building analysis at site D, the pulse period (T_P) in the fault normal component calculated with the model proposed by [39], and the pulse amplitude of the scaled motions. The number of impulsive motions (three) in the list of real records matches the number predicted by the model proposed by [32] for the San Andreas Fault, while five (Hayward Fault) simulated records have a pulse-like component. The low variability of the demand (σ_{lnPIDR}) observed at site D, for the real records in the fault normal component and for the simulated motions in the fault parallel component, is the effect of the collapse criterion adopted in this study. The attainment of 4.5% PIDR with the same failure mode (i.e., PIDR along the first third of the building height) caused by multiple motions reflects into low values of the demand variability. Instead, the simulated motions still induce a localization of the PIDR towards the lower stories of the building in the fault normal component, yet without causing collapse. In such a case, the variability of the demand reflects the variability of the input motions.

The same type of analysis presented for the twenty-story building is repeated for the three-story building at the same sites, C and D. The MCE_R spectra obtained for the two sites and the sets of real and simulated ground motions remain the same. However, the motions are scaled in the spectral-period bandwidth 0.2T1 – 2T1, with T1 = 0.78-sec. The scale factors so obtained are applied to the two separate components of the real and simulated ground motions, and NLTH analyses are carried out in OpenSees [25].

At site C, $\rho_{FN,C} = \frac{0.97}{0.965} = 1.005$ and $\rho_{FP,C} = \frac{1.147}{1.139} = 1.007$; while at site D, $\rho_{FN,D} = 0.39$ and $\rho_{FP,D} = 0.84$.

Results show that the median demand posed by the real records is very similar to that posed by the simulated motions at site C and becomes higher at site D, particularly in the fault normal component. Recognizing that the response of stiffer structures is primarily controlled by the spectral acceleration at the first mode of vibration, $PSA(T_1)$, such results are consistent with the spectral acceleration amplitudes observed at T1 = 0.78-sec for both sites. The dispersion of the PIDR is higher for the real motions than for the simulated motions, except for the fault normal component at site C, reflecting the expected heterogeneity of records obtained from worldwide catalogs, and the correlation of site-specific ground motions obtained from realizations differing from each other for the properties of the rupture model only. A separate analysis conducted on the single components of the motions showed that the simulated ground motions at site C are not particularly polarized and that the spectral amplitudes of the fault normal component have a variability larger than in the fault parallel direction, which is aligned with the observed fault normal to fault parallel demand ratios and the higher variability of the PIDR seen in the fault normal component at site C.

2.5 Regional-Scale Maps

The analysis method described above for two sites is extended to all the stations of the computational domain, i.e. $i = 1, 2 \ldots 402$. The maximum of the median of the PIDR (hereafter simply referred to as PIDR) is calculated from the set of real and simulated ground motions and regional-scale maps of PIDR and ρ are generated.

Figure **2.7** and Figure **2.8** show the maps of the PIDR as obtained from the real records (A) and simulated ground motions (B) for the three-story building in the fault normal and fault parallel components, respectively. The PIDR varies from values of about 0.5%, corresponding to elastic response, to a maximum (cap) of 4.5%, corresponding to short of collapse, as demonstrated by a separate monotonic pushover analysis performed on the buildings. These values are also aligned with the PIDR associated with different limit states for RC moment-resisting frames in ASCE 43-19 [15].

The spatial distribution of the PIDR obtained from the fault normal component of the set of real records (Figure **2.7**-A) shows that the motions on the East of the Hayward Fault pose demands substantially lower than those obtained at sites on the West, with PIDRs that gradually decrease as the distance increases. The same evaluation performed with the simulated motions (Figure **2.7**-B) yields a substantially more pronounced site-to-site variability, with demands that attain a peak of ~4.5% on both sides of the Hayward Fault.

The majority of the sites East of the Hayward Fault, with few exceptions, are characterized by similar site conditions, with Vs30 ranging between 500-m/sec and 600-m/sec (see also Figure **2.2**). As a result, the site-specific MCE_R spectra at these sites differ from each other mainly by the distance from the causative fault, with spectral accelerations that decrease with the distance. Additionally, since the sets of real records are selected based on the magnitude governing the hazard at the site, site conditions, and source-to-site distance, they remain substantially the same (with differences in two or three records) and are simply scaled by factors that decrease as the distance from the fault increases. Overall, this results in a distance-dependent variation of the median demand. In contrast, the maps generated with the simulated records, although scaled to the same MCE_R spectra, reflect a high site-to-site variability deriving from path, fault geometry, and site-condition effects. Similar observations can be extended to the sites West of the Hayward Fault where, however, the heterogeneous distribution of Vs30 reflects in a slightly more complex distribution of the demand obtained from the real records. It is also worth noting that the simulated motions produce demands lower than those obtained from the real records for the majority of the sites residing South-West of the fault, where the seismic hazard is controlled by San Andreas Fault events. At these sites, the simulated motions are still obtained from Hayward Fault realizations and, as such, will lack features typical of near-field records, while the real records are selected based on the distance from the fault controlling the seismic hazard and, therefore, will possess the characteristics of near-field motions. Although it is a challenging task to identify the reasons for the observed differences for each site of the computational domain, it will be shown later that some of the differences observed at sites close to the Hayward Fault can be mainly attributed to the different polarization of the ground-motion components and to the amplitude of the fault normal pulses that are substantially higher for the real records than for the simulated motions.

Figure **2.8** shows the results of the same type of analysis carried out for the fault parallel component. In addition to what was observed for the fault normal component in terms of distance-dependent variation of the demand and site-to-site variability, in the fault parallel direction the higher demands West of the fault generated by the simulated records lead to median PIDR ~ 4.5% for a number of near-fault sites, while peaks of ~2.5% are observed in the median demands generated by the real records.

To better visualize and evaluate the differences in the demand obtained from the sets of real and site-specific simulated motions, Figure **2.9** shows the regional-scale maps of (A) $\rho_{FN,i}$ and (B) $\rho_{FP,i}$, see Eq. (1), for the three-story building.

Red shades indicate that the median demand calculated with the simulated motions is larger than that obtained from real records, while blue shades imply that the median demand computed with the simulated motions is smaller than that obtained from the real records. Shades close to white signify that the ratio of the median demand obtained from the two sets of ground motions is close to the unit. For the three-story building, a significant site-to-site variability of ρ is seen for both components, with a maximum ratio of 3.86 and a minimum ratio of 0.27 in the fault normal component.

A closer inspection of such cases demonstrates that the extreme values of ρ are the effect of the ground-motion scaling performed on the RotD100, rather than on the separate ground-motion components. For motions that are polarized in one direction, this translates into obtaining large spectra along the dominant direction of the motion and low spectra in the component orthogonal to it. If real and simulated ground motions do not have the same polarization, very high (or low) values of ρ should be expected. As an example, Figure **2.10** shows the spectra of the separate components scaled with the scale factor obtained from the scaling performed on the RotD100 for the station located on the Northern tip (East side) of the fault, for which $\rho_{FN} = 3.06$ and $\rho_{FP} = 0.85$.

It is seen that around the fundamental period of the three-story building (0.78-sec) in the fault normal component the median PSA of the simulated motions (blue thick line) is substantially higher than the $\mathrm{MCE_R}$ spectrum, while the median PSA of the real records (black thick line) lays below the design spectrum. As a result, the median building response obtained from the simulated motions is higher than that obtained from real records, yielding ρ_{FN} =3.06, see also Figure **2.9**-A (red color). In the fault parallel component, instead, the median PSA obtained from both sets of ground motions fall below the $\mathrm{MCE_R}$ spectrum, with the median simulated PSA slightly lower than the median PSA from real records, yielding $\rho_{FP} =$ 0.85. For the sake of conciseness, the case of minimum ρ is not described herein. However, the polarization of the motions has been identified as the main cause of very low values of ρ as well. Evidence from this analysis points to the importance of incorporating spectral compatibility criteria into the scaling of the separate ground-motion components in addition to the requirement that “the average of the maximum-direction spectra from all the ground motions shall not fall below 90% of the target response spectrum for any period” [6] in the spectral bandwidth of interest for the building.

Overall, the regional-scale map of Figure **2.9**-A shows that in the fault normal component the structural demands obtained from the simulated ground motions are substantially higher than those obtained from the real records East of the fault, remain comparable for a sparse number of stations West of the fault, and are lower in the San Jose area. On the contrary, the regional-scale map of Figure **2.9**-B demonstrates that there is a much more pronounced site-to-site variability of the demand ratios in the fault parallel component, with the simulated motions yielding higher demand throughout the computational domain (red shades), except for the Southern area of the region and the area surrounding the Northern tip of the fault.

The results obtained from the analysis of the twenty-story building are summarized in the regional-scale maps of Figure **2.11** and Figure **2.12**. Figure **2.11** shows the distribution of the building demand obtained for the fault normal component of the (A) real and (B) simulated ground motions. Similarly to what was observed for the three-story building, the median demand calculated from the real records is distance-dependent with peaks of median PIDR of ~2.0% East of the fault; while West of the fault the demand is rather uniform with median PIDR of ~4.5%, corresponding to severe damage and incipient collapse. A separate analysis of the scaled real records utilized at these sites demonstrated that the sets of motions were all characterized by large amplitude velocities, causing the collapse of the twenty-story building with the PIDR localized along the first third of the building height. The distribution of the demand obtained from the simulated ground motions, instead, exhibits higher variability with peaks of the PIDR between 3-3.5% East of the fault and ~4.5% West of the fault. Values of PIDR as low as 1.5% are seen near the Northern tip of the fault and in the San Jose area (South-West of the domain).

Figure **2.12** shows the results for the fault parallel component of the (A) real and (B) simulated motions. The distribution of median PIDR East of the fault has the same characteristics highlighted for the fault normal component. A more heterogeneous distribution of the median demand is observed for the set of simulated motions West of the fault, with peaks that attain 4.5% at far-field sites and values as low as ~2% at near-field sites. A separate analysis of the displacement and velocity time-histories demonstrated that this is caused by the complex displacement field generated by the simulated earthquakes. Two sites in the South-West area of the computational domain are selected to analyze such cases more closely; one ~2-km from the fault and the other ~8-km from the fault (black squares in Figure **2.12**). These locations are characterized by the same site class and by MCE_R spectra with similar shapes and acceleration amplitudes that decrease with distance. Figure **2.13** shows the displacement time-histories at the two sites as obtained from the simulated ground motions (A and B) and the real records (C and D), and attained peak ground displacement (PGD) with the applied scale factor. For the simulated motions, it is seen that the peak and residual ground displacements are larger at the site further from the fault than at the closer site, with peak values for the realizations having the hypocenter on the Southern side of the Hayward fault and thus closer to the selected sites (time histories fifth through eighth, see also R5 through R8 in Figure **2.1**). While partially influenced by the scale factors that are purely based on the spectral accelerations, this trend is seen in the unscaled and unprocessed motions as well pointing to a complex displacement field captured by the simulations. On the contrary, eight out of the eleven real records utilized at the selected sites are the same, leading to a simple scaling of such motions proportional to the spectral amplitudes and thus to peak ground displacements that decrease at increasing distance and, therefore, to median PID that are approximately distance-dependent. In such cases, there is a potential to underestimate the demand at sites further from the causative fault and, certainly, the issue of not accounting for the site specificity of the motions, deriving from the incorporation of path and site-condition effects.

Figure **2.14** shows the regional-scale maps of (A) $\rho_{FN,i}$ and (B) $\rho_{FP,i}$, see Eq. (1), for the twenty-story building. The color shades have the same meaning explained above for the three-story building. For the fault normal component, ρ is slightly below the unit for the majority of the near-fault sites West of the fault, with values ranging between 0.5-0.6 with a minimum of 0.29 South-West of the domain, and values above the unit for a few stations East of the fault, with a maximum of 1.92. For the fault parallel component, the distribution of ρ is likewise heterogeneous, with few values above the unit, and values of ρ below 0.5 for a number of sites near the fault (~2-km), which is the effect of the low demand obtained from the simulated motions at near-fault sites in the fault parallel component.

A site located 2-km West of the fault (see black square in Figure **2.14**) for which $\rho_{FN} = 1.05$ and $\rho_{FP} = 0.53$ and is selected to analyze potential reasons behind the difference in the ρ values for the two components. In the fault normal component, both sets of motions are seen to have peak ground velocities that attain values as high as ~3-m/sec (which represent the absolute peak values across the domain). While it is recognized that this is the effect of ground-motion scaling, exceptionally high peak ground velocities above 3-m/sec have been recorded on the hanging wall of the thrust fault during the 1999 Chi-Chi, Taiwan earthquake [40-41]. Moreover, the simulated motions have distinct two-sided large-amplitude pulses caused by forward-directivity effects. Such pulses can be clearly identified in the realizations with the hypocenter located on the Northern side of the fault (corresponding to realizations 1 through 4 in Figure **2.1**, in which a delayed wave arrival can be also seen) where the rupture propagates towards the considered site, inducing large demands in the twenty-story building (see also Figure **2.11**) and, overall, a median PIDR larger than that caused by the real records [32] [42-43]. In the fault parallel component, instead, the selected real records show large one-sided peak ground velocities with peaks above 2.5-m/sec that produce a median PIDR larger than the median demand obtained from the simulated motions.

2.6 Ground-Motion Scale Factors

This section summarizes some considerations on the scale factors applied to the real and simulated motions utilized in this study. Figure **2.15** shows the variation of the scale factors applied to the real records (black) and simulated motions (blue) as a function of the distance from the fault for the (A) three-story and (B) twenty-story building. The box plot displays the median, 25th and 75th percentile, maximum and minimum values.

For the three-story building, the scale factors applied to the simulated motions are lower than those applied to the real records for distances up to ~12 km from the fault, with the exception of sites at a distance of ~2-km, with median values around 1. A closer inspection of such cases showed that the largest scale factors are associated with sites East of the fault with Vs30>2000-m/sec, corresponding to the San Leandro gabbro rock block (see Figure **2.2**), for which the simulated ground motions predict very low-amplitude motions, particularly at short spectral periods. On the contrary, at sites further from the fault (>12-km) on the Western side of the Hayward Fault the scale factors applied to the simulated motions are systematically higher than those applied to the real records, with median values around 1.5. At these sites, where the seismic hazard is governed by San Andreas Fault earthquakes with M>>7, the real records are selected consistently with the established criteria, and therefore considering the magnitude and the distance from the fault controlling the hazard; whereas the simulated ground motions remain those generated by Hayward Fault M7 strike-slip events at distances that approach conditions typical of far-field sites. As a result, the scale factors applied to approach the MCE_R spectra are naturally larger than those needed to scale appropriately selected real records.

Similar considerations can be extended to the evaluation of the scale factors utilized for the twenty-story building analysis, for which the median scale factors applied to the simulated motions become larger than those applied to the real records for sites located at distances >10-km, with values that fluctuate around 2. It is also seen that the spread of the scale factors applied to the real records at near field sites is significantly larger than that observed in the simulated motions, analogously to what seen for the three-story building at distances between 4-km and 10-km.

Analyses of the type illustrated above demonstrate that the utilization of site-specific simulated motions from events consistent with the earthquake controlling the seismic hazard at the considered site leads to the use of scale factors lower than those applied to real records selected from worldwide catalogs. This has important implications in building NLTH analyses and performance evaluations, where the application of large factors has been largely demonstrated to introduce bias in the structural response [44-45] (to cite some).

However, it is envisioned that the availability of more earthquake scenarios and uncorrelated realizations will enable the possibility to perform pure site-specific analyses in which the sought set of ground motions will be selected from a large population of available records and ground-motion scaling will not be necessary or limited to low scale factors. Nevertheless, if more than 11 realizations become available and a variety of hypocenter locations are considered, the selection of the ground motions should be also driven by the appropriate incorporation of motions with forward-directivity effects and pulses and not by the minimization of the scale factors only.

2.7 Localization of Maximum Demand Along The Building Height

The previous sections of the paper discussed the response of the buildings as a function of the PIDR. In this section, the analysis of the structural response focuses on the localization of the maximum demand along the building height. Only the twenty-story building is considered.

Figure **2.16** and Figure **2.17** report the regional-scale maps showing the localization of the PIDR along the building height obtained from the (A) real and (B) simulated motions in the fault normal and fault parallel component, respectively. The twenty-story building is divided into three parts, the first one going from story 1 to story 7 indicated with “1” in the legend (white), the second one going from story 8 to story 14 indicated with “2” in the legend (gray), and the third one going from story 15 to story 20 indicated with “3” in the legend (black). Therefore, depending on where the PIDR is localized along the building height, the square representing each site is filled with a different color.

It is seen that in the fault normal component (Figure **2.16**) the real records pose a demand that is localized between story 1 and story 8 in the vast majority of the sites, with a few exceptions in the North-West region of the computational domain where the PIDR occurs between story 8 and story 15. On the contrary, a much more pronounced site-specificity is observed in the distribution of the maximum demand posed by the simulated motions, with the PIDR localized in the top stories of the building (between story 15 and 20) in a number of near-field and far-field sites.

Similar distributions of the localization of the PIDR are observed for the fault parallel component (Figure **2.17**), where in nearly all sites East of the fault the peak demand is localized along the first third of the building height, and in nearly all sites West of the fault the peak demand is localized along the second third of the building height. The simulated motions, instead, pose demands that are highly site-specific, with a number of sites exhibiting the maximum PIDR between story 15 and story 20.

Two main reasons behind these differences are identified. The first one resides in the nature of the population of real records. As highlighted earlier, for sites characterized by similar site conditions, the ground motions selected and utilized for the building analyses differ by two/three records, thus yielding median demands that are distance-dependent in terms of PIDR and very similar in terms of distribution along the building height. The second reason resides in the different spectral shape and polarization of real and simulated ground motions. The scaling in the 0.2T1-2T1 spectral bandwidth, in fact, tends to yield larger spectral amplitudes at shorter spectral periods for the simulated motions, which translates into higher spectral accelerations exciting the higher vibrational modes of the structure. In tall buildings, such condition manifests with a concentration of the demand toward the top stories of the structure. The plots in Figure **2.4** with the corresponding structural responses in Figure **2.5** provide one of such examples.

2.8 Concluding Remarks And Future Work

The study presented in this paper assesses the implications of utilizing site-specific simulated ground motions as opposed to historical records from worldwide catalogs in ASCE/SEI 7-compliant procedures [5-6] for seismic demand evaluations in RC buildings. The ground motions generated from eight (correlated) realizations of an M7 Hayward Fault strike-slip earthquake in the San Francisco Bay Area and real records selected from the PEER NGA-W2 database [1] are utilized to perform NLTH analyses. Two modern archetypal RC moment-resisting frame buildings are employed as a case study. One three-story building with fundamental period of vibration of 0.78-sec; and one twenty-story with fundamental period of vibration of 2.93-sec. An integrated computational framework is developed in Python and MATLAB [29] to query and link data from multiple sources, including the 2014 USGS [31] earthquake hazard and probability maps, the PEER NGA-

W2 [1] and EQSIM [14] databases, and the OpenSees software framework, perform a total of 30,552 NLTH analyses, and post-process results across the regional-scale computational domain. The structural demands obtained from the two sets of ground motions are compared in terms of median and dispersion (standard deviation) of PIDR and localization of the peak demand along the building height. The following considerations are derived.

Median demand. Results show differences in the structural demands as large as 50% (or above for selected sites), as either overestimate or underestimate of the (maximum) median values. Such differences are markedly site-specific both East and West of the fault and difficult to predict starting from the PIDR distributions obtained from historical records. At stations characterized by similar site conditions, a distance-dependent variation of the median demand calculated from the real motions is observed. This is an effect of the criteria utilized for selecting the records, conventionally based on magnitude, rupture distance and site conditions, which lead to the utilization of similar sets of records that are scaled by factors that decrease at longer distances. On the contrary, the demand distributions obtained from the simulated ground motions, although scaled to match the same MCE_R design spectra, are highly site-specific with demands that are not strictly distance-dependent. A closer inspection of such cases demonstrated that 3D physics-based simulations that incorporate path, fault geometry, and site-condition effects can capture complex displacement fields and forward-directivity effects that largely influence the structural response, particularly of the twenty-story building in both fault normal and fault parallel components. While forward-directivity effects can potentially be accounted for upon appropriate selection of the historical records, the incorporation of path and site-condition effects remains critical, particularly for the analysis of sites and earthquake scenarios for which records from consistent events are not available. In addition, the analysis of the demand posed in the two separate components (fault normal and fault parallel) of the sets of scaled ground motions highlighted significant differences in the polarization and spectral shape between real and simulated motions. According to the ASCE/SEI 7 [5-6], in fact, the scaling is performed on the maximum rotated component of the ground motion (i.e., RotD100) in the 0.2T1-2T1 bandwidth, and the factors so obtained are applied to the two separate components. In highly polarized ground motions, this translates into spectral amplitudes that can be well below the target (or design) spectrum in one component and well above the design spectrum in the other. In the study presented in this paper, the simulated motions show a significant polarization in either component at several stations across the domain, with the effect of yielding values of the demand ratio (ρ) well below the unit in one component and well above the unit in the other.

Demand variability. The observed variability of the PIDR across the building height is generally lower for the simulated motions than for the real records. This is the expected effect of the nature of the two sets of motions, where the historical records are selected from worldwide catalogs and the simulated ground motions are generated from realizations differing from each other in terms of rupture model and rupture initiation only. A significant decrease of the variability of the demand is seen at sites where multiple ground motions induce a demand close or equal to the predefined failure criterion (IDR = 4.5% in this study) at approximately the same location along the building height. This is observed in several stations for the twenty-story building where the impulsive motions have large amplitudes.

Scale factors. A comparison of the scale factors applied to the ground motions (real and simulated) utilized to analyze the three and twenty-story buildings demonstrates that, with few exceptions at very stiff rock sites, the simulated records utilize scale factors that are lower than those utilized with the real records at near-field sites. An inversion of this trend is observed at sites further from the Hayward Fault where the seismic hazard is controlled by San Andreas Fault events with M>>7. This is the effect of the selection of the real records consistent with the event controlling the seismic hazard at the sites and, yet, the utilization of simulated records that model an event different from that dominating the hazard at approximately far-field sites

Demand localization along the building height. Finally, the analysis of the localization of the maximum demand along the building height reveals significant differences between real and simulated motions. While the real records tend to pose maximum demands localized between story 1 and 7 in both components and between story 8 and 14 in the fault parallel component West of the fault, the simulate motions induce maximum demands that are distributed at different locations along the building height. The first reason behind this difference resides in the nature of the population of real records. The ground motions selected and utilized for the building analyses, in fact, differ by two/three motions, thus yielding median demands that are distance-dependent in terms of PID and very similar in terms of distribution along the building height. The second reason is in the different spectral shape and polarization of real and simulated motions that yield larger spectral amplitudes at shorter spectral periods for the simulated motions. This translates into higher spectral accelerations exciting the higher vibrational modes of the structure and therefore into a concentration of the demand toward the top stories of the structure.

Overall, evidence from this study demonstrates that simulated motions generated from 3-D physics-based wave propagation models have a potential to inform current code-compliant design and assessment procedures. Simulated motions can, in fact, provide insight into the expected site and event-specific characteristics of the motions as opposed to the selection of historical records from worldwide catalogs that should possess, in the average, a set of sought characteristics. This is particularly relevant to the design or assessment of structures subject to ground motions generated by not-historical events (e.g., large magnitude Hayward Fault earthquakes). Results also show that the differences in the structural demands obtained from the sets of real and simulated ground motions cannot be easily inferred from ASCE/SEI-compliant procedures that adopt historical records. The results discussed in this paper can be affected by the adopted selection and scaling methods. However, the objective is to provide a methodology for conducting a systematic and rigorous type of comparisons between structural demands obtained from real and simulated motions and offering insight into the differences and biases that real records can introduce in structural demand assessments.

Moving forward, studies of this type should be extended to uncorrelated realizations of earthquake events of different magnitude, adopting different rupture models to better represent the expected aleatory variability of the ground motions and the variability of the corresponding structural response. Moreover, including earthquake scenarios and realizations with magnitudes closer to those controlling the seismic hazard will contribute to further decrease the applied scale factors and obtain unbiased site-specific simulation-based structural designs and assessments. Based on the results shown in this paper, it is advisable to employ a combination real and fully validated simulated ground motions to ensure the sought structural response variability and concurrently incorporate the necessary site-specificity in performance evaluation and fragility analyses.

Acknowledgements

The authors wish to thank the anonymous reviewer for their thorough and insightful comments that helped improve the quality of the paper. The simulated ground motions utilized in this study were provided by the EQSIM Exascale Application Development Project at Lawrence Berkeley National Laboratory by Dr. Arben Pitarka and Dr. Arthur Rodgers of Lawrence Livermore National Laboratory. The help of Dr. Pitarka in processing the ground motions for the application of the empirical site-correction factors is greatly appreciated.

References

[1] Pacific Earthquake Engineering Research (PEER) Center. "NGA-West2 Grond Motion Database." https://ngawest2.berkeley.edu/spectras/new?sourceDb_flag=1.

[2] Strong-motion Seismograph Networks. https://www.kyoshin.bosai.go.jp/

[3] Sgobba, S.A., Felicetta, C., Lanzano, G., Ramadan, F., D'Amico, M.C., Pacor, F., 2021, "NESS2.0: An Updated Version of the Worldwide Dataset for Calibrating and Adjusting Ground-Motion Models in Near Source." *Bull. Seismol. Soc. Am,* 111 (5): 2358–2378.

[3] Sørensen, Mathilde B., and Dominik H. Lang. 2015. "Incorporating Simulated Ground Motion in Seismic Risk Assessment: Application to the Lower Indian Himalayas." *Earthquake Spectra* 31 (1): 71–95. https://doi.org/10.1193/010412EQS001M.

[4] Burks, Lynne S., Reid B. Zimmerman, and Jack W. Baker. 2015. "Evaluation of Hybrid Broadband Ground Motion Simulations for Response History Analysis and Design." *Earthquake Spectra* 31 (3): 1691–1710. https://doi.org/10.1193/091113EQS248M.

[5] ASCE/SEI 7-16, "Minimum Design Loads and Associated Criteria for Buildings and Other Structures," 2016.

[6] ASCE/SEI 7-22, "Minimum Design Loads and Associated Criteria for Buildings and Other Structures," 2022.

[7] Smerzini, Chiara, and Kyriazis Pitilakis. 2018. "Seismic Risk Assessment at Urban Scale from 3D Physics-Based Numerical Modeling: The Case of Thessaloniki." *Bulletin of Earthquake Engineering* 16 (7): 2609–31. https://doi.org/10.1007/s10518-017-0287-3.

[8] Bijelić, Nenad, Ting Lin, and Gregory G. Deierlein. 2019a. "Quantification of the Influence of Deep Basin Effects on Structural Collapse Using SCEC Cybershake Earthquake Ground Motion Simulations." *Earthquake Spectra* 35 (4): 1845–64. https://doi.org/10.1193/080418EQS197M

[9] Bijelić, Nenad, Ting Lin, and Gregory G. Deierlein. 2019a. "Evaluation of Building Collapse Risk and Drift Demands by Nonlinear Structural Analyses Using Conventional Hazard Analysis versus Direct Simulation with Cybershake Seismograms." *Bulletin of the Seismological Society of America* 109 (5): 1812–28. https://doi.org/10.1785/0120180324.

[10] McCallen, D., F. Petrone, M. Miah, A. Pitarka, A. Rodgers, and N. Abrahamson. 2020. "EQSIM – A Computational Framework for Fault-to-Structure Earthquake Simulations on Exascale Computers Part II : Regional Simulations of Building Risk." *Earthquake Spectra*. Volume 37, Issue 2

[11] Zhong, Kuanshi, Ting Lin, Gregory G. Deierlein, Robert W. Graves, Fabio Silva, and Nicolas Luco. 2021. "Tall Building Performance-Based Seismic Design Using SCEC Broadband Platform Site-Specific Ground Motion Simulations." *Earthquake Engineering and Structural Dynamics* 50 (1): 81–98. https://doi.org/10.1002/eqe.3364.

[12] Antonietti, Paola F., Ilario Mazzieri, Laura Melas, Roberto Paolucci, Alfio Quarteroni, Chiara Smerzini, and Marco Stupazzini. 2021. "Three-Dimensional Physics-Based Earthquake Ground Motion Simulations for Seismic Risk Assessment in Densely Populated Urban Areas." *Mathematics In Engineering* 3 (2): 1–31. https://doi.org/10.3934/mine.2021012.

[13] Haselton, C.B. (Editor), Evaluation of Ground Motion Selection and Modification Methods: Predicting Median Interstory Drift Response of Buildings, PEER report 2009/01

[14] McCallen, D, Petersson, A, Rodgers, A, Pitarka, A, Miah, M, Petrone, F, Sjogreen, B, Abrahamson, N, Tang, H. 2020. "EQSIM—A multidisciplinary framework for fault-to-

structure earthquake simulations on exascale computers part I: Computational models and workflow." *Earthquake Spectra*. Volume 37, Issue 2

[15] ASCE 43-19. 2019. "Seismic Design Criteria for Structures, Systems, and Components in Nuclear Facilities."

[16] Graves, R., and A. Pitarka. 2016. "Kinematic Ground Motion Simulations on Rough Faults Including Effects of 3D Stochastic Velocity Perturbations." *Bulletin of the Seismological Society of America* 106 (5): 2136–53.

[17] Pitarka, A., R. Graves, K. Irikura, K. Miyakoshi, and A. Rodgers. 2019. "Kinematic Rupture Modeling of Ground Motion from the M7 Kumamoto, Japan Earthquake." *Pure and Applied Geophysics*. https://doi.org/10.1007/s00024-019-02220-5.

[18] Petrone, Floriana, Norman Abrahamson, David McCallen, Arben Pitarka, and Arthur Rodgers. 2021. "Engineering Evaluation of the EQSIM Simulated Ground-Motion Database: The San Francisco Bay Area Region." *Earthquake Engineering and Structural Dynamics*, 50(15), pp. 3939-3961. https://doi.org/10.1002/eqe.3540.

[19] Petrone F, Abrahamson N, McCallen D, Miah M. 2021. "Validation of (not-historical) large-event near-fault ground-motion simulations for use in civil engineering applications." Earthquake Eng Struct Dyn. 50:116-134. https://onlinelibrary.wiley.com/doi/epdf/10.1002/eqe.3366

[20] Sjögreen, Björn, and N. Anders Petersson. 2012. “A Fourth Order Accurate Finite Difference Scheme for the Elastic Wave Equation in Second Order Formulation.” *Journal of Scientific Computing* 52 (1): 17–48. https://doi.org/10.1007/s10915-011-9531-1.

[21] https://www.usgs.gov/natural-hazards/earthquake-hazards/science/3-d-geologic-and-seismic-velocity-models-san-francisco?qt-science_center_objects=0#qt-science_center_objects (last accessed in 2020)

[22] Boore, D.M., Stewart, J.P., Seyhan E., Atkinson, G.M. 2014. “NGA-West2 Equations for Predicting PGA, PGV, and 5% Damped PSA for Shallow Crustal Earthquakes.” *Earthquake Spectra* 30 (3): 1057–1085. https://doi.org/10.1193/070113EQS184M.

[24] ACI (American Concrete Institute), *318-19 Building Code Requirements for Structural Concrete and Commentary*. 2019.

[25] McKenna, F., Fenves, G. L, and Scott, M. H. (2000) Open System for Earthquake Engineering Simulation. University of California, Berkeley, http://opensees.berkeley.edu.

[26] Ibarra, Luis F., Ricardo A. Medina, and Helmut Krawinkler. 2005. “Hysteretic Models That Incorporate Strength and Stiffness Deterioration.” *Earthquake Engineering and Structural Dynamics* 34 (12): 1489–1511. https://doi.org/10.1002/eqe.495.

[27] Haselton, Curt B, Abbie B Liel, Sarah C Taylor-Lange, and Gregory G Deierlein. 2016. “Calibration of Model to Simulate Response of Reinforced Concrete Beam-Columns to Collapse.” *ACI Structural Journal* 113.

[28] Python v.3.11.1 software. https://www.python.org/

[29] Matworks, MATLAB v R_2022 software. https://www.mathworks.com/products/matlab.html

[30] USGS. “Unified Hazard Tool.” https://earthquake.usgs.gov/hazards/interactive/.

[31] https://www.usgs.gov/programs/national-geospatial-program/national-map

[32] Hayden, Connor P., Jonathan D. Bray, and Norman A. Abrahamson. 2014. “Selection of Near-Fault Pulse Motions.” *Journal of Geotechnical and Geoenvironmental Engineering* 140 (7). https://doi.org/10.1061/(asce)gt.1943-5606.0001129.

[33] Seifried, A.E., Baker, J.W., 2016. “Spectral Variability and Its Relationship to Structural Response Estimated from Scaled and Spectrum-Matched Ground Motions”, Earthquake Spectra, 32(4)

[34] Teng G, Baker J. Evaluation of SCEC Cyber Shake ground motions for engineering practice. Earthquake Spectra. 2019;35(3):1311-1328.

[35] Reyes, J.C., E. Kalkan. 2012. “Relevance of Fault-Normal/Parallel and Maximum Long-Period (3 to 16 s) Ground Automated Damage Detection, Early-Warning Ed Hospital Buildings in the United States Direction Rotated Ground Motions on Nonlinear Behavior of Multi-Story Buildings.” 15th World Conference on Earthquake Engineering. Lisbon, Portugal

[36] Abrahamson, N. A., W. J. Silva, and R. Kamai. 2014. “Summary of the ASK14 Ground Motion Relation for Active Crustal Regions.” *Earthquake Spectra,* 30 (3): 1025–1055. https://doi.org/10.1193/070913EQS198M.

[37] Boore, D. M., J. P. Stewart, E. Seyhan, and G. M. Atkinson. 2014. “NGA-West2 Equations for Predicting PGA, PGV, and 5% Damped PSA for Shallow Crustal Earthquakes.” *Earthquake Spectra,* 30 (3): 1057–1085. https://doi.org/10.1193/070113EQS184M.

[38] Chiou, B. S.-J., and R. R. Youngs. 2014. “Update of the Chiou and Youngs NGA Model for the Average Horizontal Component of Peak Ground Motion and Response Spectra.” *Earthquake Spectra*, 30 (3): 1117–1153. https://doi.org/10.1193/072813EQS219M.

[39] Kardoutsou, V., I. Taflampas, and I. N. Psycharis. 2017. “A new pulse indicator for the classification of ground motions.” *Bulletin of the Seismological Society of America*, 107 (3): 1356–1364. Seismological Society of America.

[40] Anderson, J.G., 2008, “Exceptional Ground Accelerations and Velocities Caused by Earthquakes”, Final Technical Report, Part B, TR-NQ-022-2, Nevada System of Higher Education.

[41] Shin, T.C., Teng, T., 2001, “An Overview of the 1999Chi-Chi, Taiwan, Earthquake”, Bulletin of the Seismological Society of America, 91(5), pp.895–913

[42] Gazetas, G., E. Garini, and T. Georgarakos. 2008. “Effects of near-fault ground shaking on sliding systems.” *Geotechnical Earthquake Engineering and Soil Dynamics IV*, 1–23.

[43] Somerville, P. 2000. “Seismic hazard evaluation.” *Bulletin of the New Zealand Society for Earthquake Engineering*, 33 (3): 371–386. https://doi.org/10.5459/bnzsee.33.3.371-386.

[44] Baker, J. W. 2007. “Measuring bias in structural response caused by ground motion scaling.” *8th Pacific Conference on Earthquake Engineering, Singapore*.

[45] Huang, Y.-N., A. S. Whittaker, N. Luco, and R. O. Hamburger. 2011. “Scaling earthquake ground motions for performance-based assessment of buildings.” *Journal of Structural Engineering*, 137 (3): 311–321. American Society of Civil Engineers.

Table 2.1. Fundamental vibrational periods of the RC buildings.

	Direction	Mode 1 [sec (%)]	Mode 2 [sec (%)]	Mode 3 [sec (%)]
Three-story building	X	0.78 (0.86)	0.21 (0.98)	0.10 (1.00)
	Y	0.64 (0.88)	0.18 (0.98)	0.09 (1.00)
Twenty-story building	X	2.93 (0.74)	1.09 (0.89)	0.65 (0.92)
	Y	2.40 (0.73)	0.90 (0.87)	0.53 (0.92)

Table 2.2. List of the records utilized for the building analyses at site D and pulse period (T_P) of the fault normal component.

Historical	**T_P [sec] (A_P [cm/sec])**	**Simulated**	**T_P [sec] (A_P [cm/sec])**
Imperial Valley-06 (1979) - El Centro Array #10, 50	-	R1	-
Chi-Chi Taiwan (1999) - TCU123, E	-	R2	
Darfield New Zealand (2010) - Riccarton High School, N86W	-	R3	2.38 (148)
Iwate (2008) - IWT011, NS	2.86 (85)	R4	-
El Mayor-Cucapah (2010) - Cerro Prieto Geothermal, 0	-	R5	2.90 (83)
Chi-Chi Taiwan (1999) - TCU110, E	2.42 (143)	R6	2.90 (83)
Darfield New Zealand (2010) - ROLC, S29E	-	R7	2.92 (84)
Denali Alaska (2002) - TAPS Pump Station #10, 47	2.66 (125)	R8	2.98 (79)
Kocaeli Turkey (1999) - Duzce, 180	-	-	
Kocaeli Turkey (1999) - Yarimca, 60	-	-	
El Mayor-Cucapah (2010) - Ejido Saltillo, 0	-	-	

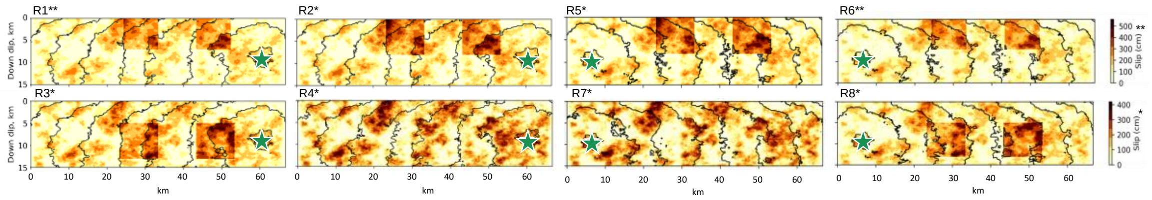

Figure 2.1. Slip distribution of the rupture models utilized to simulate eight M7 earthquake realizations (R1 through R8). The green star represents the location of the hypocenter (Adapted from Petrone et al., 2021 [18]).

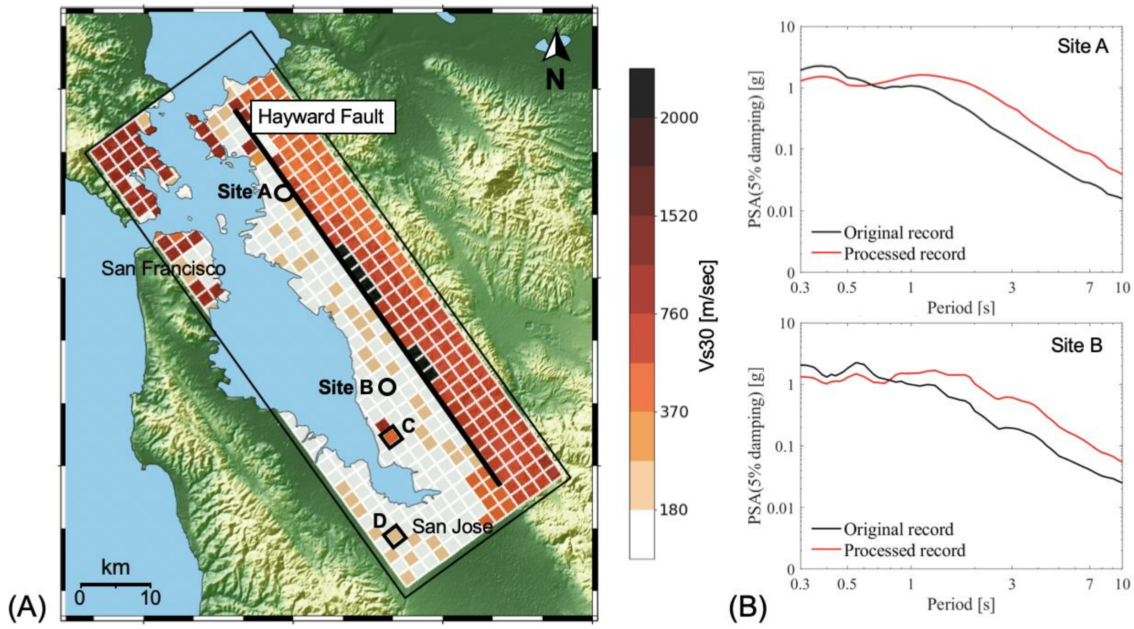

Figure 2.2. (A) Distribution of the shallow shear-wave velocity (Vs30) in the San Francisco Bay Area computational domain across the stations considered in this study. This distribution follows the USGS 3D velocity model [21]. The black line represents the projection of the Hayward Fault. (B) Pseudo-acceleration spectra of the original (black) and processed (red) ground-motion record at two sample sites where Vs30 < 500-m/sec.

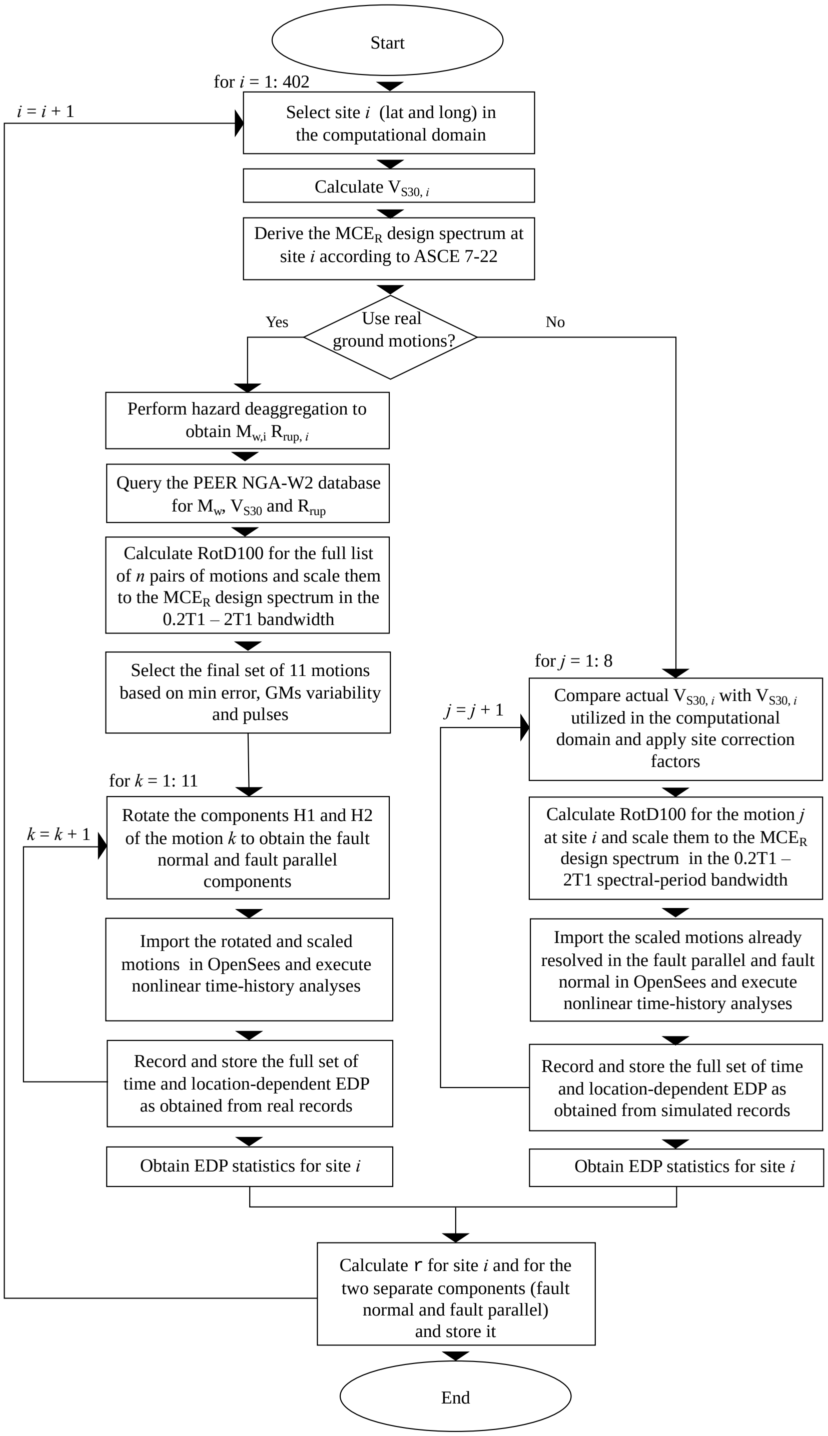

Figure 2.3. Workflow established to conduct the regional-scale analyses and compare structural demands as obtained from populations of real and simulated ground motions.

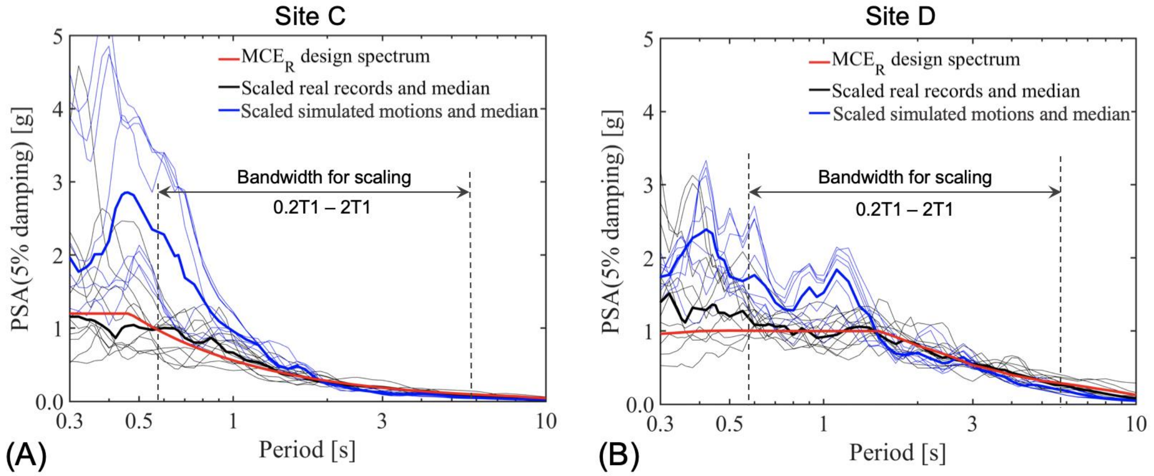

Figure 2.4. MCE$_R$ design spectrum, real records and simulated motions scaled in the bandwidth 0.2T1 – 2T1 with T1 = 2.93-sec for two sites (A) Site C with $V_{s30,C}$ = 515-m/sec and (B) Site D with $V_{s30,D}$ = 195-m/sec.

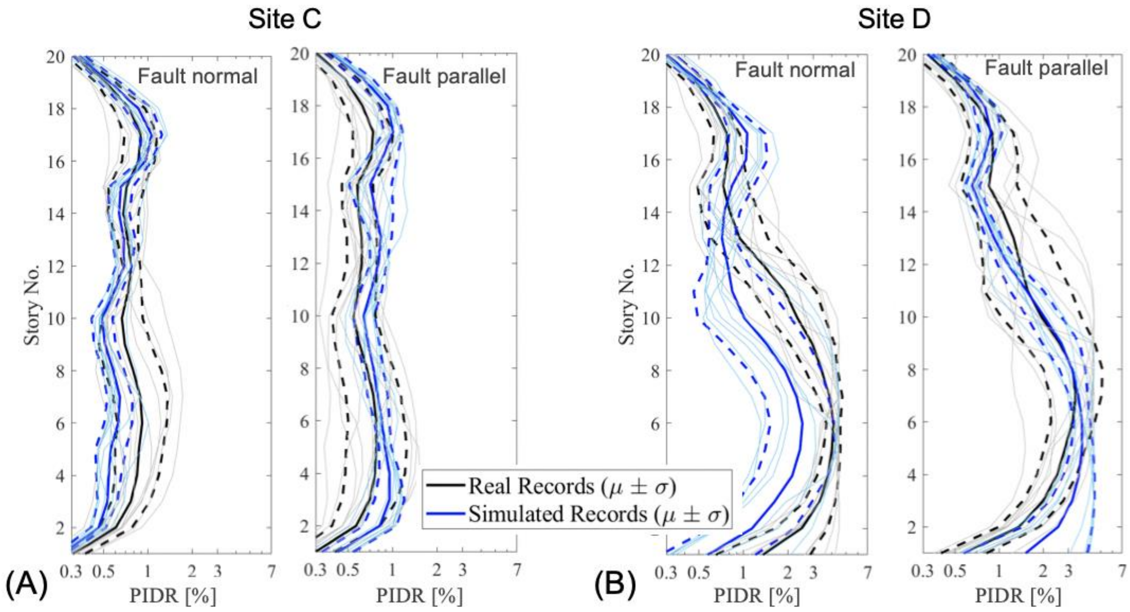

Figure 2.5. Twenty-story building response statistics obtained from the two separate components of real and simulated motions at (A) site C and (B) site D.

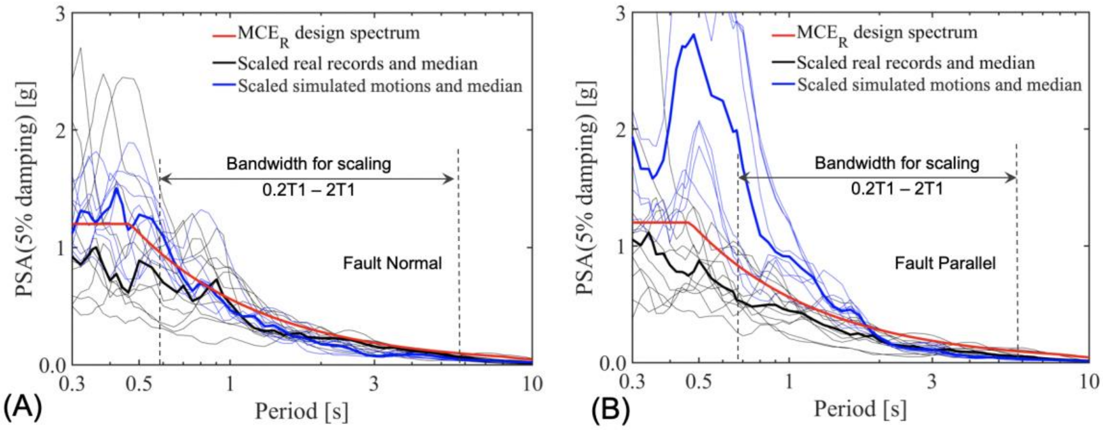

Figure 2.6. Site C: MCE$_R$ design spectrum with scaled real and simulated ground motions for the two separate components (A) fault normal and (B) fault parallel.

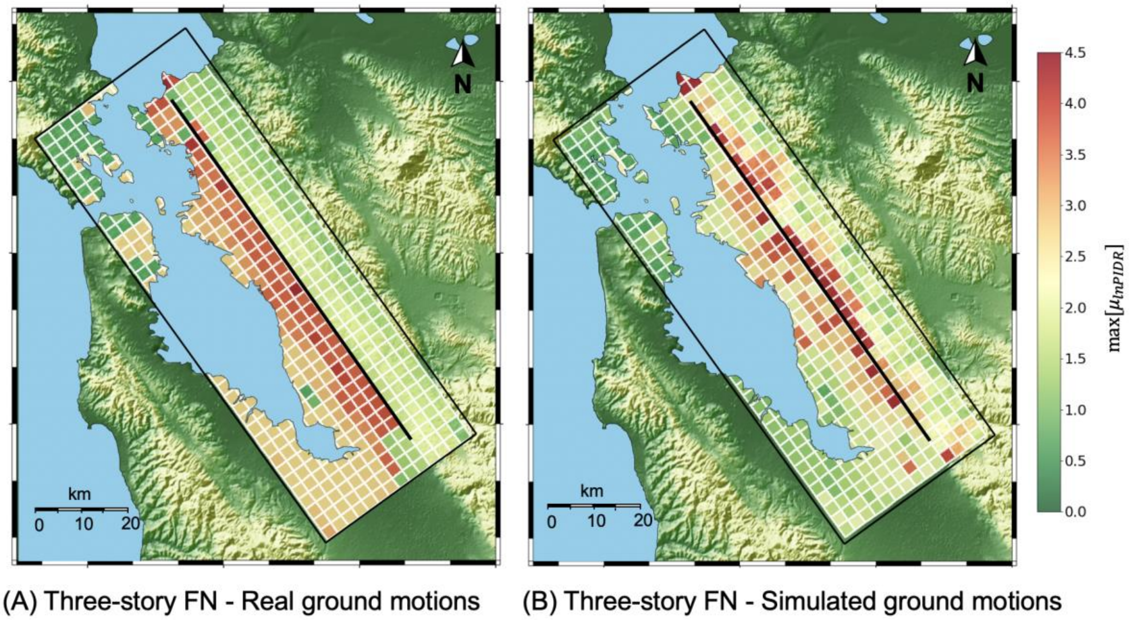

(A) Three-story FN - Real ground motions (B) Three-story FN - Simulated ground motions

Figure 2.7. Regional-scale map of the median PIDR for the three-story building in the fault normal component as obtained from the (A) real and (B) simulated ground motions.

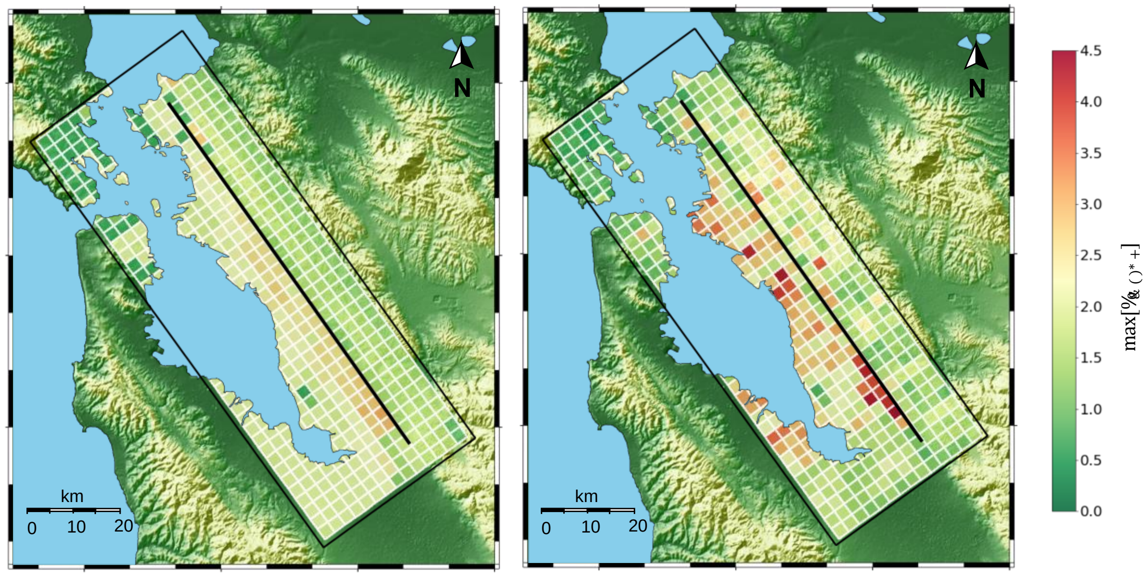

(A) Three-story FP - Real ground motions (B) Three-story FP - Simulated ground motions

Figure 2.8. Regional-scale map of the median PIDR for the three-story building in the fault parallel component as obtained from the (A) real and (B) simulated ground motions.

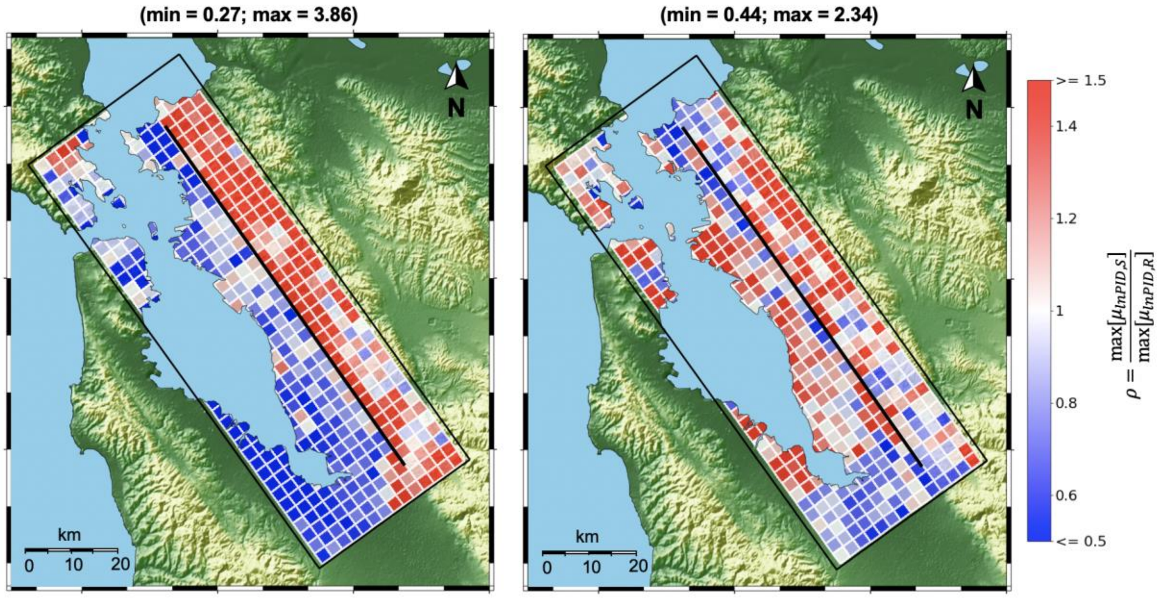

(A) Three-story FN

(B) Three-story FP

Figure 2.9. Regional-scale maps of ρ (ratio of the structural demand obtained from the simulated motions to the structural demand obtained from the real record) for the three-story building in the (A) fault normal and (B) fault parallel component.

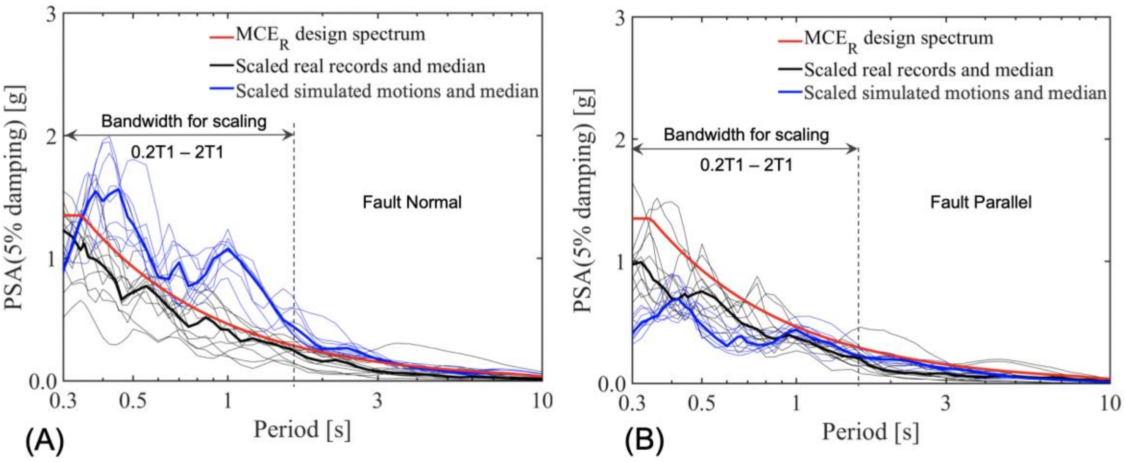

Figure 2.10. PSA of the two separate components of the real and simulated ground motions scaled with the scale factors obtained from the scaling performed on the RotD100 for the station right on the North tip of the fault: (A) fault normal and (B) fault parallel.

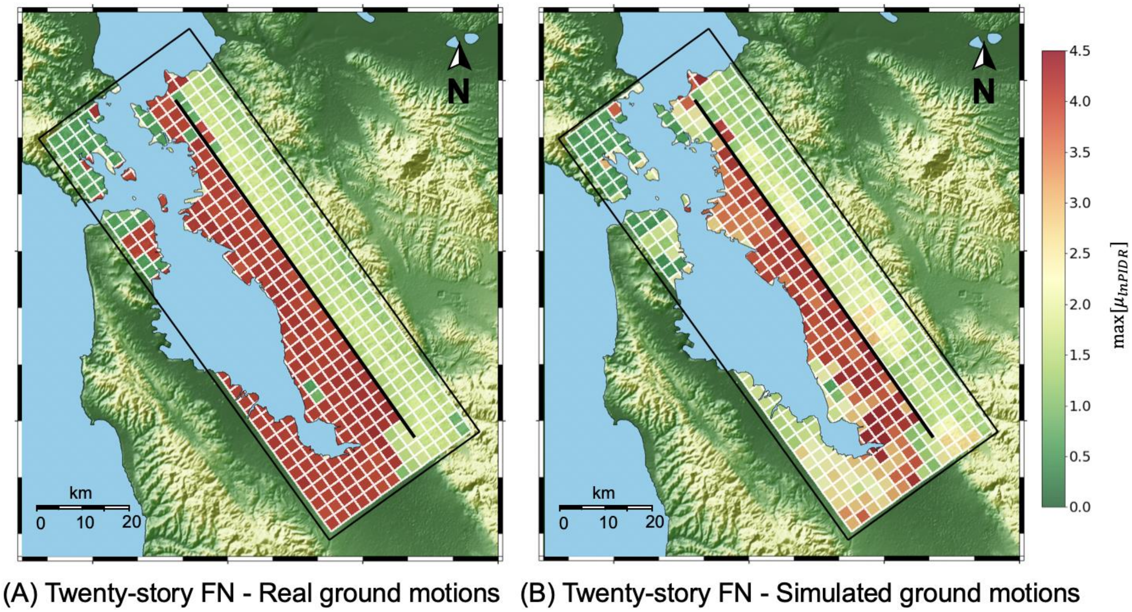

Figure 2.11. Regional-scale map of the median PIDR for the twenty-story building in the fault normal component as obtained from the (A) real and (B) simulated ground motions.

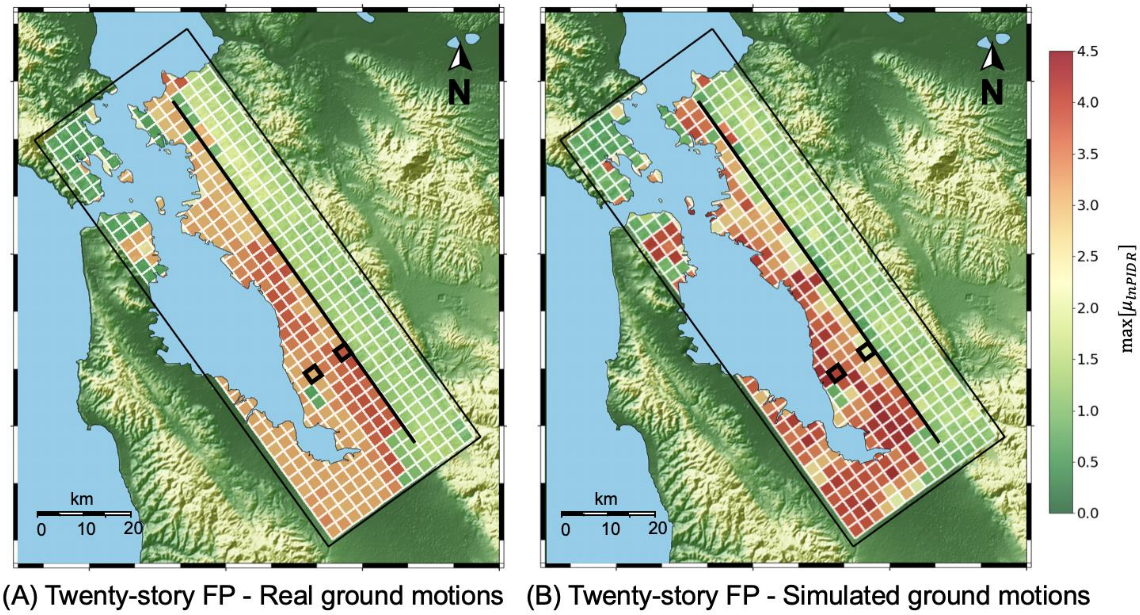

(A) Twenty-story FP - Real ground motions (B) Twenty-story FP - Simulated ground motions

Figure 2.12. Regional-scale map of the median PIDR for the twenty-story building in the fault parallel component as obtained from the (A) real and (B) simulated ground motions.

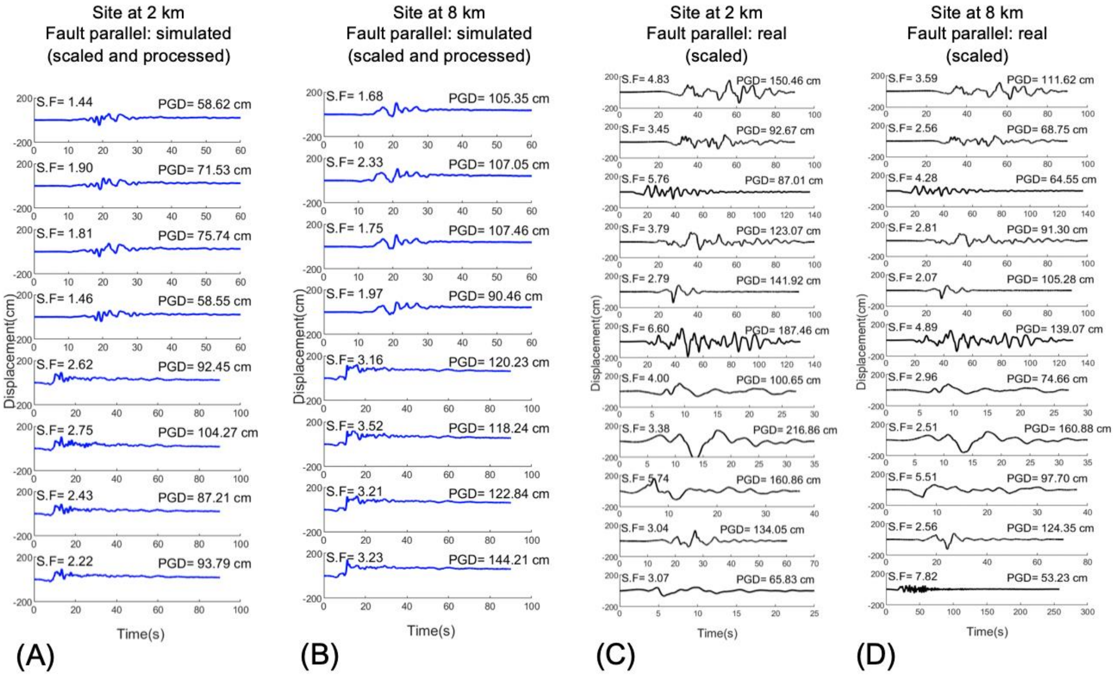

Figure 2.13. Displacement time-history of the fault parallel component of simulated motions at a site (A) ~2-km away from the fault and (B) 8-km away from the fault and real records at (C) ~2-km away from the fault and (B) 8-km away from the fault.

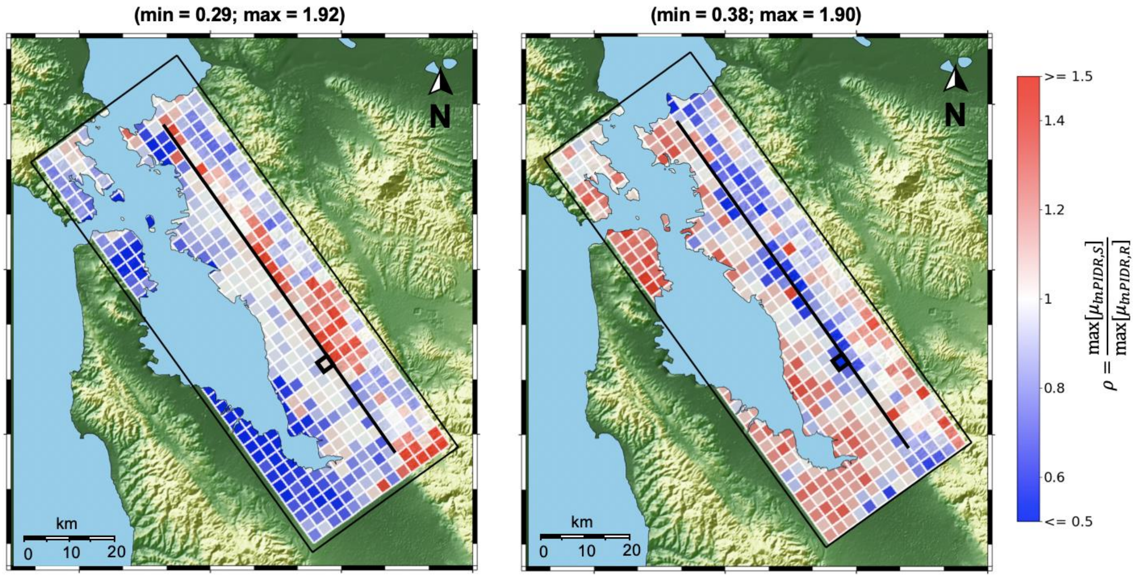

(A) Twenty-story FN

(B) Twenty-story FP

Figure 2.14. Regional-scale maps of ρ (ratio of the structural demand obtained from the simulated motions to the structural demand obtained from the real records) for the twenty-story building in the (A) fault normal and (B) fault parallel component.

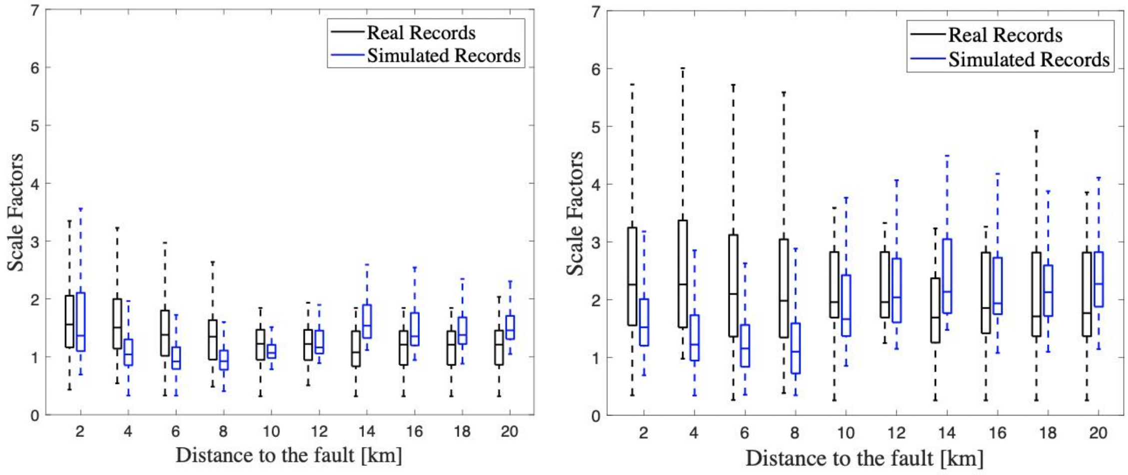

(A) Three-story building

(B) Twenty-story building

Figure 2.15. Variation of mean scale factors applied to the real and simulated motions at each station as a function of distance for the (A) three-story and (B) twenty-story building.

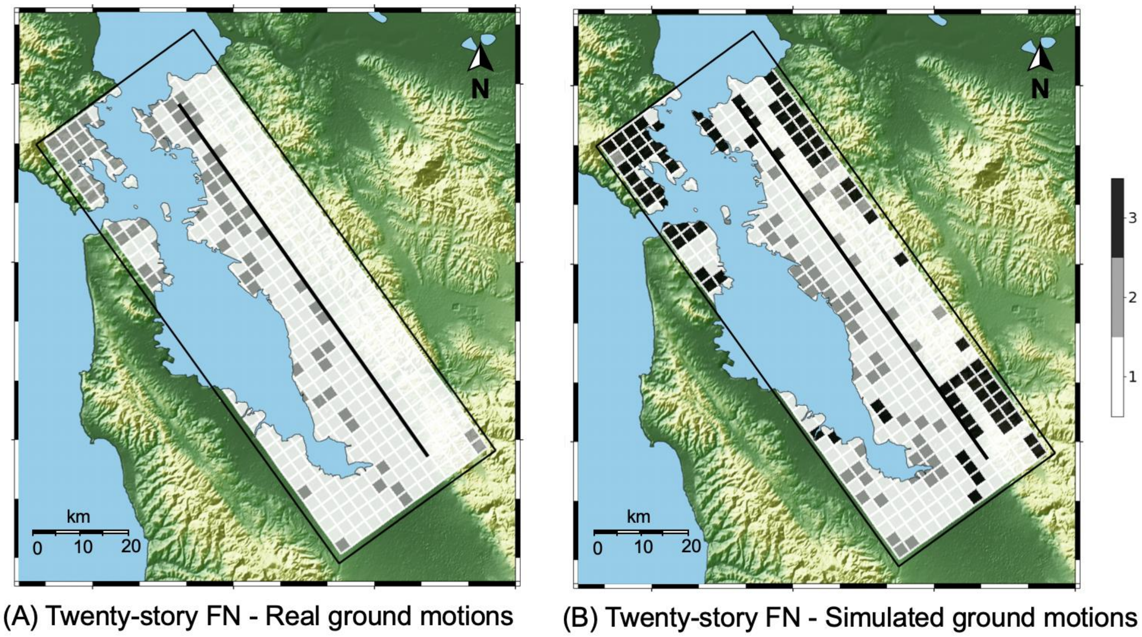

(A) Twenty-story FN - Real ground motions (B) Twenty-story FN - Simulated ground motions

Figure 2.16. Regional-scale maps showing the localization of the PIDR along the building height obtained from the fault normal component of the (A) real motions and (B) simulated motions.

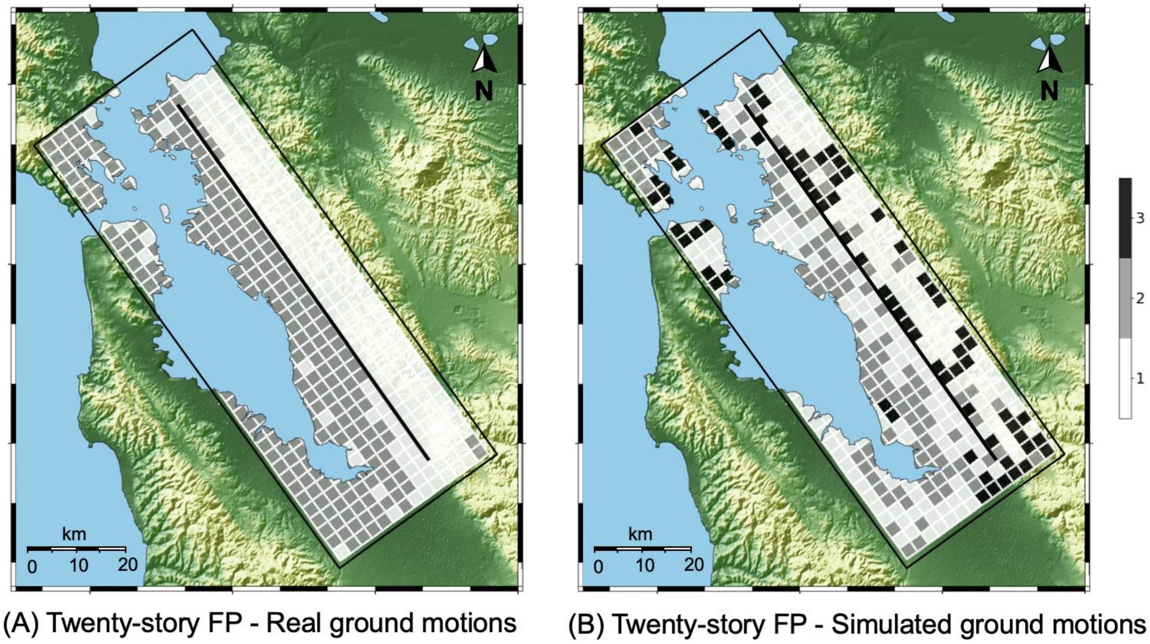

(A) Twenty-story FP - Real ground motions (B) Twenty-story FP - Simulated ground motions

Figure 2.17. Regional-scale maps showing the localization of the PIDR along the building height obtained from the fault parallel component of the (A) real motions and (B) simulated motions.

3 ASSESSING THE IMPACT OF REGION SPECIFICITY ON RC BUILDINGS FRAGILITY WITH GROUND-MOTION SIMULATIONS

This chapter of the dissertation is accepted to be published in the 18th World Conference on Earthquake Engineering 2024 (WCEE 2024)

Abstract

Probabilistic seismic risk assessments rely on the knowledge of the annual frequency of exceedance of a load level and the appropriate estimate of the conditional probability of exceeding predefined limit states in a structure at a given seismic load level, generally referred to as fragility. The selection of ground motions to perform nonlinear dynamic analyses is a crucial step in deriving fragility functions, known to potentially introduce significant biases in risk assessments. This study utilizes validated simulated ground motions generated from multiple realizations of large magnitude Hayward Fault strike-slip earthquakes in the San Francisco Bay Area region and scaled to site-specific ASCE 7-compliant design spectra to estimate the demand statistics posed to two structures: a low-rise and a mid-rise reinforced concrete (RC) building. Results are compared with those obtained from state-of-the-art approaches based on the use of records selected from worldwide catalogues and scaled to the same design spectra. The ground motions are simulated in SW4 on the EQSIM platform, the PEER-NGA W2 database is employed to select records consistent with the hazard at the considered 546 sites, and the OpenSees software is used to develop fully nonlinear models of the building archetypes. 30,522 nonlinear dynamic analyses are utilized to generate fragility functions with a cloud-based approach for different limit states. The maximum inter-story drift ratio is utilized as the key engineering demand parameter to assess and compare structural performance. Evidence from this study highlights the significance of utilizing region-specific simulated ground motions as opposed to historical records, with substantial differences seen in the structural demand median and distribution across the computational domain.

Keywords: Simulated ground motions, fragility curves, regional-scale analysis, site-specific seismic evaluation

3.1 Introduction

Site-specific ASCE/SEI 7-compliant (ASCE/SEI 7-22, 2021) approaches to seismically evaluate and design structures require the use of a suite of ground motions that are selected and scaled to a target spectrum to eventually perform nonlinear time-history analyses (NLTH). The suitable set of ground motion records shall be selected making appropriate considerations on the earthquake parameters controlling the hazard at the site such as magnitude, fault distance, tectonic regime etc. When tasked with the design at sites residing in the vicinity of a major active fault with site conditions not well represented in the existing datasets of records, engineers face the challenge of not having enough earthquake motions to perform an adequate number of NLTH analyses. As a result, ASCE/SEI 7 (ASCE/SEI

7-22, 2021) contemplates the possibility to supplement the existing database of records with simulated ground motions.

3D physics-based wave propagation models that incorporate the characteristics of fault rupture, geological structure, and topography are gaining increasing interest in the engineering community for their capability to generate site-specific ground motions. This allows engineers to potentially have access to ground motions for any conceivable scenario and potentially incorporate the expected aleatory variability associated with a specific earthquake or earthquakes of interest (McCallen, Petersson, et al., 2021; McCallen, Petrone, et al., 2021).

Recent work carried out by Matinrad & Petrone (2023) discussed the implications of utilizing historical records and simulated ground motions in ASCE/SEI 7-compliant methods. Evidence from such analyses demonstrated that while the demand obtained from real ground motions tends to be distance-dependent for sites of the same class, the demand from simulated records is markedly site-specific, reflecting the concurrent effect of source, site, and path, with significant implications on structural design and assessment outcomes.

This work builds upon the results of that study and utilizes the ground motions selected and scaled following ASCE/SEI 7-compliant procedures and the response obtained from two reinforced concrete moment resisting frame buildings to analyze the probability of exceeding selected limit states when utilizing either historical records or site-specific simulated ground motions. Specifically, simulated ground motions from eight realizations of a magnitude 7 Hayward Fault strike-slip earthquake generated across a computational domain counting 402 (inland) stations and suites of 11 historical records selected for each station from the PEER-NGAW2 database are employed. Both sets of motions are scaled to site-specific MCE_R design spectra, leading to 30,552 nonlinear time-history analyses. The probabilistic seismic demand model (PSDM) is utilized to generate the fragility function, adopting the peak interstory drift ratio as the reference engineering demand parameter (Nguyen et al., 2023).

The fragility functions indicate that the probability of exceedance minor damage is comparable when using either set of motions (real or simulated). On the contrary, the probability of exceeding more severe damage states is larger when utilizing real rather than simulated motions.

3.2 Simulated Ground Motions and Building Structures

Figure 3.1A shows the 80-km x 30-km x 20-km computational domain modelled in SW4 (Seismic Waves, fourth order) to simulate eight realizations of an M7 Hayward Fault strike-slip event in the San Francisco Bay Area. The realizations differ from each other for the adopted rupture model (Graves & Pitarka, 2016). Figure 3.1B provides a representation of the rupture planes with slip distribution and hypocenter location (green star) for the considered eight cases. The physics-based models can resolve a maximum frequency of 5-Hz and a minimum shear-wave velocity of 500-m/s. However, the domain incorporates sites with shallow shear wave velocities as low as 100 m/sec (U.S. Geological Survey, 2020). Therefore, to fully capture the potential amplification and deamplification at soft and near-field sites, the simulated ground motions are processed with the empirical model proposed by Boore et al., (2014).

Two reinforced concrete special moment resisting frame buildings are considered as case study structures: namely, a 20-story and a 3-story building. Three-dimensional structures were designed following the ASCE/SEI 7-22, (2021) provisions with detailing conforming ACI318-19, (2019) in the ETABS for a site in Berkeley (CA). Middle frames were then extracted and modelled in OpenSees. A concentrated-plasticity modelling approach is utilized to simulate the nonlinear behaviour of the frame from linear to sidesway collapse (Ibarra et al., 2005). This research is taking advantage of computational efficiency of this kind of modelling since the numerous numbers of analyses need to be performed. The 3-story building has fundamental periods T1 = 0.78 sec, T2 = 0.21 sec, and T3 = 0.10 sec; while the 20-story building has fundamental periods T1 = 2.93 sec, T2 = 1.09 sec, T3 = 0.53 sec.

The peak inter-story drift ratio (PIDR) was utilized as the reference engineering demand parameter (EDP) to perform structural assessments. Specifically, the maximum of the median interstory drift ratio as obtained from the two populations of records (real and simulated ground motions) is utilized to assess and contrast structural performance.

3.3 Ground-Motion Selection and Scaling

Hazard deaggregation (USGS, 2017) was performed at each site across the computational domain to inform the selection of the real ground motions. Specifically, the magnitude and distance of the event(s) controlling the hazard at each site were utilized to center the range of variability of such parameters to utilize as search criteria in the PEER NGA-W2 database (Pacific Earthquake Engineering Research (PEER) Center, 2013). The site-specific target Maximum Considered Earthquake Spectrum (MCE_R) was derived at all the stations following the ASCE/SEI 7 procedures and the RotD100 of the motions selected from the PEER database were scaled to the design spectrum (2/3 of MCE_R) in the 0.2T1-2T1 bandwidth, where T1 represents the fundamental period of the structure under consideration. Upon completion of this process, the motions were sorted as a function of the calculated error in matching the design spectrum and first 11 motions showing the least error were selected. The selection of motions for each station was finalized adding consideration on the minimum expected number of impulsive motions, which was assessed with the model proposed by (Hayden et al., 2014), and by limiting the number of motions to two for each earthquake. The latter condition was imposed to avoid a very common condition for the selected region and event to have the database of real records dominated by one of the few large earthquake events for which near-filed records are available, such as Chi-Chi. The pairs of motions so attained (H1 and H2) were rotated to obtain the fault normal (FN) and fault parallel (FP) components utilizing the information available in the PEER database flatfiles.

These pairs of ground motions derived at each station of the computational domain are utilized to perform nonlinear time history analyses with two building structures and for the two separate components of the ground motion (fault normal and fault parallel), thus obtaining a total of 30,552 datapoints that will be utilized for the generation of the fragility functions.

As for the simulated records, while it will be desirable to have multiple simulations of the actual earthquake events controlling the hazard at the considered site, in this specific case study only realizations of an M7 earthquake were available. Since the hazard deaggregation indicates that the magnitude of the event controlling hazard at sites in the intended computational domain varies from 7.1 to 7.3, the RotD100 of the simulated motions were scaled to the same design target spectrum as the real records.

To start assessing the differences in ground-motion amplitudes (real vs simulated), Figure 3.2A and B show the regional-scale maps of the mean RotD50 spectral acceleration of the real (A) and simulated (B) suites of ground motions at the fundamental period of the 3-story building. The variation of the spectral acceleration across the computational domain demonstrates that, although site-specific procedures are followed to derive the MCE_R spectrum and select and scale real records, the variation of the spectral amplitudes is markedly distance dependent for sites following in the same class. It is for example seen that East of the Hayward Fault the spectral accelerations vary from about 1.3 g at sites located 2 km from the fault to about 1 g for sites at 8 km from the fault. A similar trend is observed West of the fault where; however, the geologic structure is slightly more heterogeneous, making the distribution of the spectral accelerations not strictly distance-dependent. On the contrary, the distribution of the spectral accelerations obtained from the simulated records is highly site-specific. It is for example seen that East of the Hayward Fault, Sa(T1) attains peak values of about 2.5 g for sites at about 2 to 4 km from the fault and minimum values of about 1 g at 6 km, owing to the incorporation of path, fault geometry, and site-condition effects.

The maps in Figure 3.3A and B show the distribution of the spectral acceleration of the RodD50 at the fundamental period of the 20-story structure for the real (A) and simulated (B) ground motions, demonstrating a pronounced difference in the site-to-site variability West of the Hayward fault.

3.4 Damage States (DS) Definition and Data Regression

HAZUS-MH, (2022) provides damage states definitions for structural and nonstructural components of buildings and is widely used to estimate the earthquake damage based on different EDPs.

The damage states employed in this study for the wo considered reinforced concrete SMRFs are shown in Table 3.1.

The strength of the ground motions applied to the structures can be quantified by various types of intensity measures (IMs). There are many studies investigating the best correlation between IMs and EDPs (Hancilar & Çaktı, 2015; Nguyen et al., 2023). A separate analysis conducted by the authors on the correlation between the PIDR for the considered buildings and different ground-motion IMs has demonstrated that the spectral acceleration at the fundamental period of each structure and the peak ground velocity show the strongest correlation with the building response. The spectral acceleration of at the fundamental period of the structure is herein employed.

Regression analyses is performed on 7,638 datapoint (real and simulated records) for each building and for each ground-motion component. The coefficient of determination (R^2) of the fitted line and logarithmic dispersion ($\beta_{D|IM}$) of the demand are shown in Figure 3.4 for the three-story building as an example to indicate the dispersion of the data. Similar trends are seen for the 20-story building but are not reported here for the sake of conciseness. The logarithmic dispersion is calculated based on the following equations(Jeon et al., 2015; Nguyen et al., 2023; Zhang et al., 2022):

$$S_{D\,|\,IM} = a.IM^b \tag{1}$$

$$\beta_{D\,|\,IM} = \sqrt{\sum_{i=1}^{n} \frac{[lnd_i - \ln\,(S_{D\,|\,IM})]^2}{n-1}} \tag{2}$$

where, $S_{D\,|\,IM}$ is the median value of the demand as function of IM, a and b are the parameters computed in the linear regression denoting the y-intercept and slope of the fitted line in log-log scale, d_i is the maximum seismic demand, and n is the number of the datapoints.

The cap on the PIDR of 4.5% seen in Figure 3.4 is related to the attainment of building collapse and numerical instability. Therefore, the nonlinear time-history analyses were stopped when a drift of 4.5% was achieved in the considered structures. The distribution of the data obtained from the real ground motions seen in Figure 3.4C and D for the two separate components is influenced by the record selection procedures. As explained earlier, although site-specific procedures are followed, for locations characterized by similar site conditions, similar populations of records were selected and scaled to spectra whose amplitudes decrease at increasing distance. As a result, the datapoints align in nearly straight lines for the real ground motions, reflecting the scaling of the same motions by different factors. Conversely, the ground motions obtained from the physics-based wave propagation models exhibit higher dispersion caused by the pronounced site-to-site variability and between-events variability (eight in this case).

3.5 Fragility Functions

Fragillity functions outline the probability that the seismic demand of the structure under consideration exceeds a predifined damage state at a specific level of the input motion (i.e., IM).

From the datapoints and damage states defiend earlier, fragility curves are calculated as follows(Cornell et al., 2002):

$$P(DS \geq DS_i|IM = X = S_aT_1) = \Phi(\frac{lnS_d(X) - \ln DS_i}{\beta}) \quad (3)$$

Where $P(DS|IM)$ is the probability of being at or exceeding a damage state (DS_i) in the specific intensity measure (IM), and the Φ operator is the standard normal cumulative distribution function. All the other symbols have the meaning explained earlier.

The structural responses obtained from the ground motion selected (real) and scaled (both real and simulated) as explained above, span a range of PIDRs, namely from approximately 0.3% to 4.5%. Therefore, three out of four DS, as presented in Table 3.1, are utilized in this study for the fragility analyses. Specifically, fragility curves are derived for the 3-story building for slight, moderate and complete damage (DS1, DS2 and DS3); while fragility curves for the 20-story structure are derived for moderate, extensive and complete damage (DS2, DS3 and DS4).

Figure 3.5 shows the fragility curves derived for the 3-story building with fault normal (A) and fault parallel (B) components of the ground motions. While slight differences are seen in the probability of exceeding DS1 and DS2 when comparing real and simulated records, significant disparities arise in DS3, with fragility functions derived from the real records being substantially steeper than those derived from the simulated records for both components of the ground motions.

The fragility functions developed for the 20-story building and shown in Figure 3.6 indicate very similar trends for DS2 and DS3 and for both components, and more pronounced differences in the probability of exceeding DS3 in the FN components only. The fragility functions derived with the real ground motions are again seen to be steeper than those derived with the simulated records, leading to a mean probability of exceeding DS3 for a spectral acceleration of about 1.6 g for the real motions and 2 g for the simulated motions for the fault normal component, and for a spectral acceleration of about 1.8 g for the real records and about 2 g for the simulated records for the fault parallel component

3.6 Conclusion

This study investigated the implications of utilizing site-specific simulated ground motions and historical records selected and scaled following ASCE/SEI 7-compliant site-specific procedures on probabilistic seismic demand analysis. Eight events of an M7 Hayward Fault earthquake simulated across a computational domain covering the San Francisco Bay Area and the PEER-NGA W2 database are utilized as the sources for ground motion selection and scaling. Two reinforced concrete special moment resisting frame buildings are utilized as a case study structures. The spectral accelerations at the fundamental period of each structure and peak inter-story drift ratio are adopted as the target intensity measure and engineering demand parameter, respectively, for generating fragility functions.

The fragility curves are derived from a total of 30,522 datapoint (nonlinear time-history analyses) and demonstrate a higher probability of exceeding extensive and complete damage states for real ground motions compared to simulated ground motions for the 3-story and 20-story buildings, respectively. It's worth mentioning that fragility curves provide an overall perspective of the seismic demand the structures are expected to be subject to. That is, although the fragility functions are showing higher probability of exceeding extensive and complete damage when real, instead of simulated, ground motions are used, site-specific regional-scale analyses demonstrate a very pronounced site-to-site variability in the demand when two populations of motions are used, pointing to differences (underestimated and overestimates) that are difficult to predict when ASCE7-compliant methods with historical records are utilized (Matinrad & Petrone 2023) and thus pointing to potential misestimates deriving from the use of records that do not necessarily reflect the conditions of the region under consideration.

3.7 References

ACI318-19. (2019). American Concrete Institute 318-19 Building Code Requirements for Structural Concrete and Commentary. In *318-19 Building Code Requirements for Structural Concrete and Commentary*. https://doi.org/10.14359/51716937

ASCE/SEI 7-22. (2021). Minimum Design Loads and Associated Criteria for Buildings and Other Structures. In *Minimum Design Loads and Associated Criteria for Buildings and Other Structures* (ASCE/SEI 7). American Society of Civil Engineers. https://doi.org/10.1061/9780784415788

Boore, D. M., Stewart, J. P., Seyhan, E., & Atkinson, G. M. (2014). NGA-West2 Equations for Predicting PGA, PGV, and 5% Damped PSA for Shallow Crustal Earthquakes. *Earthquake Spectra*, *30*(3), 1057–1085. https://doi.org/10.1193/070113EQS184M

Cornell, C. A., Jalayer, F., Hamburger, R. O., & Foutch, D. A. (2002). Probabilistic basis for 2000 SAC federal emergency management agency steel moment frame guidelines. *Journal of Structural Engineering*, *128*(4), 526–533.

Graves, R., & Pitarka, A. (2016). Kinematic ground-motion simulations on rough faults including effects of 3D stochastic velocity perturbations. *Bulletin of the Seismological Society of America*, *106*(5), 2136–2153.

Hancilar, U., & Çaktı, E. (2015). Fragility functions for code complying RC frames via best correlated IM–EDP pairs. *Bulletin of Earthquake Engineering*, *13*(11), 3381–3400. https://doi.org/10.1007/s10518-015-9775-5

Hayden, C. P., Bray, J. D., & Abrahamson, N. A. (2014). Selection of near-fault pulse motions. *Journal of Geotechnical and Geoenvironmental Engineering*, *140*(7), 04014030.

HAZUS-MH. (2003). Multi-hazard loss estimation methodology: earthquake model, technical report. In *Department of Homeland Security, FEMA, Washington, …*. Department of homeland security, FEMA. http://scholar.google.com/scholar?cluster=11618114585157572557&hl=en&oi=scholarr#0

Ibarra, L. F., Medina, R. A., & Krawinkler, H. (2005). Hysteretic models that incorporate strength and stiffness deterioration. *Earthquake Engineering \& Structural Dynamics*, *34*(12), 1489–1511. https://doi.org/https://doi.org/10.1002/eqe.495

Jeon, J.-S., Lowes, L. N., DesRoches, R., & Brilakis, I. (2015). Fragility curves for non-ductile reinforced concrete frames that exhibit different component response mechanisms. *Engineering Structures*, *85*, 127–143. https://doi.org/https://doi.org/10.1016/j.engstruct.2014.12.009

Matinrad, P., & Petrone, F. (2023). ASCE/SEI 7-compliant site-specific evaluation of the seismic demand posed to reinforced concrete buildings with real and simulated ground motions. *Earthquake Engineering and Structural Dynamics*, *52*(15), 4987–5009. https://doi.org/10.1002/eqe.3995

McCallen, D., Petersson, A., Rodgers, A., Pitarka, A., Miah, M., Petrone, F., Sjogreen, B., Abrahamson, N., & Tang, H. (2021). EQSIM—A multidisciplinary framework for fault-to-structure earthquake simulations on exascale computers part I: Computational models and workflow. *Earthquake Spectra*, *37*(2), 707–735. https://doi.org/10.1177/8755293020970982

McCallen, D., Petrone, F., Miah, M., Pitarka, A., Rodgers, A., & Abrahamson, N. (2021). EQSIM—A multidisciplinary framework for fault-to-structure earthquake simulations on exascale computers, part II: Regional simulations of building response. *Earthquake Spectra*, *37*(2), 736–761. https://doi.org/10.1177/8755293020970980

Nguyen, H. D., Shin, M., & LaFave, J. M. (2023). Optimal intensity measures for probabilistic seismic demand models of steel moment frames. *Journal of Building Engineering*, *65*, 105629. https://doi.org/https://doi.org/10.1016/j.jobe.2022.105629

Pacific Earthquake Engineering Research (PEER) Center. (2013). *NGA-West2 Grond Motion Database*. https://ngawest2.berkeley.edu/

Pang, Y., & Wang, X. (2021). Cloud-IDA-MSA conversion of fragility curves for efficient and high-fidelity resilience assessment. *Journal of Structural Engineering*, *147*(5), 4021049.

USGS. (2017). *Unified Hazard tool*. https://earthquake.usgs.gov/hazards/interactive/

Zhang, W., Liu, S., Shokrabadi, M., Dehghanpoor, A., & Taciroglu, E. (2022). Nonlinear seismic fragility assessment of tall buildings equipped with tuned mass damper (TMD) and considering soil-structure interaction effects. *Bulletin of Earthquake Engineering*, *20*(7), 3469–3483. https://doi.org/10.1007/s10518-022-01363-6

Table 3.1. Defined four damage states based on PIDR.

Damage States (DS)	20-Story PIDR (%)	3-Story PIDR (%)
DS1. Slight	0.25	0.5
DS2. Moderate	0.5	1.0
DS3. Extensive	1.5	3.0
DS4. Complete	4.0	8.0

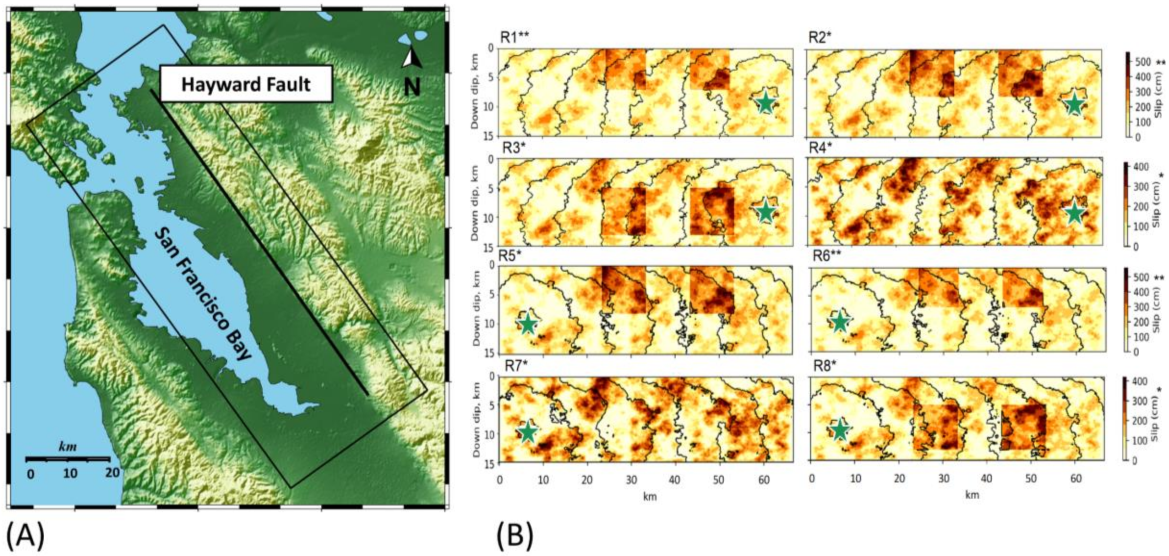

Figure 3.1. A) The computational domain over San Francisco Bay Area. B) Slip distribution of the rupture models and the hypocentre location for the eight realizations of the simulated ground motions.

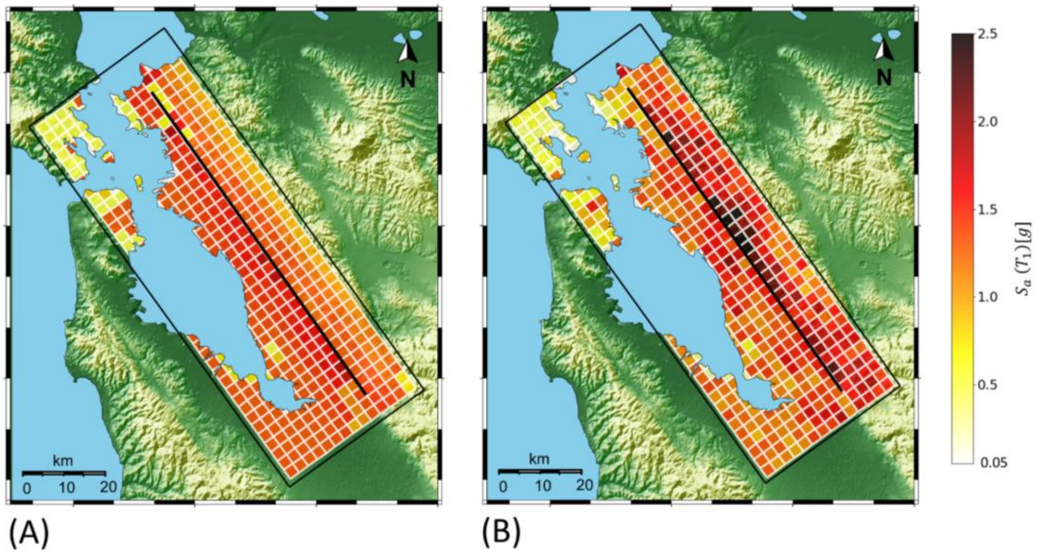

Figure 3.2. Mean RotD50 spectral acceleration at the fundamental period of the 3-story building. A) Real ground motions B) Simulated ground motions.

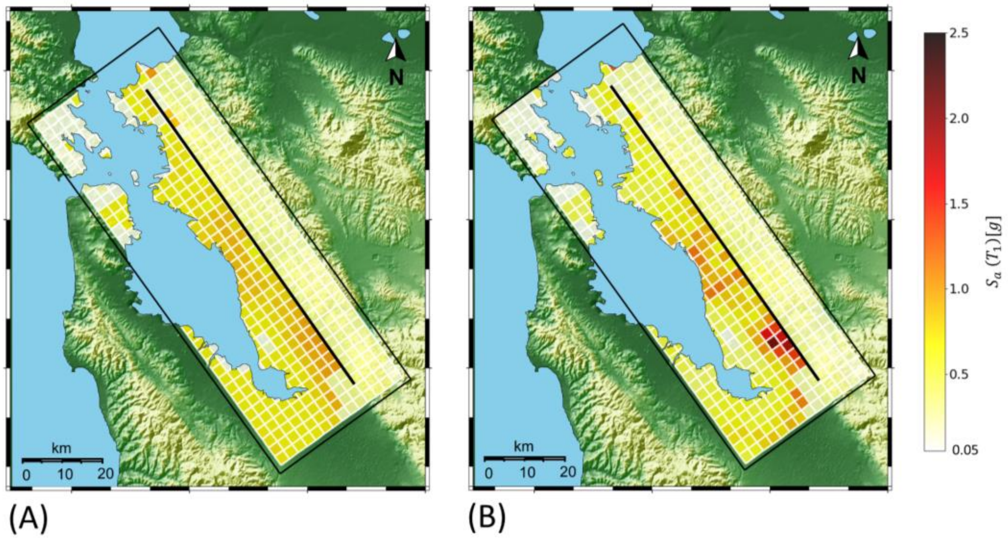

Figure 3.3.3. Mean RotD50 spectral acceleration at the fundamental period of the 20-story building. A) Real ground motions B) Simulated ground motions.

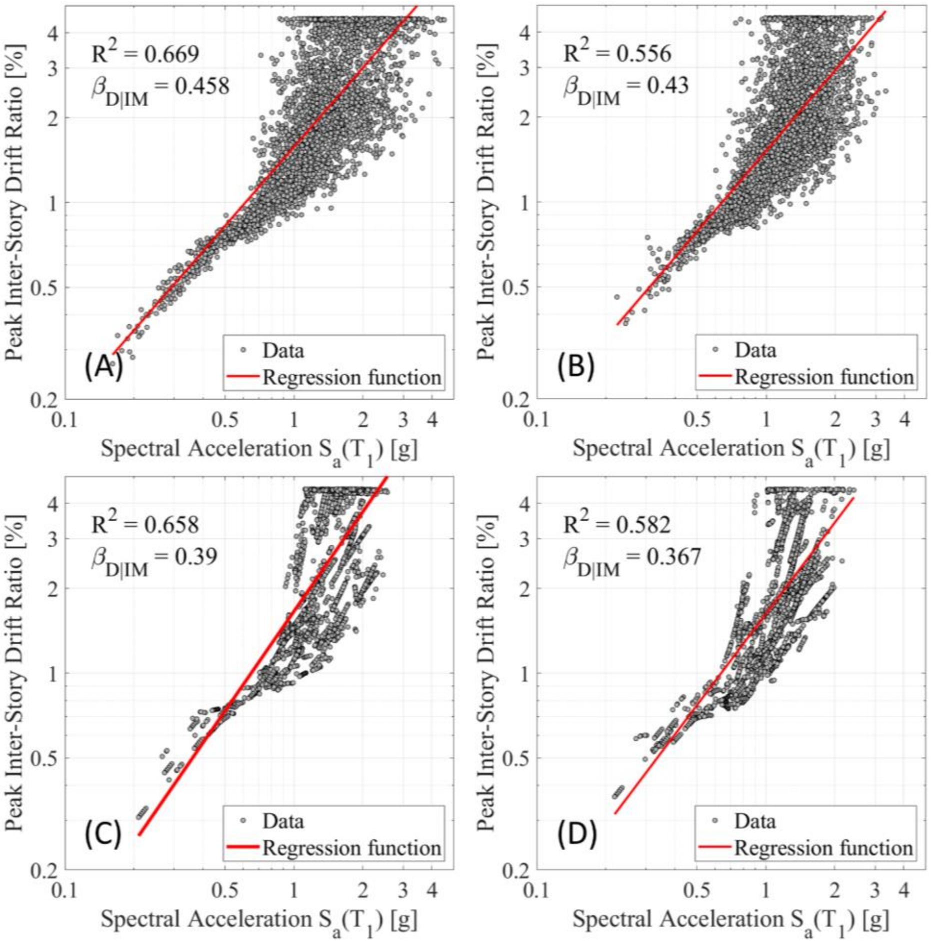

Figure 3.3.4. PIDR versus $S_a(T_1)$ correlation for 3-Story building A) simulated ground motions FN. B) simulated ground motions FP. C) real records FN. D) real records FP.

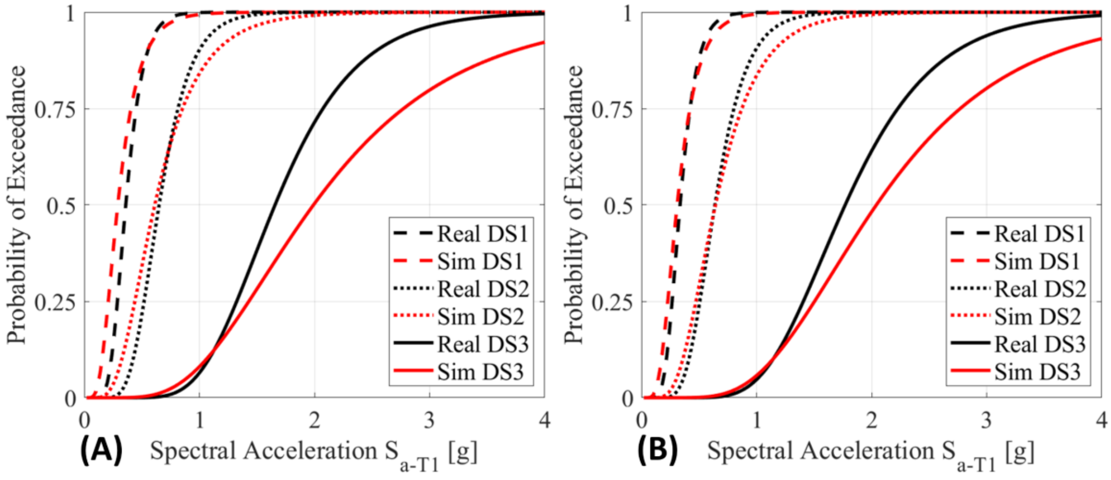

Figure 3.5. Fragility curves of real and simulated ground motions based on PIDR for 3-Story building considering 3 damage states A) Fault Normal. B) Fault Parallel.

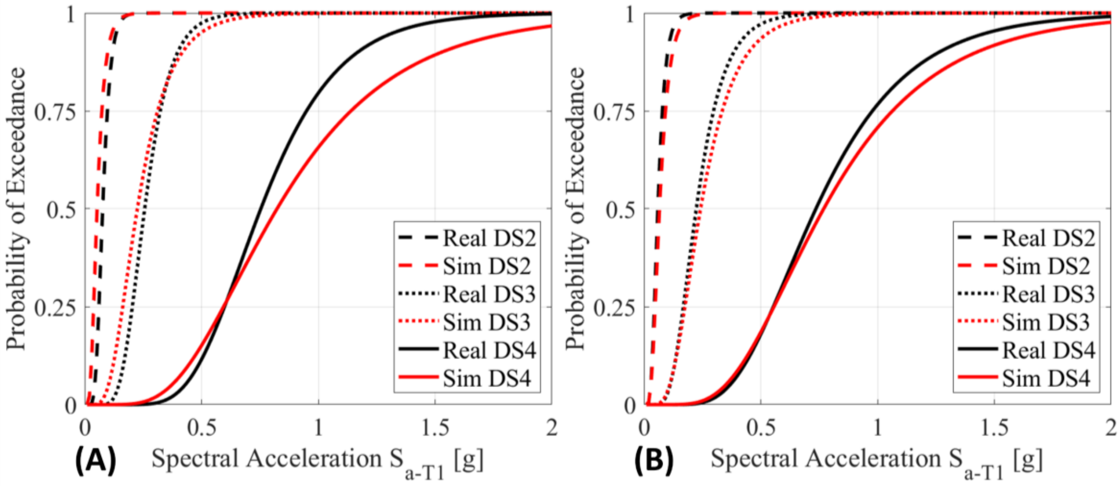

Figure 3.6. Fragility curves of real and simulated ground motions based on PIDR for 20-Story building considering 3 damage states A) Fault Normal. B) Fault Parallel.

4 EFFECT OF SOFT SEDIMENTS MODELING ON THE SEISMIC RESPONSE OF A 3D MID-RISE RC BUILDING: HIGH-RESOLUTION PHYSICS-BASED GROUND-MOTION SIMULATIONS VERSUS EMPIRICAL FACTORS

This chapter of the dissertation is submitted and is being reviewed in the journal of Earthquake Spectra.

Abstract

Physics-based ground motions have progressively become a key resource in earthquake engineering. Nevertheless, the challenge of accurately simulating ground motions in regions with low shear-wave velocities, such as basins and shallow sediments, persists and is often constrained by the associated computational demands. Motivated by the potential unavailability of a suite of simulations resolving low velocities for a specific region or site of interest, this work assesses the implications of using different approaches for modeling low shear-wave velocities on structural response evaluations. Two methods are investigated: one relies on simulation models capable of resolving low shear-wave velocities, while the other combines simulations that resolve high shear-wave velocities with empirical site amplification factors. An M7 Hayward Fault strike-slip earthquake in the San Francisco Bay Area and a three-dimensional ten-story reinforced concrete building are utilized as the case study. Findings from this work demonstrate significant disparities in the prediction of ground-motion intensity measures and building responses (from moderate to extensive) when different modeling methods are utilized. Such differences

manifest at sites with low shear-wave velocities as well as at stiff sites in their vicinity. This is caused by the concurrent effect of the specificity of the seismic velocity structure of the considered region and wave propagation, which is adequately captured only by the simulation model incorporating the (target) low shear-wave velocity. Evidence from this study suggests that empirical factors should be used and processed with consideration for the specific geological characteristics of the domain of interest, especially in regions lacking representation in historical record databases. From a structural engineering perspective, these insights contribute to a better understanding of the complexities involved in soft sediment modeling and its implications in structural engineering applications.

4.1 Introduction

Numerical simulations have become an established tool for carrying out a spectrum of analyses aimed at improving seismic structural performance evaluations at both local and regional scales. The progressive integration of high-performance computing architectures with physics and mechanics-based simulation codes has enabled the possibility to study complex models incorporating the three-dimensional effects of earthquake source, propagation paths, local site conditions to eventually obtain statistics of structural systems response.

Historical events, such as the 1985 Mexico City (Campillo et al., 1989) and the 1989 Loma Prieta (Hanks & Krawinkler, 1991) earthquakes, have in fact demonstrated that the three-dimensional effects occurring in basins and sedimentary valleys can amplify the motions by up to five times, increase their duration by up to 30 seconds compared to rock, and lead to significant site-to-site variability. A correct representation of the three-dimensional crustal structure is therefore crucial for capturing the combined effects of wave propagation and local site conditions and their impact on the built environment. This includes embodying soft deposits characterized by low shear wave velocities (Vs) where the resonance of shallow layers can cause amplification of the seismic waves, and potential soil nonlinearities can de-amplify the motions at high frequencies as an effect of increased damping ratio under large strains induced by strong shaking.

However, earthquake simulations performed on realistic heterogeneous media pose enormous demands on the computational resources required for solving Navier's equations of elastodynamics and potentially incorporating soil nonlinearities. Such demands increase with the minimum local mesh size, h_{min}, needed for the minimum wavelength, that is $h_{min} = V_{s,min}/(f_{max} \times PPW)$, where $V_{s,min}$ and f_{max} are the minimum shear wave velocity and the maximum frequency that the simulation model can resolve, respectively, and PPW is the number of grid points per wavelength. Therefore, for a constant PPW, the lower the resolved shear wave velocity (or the higher the frequency resolution), the smaller h_{min}, and the larger the computational burden to perform the simulation. Moreover, the finer the mesh size, the smaller the required time step, and thus the longer the running time, leading to more CPU hours and larger memory requirements. As a result, balancing accuracy and efficiency becomes essential when modeling large-magnitude earthquakes in highly heterogeneous media, where under-sampling would result in inaccurate solutions for soft soils, and over-sampling would likely cause computational and storage overburdens.

Numerous techniques have been developed and successfully implemented to optimize the mesh grid refinement and the resulting computational load. For example, Bao et al. (1996) developed an elastic wave propagation finite element-based simulator incorporating an unstructured mesh generator that tailors the mesh size to the local wavelength in large-scale sedimentary basins. Taborda et al. (2010) generated a parallel earthquake simulator (Hercules) employing an adaptive scalable octree-based approach for generating finite element unstructured meshes fitted to the local wavelength. More recently, McCallen et al. (2021) implemented into SW4 (Sjögreen & Petersson, 2012) a mesh refinement scheme operating on a combined Cartesian and curvilinear grid, which allows to adapt the computational grid size to the depth-dependent wavelength (EQSIM). Simulation schemes have also been developed to incorporate soil nonlinear geomechanics. To cite some, Paolucci et al. (2014) extended the equivalent linear approach used in one-dimensional analyses to account for the shear modulus reduction (G/G_{max}) and increased damping ratio as a function of the shear strain to three-dimensional stress conditions (BB-SPEED). Roten et al. (2012) utilized an approach based on the combined use of linear broadband simulated ground motions and the result of nonlinear one-dimensional simulations in NOAH (Bonilla et al., 2005) to estimate the impact of soil nonlinearities at frequencies above 1-Hz and derive correction functions to apply to the case study linear motions (i.e., Salt Lake Basin). However, while theoretically rigorous and computationally executable, such approaches require the definition of many weakly constrained or unknown parameters that introduce large uncertainties in the generated motions, particularly if the intent is to utilize numerical models in domains outside the range of available data. These include very near-source, large magnitude events, and regions that have been seismically non-active, yet are highly populated and thus most relevant for hazard and risk evaluations.

Although the cited works, among others, have marked fundamental milestones in the capability to simulate earthquake ground motions, the possibility to fully execute such codes to simulate large magnitude events on (consequently) large computational domains remains tied to the use of world-class high-performance computers.

An alternative approach for simulating ground motions that incorporate soft sediments and basins, while containing the computational burden, would entail combining less computationally demanding physics-based models with existing empirical site-response correction factors.

Motivated by the progressive integration of simulated ground motions in engineering domains (ASCE/SEI7, 2022) (Matinrad & Petrone, 2023) and the potential unavailability of a suite of ground-motion simulations resolving low velocities for a specific region or site of interest, this work aims to provide the basis for assessing the implications of using different approaches for modeling low shear-wave velocity layers on structural response evaluations.

The region and earthquake selected for this study are the San Francisco Bay Area and an M7 Hayward Fault strike-slip earthquake. Two sets of simulated ground motions are utilized, one that can resolve a minimum shear-wave velocity ($V_{s,min}$) of 250-m/sec and one resolving 500-m/sec. Two empirical (ergodic) ground-motion models (GMMs) are employed to obtain the site-response correction factors. A three-dimensional reinforced concrete ten-story building is utilized as a representative mid-rise building to conduct structural response assessments. Comparisons of the ground-motion predictions are conducted in terms of ground-motion intensity measures (IMs) relevant to the response of the considered building. The differences in the structural responses are evaluated in terms of maximum interstory drift ratio (IDR) and global rotation (torsion).

Results show fundamental differences in the prediction of ground-motion intensities and building response across the considered modeling approaches in terms of capability to capture the site-to-site variability and the absolute demands (interstory drift ratio and torsion). This is observed at sites with $V_s < V_{s,min}$ as well as at stiffer sites in their vicinity.

4.2 Ground-Motion Simulations

An M7.0 strike-slip Hayward Fault crustal earthquake was simulated in SW4 (Sjögreen & Petersson, 2012) across the 80-km x 120-km x 40-km domain in the San Francisco Bay Area represented in Figure **4.1**-A. Two simulation models were utilized: one model is characterized by a $V_{s,min}$ of 250-m/sec, the other by a $V_{s,min}$ of 500-m/sec. Both simulation models incorporate three-dimensional variations in material properties, surface topography, and inelastic attenuation through P- and S-wave frequency-independent quality factors that are related to the V_s at the considered site (grid point). Both models employ the Graves & Pitarka (2016) kinematic rupture generator with slip distribution, rise time, and 4-Hz slip rate depicted in Figure **4.1**-B. The rupture plane combines a stochastic distribution of the slip parameters and one discrete 23-km x 8-km patch with high slip (Pitarka et al., 2019). In both models, the rupture is assumed to initiate at a point located 7-km from the southern tip of the fault and at a depth of 8-km (the hypocenter represented by the green star in Figure **4.1**-B). The USGS geologic and seismic velocity model (v21.1) (Aagaard & Hirakawa, 2021) with modifications introduced by Nakata et al. (2023) was employed to represent the three-dimensional variations in material properties and topography across the domain. Broadband fully deterministic ground motions were generated across a combined Cartesian and curvilinear mesh grid with 8 PPW, resulting in 1.26E^{10} billion grid points for the model with $V_{s,min}$ = 500-m/sec and 2.96E^{10} billion grid points for the model with $V_{s,min}$ = 250-m/sec to achieve a target frequency resolution of 5-Hz. Since the response spectra are sensitive to motions above and below 25% of the target period, the shortest spectral period shown in the forthcoming analyses is 0.3-sec. Both models were simulated on the U.S. Department of Energy Perlmutter supercomputer (NERSC-9).

Figure **4.2**-A illustrates the distribution of the time-averaged shear wave velocity in the upper 30-m (V_{s30}) across the computational domain as obtained from the USGS velocity model (Aagaard & Hirakawa, 2021). Overall, the area characterized by $V_s < V_{s,min} = 500$-m/sec covers about 30% of the inland portion of the computational domain, noteworthy corresponding to the most densely populated region in the San Francisco Bay Area.

Figure **4.2**-B shows the distribution of the depth to the first occurrence of shear-wave velocity of 1-km/sec (Z1.0), demonstrating that the region is characterized by shallow soft sediments, with Z1.0 ranging from approximately 0.1-km to 0.6-km, except for the Pleasanton-Livermore Valley where the average Z1.0 is about 1.5-km. These features of the geological structure characterizing the San Francisco Bay Area will be instrumental to interpret the differences in the ground-motion amplitudes when utilizing a purely simulation-based approach and simulations processed with empirical factors.

The three components of the surface ground motions were sampled on a grid with 2-km spacing, yielding a total of 2,301 three-component motions. Only the horizontal components of the inland stations were analyzed in this study, corresponding to 1942 pairs. The orthogonal horizontal components oriented parallel and normal to the fault were utilized as an input for the three-dimensional building structure.

The ground motions generated from the computational domain represented in Figure **4.1**-A are herein compared against the NGA-W2 ground-motions models (GMMs) to assess their realistic character (Petrone et al., 2020, 2021). The median properties of the computational domain (i.e., Vs30, Z1.0, etc.) are utilized to calculate the GMMs predictions (median and standard deviation). Specifically, the calculation of the median V_{s30} for the computational domain is performed considering the resolved $V_{s,min}$ (250-m/sec or 500-m/sec), while the input V_{s30} for the GMMs is obtained from (Aagaard & Hirakawa, 2021) with modifications by Nakata et al. (2023) to represent the actual properties of the region. With this approach, it is possible to verify whether the simulation model can produce ground-motion intensity measures in agreement with those predicted by the empirical models. Figure **4.3**-A and 3-B show the comparison of the PSAs in the 0.3 – 10-sec spectral bandwidth as obtained from the GMMs and the simulated motions with $V_{s,min}$ of 500-m/sec and 250-m/sec, respectively, for the two separate components (fault normal, FN, in red; and fault parallel, FP, in blue). The median spectral amplitudes are within +/- 1 sigma across all spectral periods, providing confidence in reliable average predictions of the PSAs. Figure **4.3**-C and D show the variation of the PGV for the two separate components of the ground motions as a function of the Joyner-Boore distance from the fault (R_{jb}) for the simulations with a $V_{s,min}$ of 500-m/sec and 250-m/sec, respectively. Comparisons show that the predictions of the empirical models are centered on the simulated PGV values, with deviations from the average occurring at sites affected by the concurrent effects of forward directivity, increased ground motion intensities resulting from the localized effect of concentrated slip in the deterministic patches, and basin focusing phenomena. A comprehensive assessment of the motions utilized in this study can be found in (Petrone et al., 2024).

To help interpret the extent of the differences introduced by the $V_{s,min}$ on the Vs30 calculations in the computational domain utilized in this study, Figure **4.4** provides a representation of the velocity profiles at two sites.

One site is in the (A) Santa Clara Valley (SC hereafter), and the other is in the (B) Pleasanton-Livermore Valley (PL hereafter). The dotted black lines represent the original velocity profile obtained from the USGS seismic velocity model (v21.1) (Aagaard et al., 2008), and the dotted red and green lines are the profile obtained when $V_{s,min}$ = 500-m/sec and 250-m/sec, respectively. Therefore, whenever the actual V_s (USGS model) is lower than $V_{s,min}$, the modeled V_s will be equal to the $V_{s,min}$. The profiles modeled in SW4 utilize linear interpolation between velocities and are represented by solid lines.

Based on these profiles, the following Vs30 values are obtained: for SC, $V_{S30,USGS} = 81\ m/sec$, $V_{S30,250}$ = 250 m/sec, and $V_{S30,500} = 500\ m/sec$; while for PL $V_{S30,USGS} = V_{S30,250} = 401\ m/sec$, and $V_{S30,500} = 500\ m/sec$.

4.3 Empirical Ground-Motions Models and Simulated Ground-Motion Modification

Two widely used empirical models are utilized to incorporate the site effects into the simulated ground motions with $V_{s,min}$ = 500-m/sec.

The first model is the one proposed by Boore et al. (2014) - hereafter BSSA14 - for shallow crustal earthquakes. BSSA14 provides the median (and standard deviation) of the average horizontal component 5% damped pseudo-spectral acceleration (PSA), peak ground acceleration and velocity (PGA and PGV). It is obtained utilizing the PEER NGA-West 2 database of records (Ancheta et al., 2014) and it is applicable to earthquakes of magnitude of 3.0 to 8.5, distances ranging from 0 to 400-km, time-averaged Vs30 from 150 to 1500-m/sec, and periods ranging from 0.01 to 10-s. The site function incorporates the contributions of both linear and nonlinear components of site amplification. The linear component represents the scaling of ground motion with Vs30 for linear soil response; the nonlinear component is a function of the median horizontal PGA for reference rock and the degree of nonlinearity expressed as a function of Vs30. The PGA so calculated is utilized in this study.

The second model is the one proposed by Bayless & Abrahamson (2018) - hereafter BA18 - for shallow crustal earthquakes in California and Nevada. BA18 is based on the combined use of the NGA-W2 database and finite-fault simulations performed with the SCEC Broadband Platform (Maechling et al., 2015) to constrain the near-fault large-magnitude scaling and nonlinear site amplification (Hashash et al., 2018). Differently from BSSA14, AB18 is developed for the smoothed effective amplitude spectrum (EAS), defined as the orientation-independent horizontal component FAS of the ground acceleration. The EAS is defined as $EAS(f) = \sqrt{\frac{1}{2}[FAS_{HC1}(f)^2 + FAS_{HC2}(f)^2]}$, where FAS_{HC1} and FAS_{HC2} are the FAS of the two orthogonal horizontal components of the ground motion, and f is the frequency in Hz. This model is considered applicable for rupture distances 0 - 300 km, magnitude 3.0 - 8.0, frequencies 0.1-100 Hz, and Vs30 180-1500 m/sec. The term utilized to correct the simulated ground motions site effects is $f_s = f_{SL} + f_{NL}$, where f_{SL} is the linear site amplification determined by regression analysis that scales linearly with ln (V_{S30}); and f_{NL} is the nonlinear site amplification obtained from a purely analytical model (Hashash et al., 2018).

Although the Vs30 in the adopted velocity model attains values below 100-m/sec (see Figure **4.2**-A), the simulated motions with $V_{s,min}$ = 500-m/sec are processed with the empirical factors to achieve a minimum target Vs30 of 250-m/sec, making both empirical models applicable to this study. This is to provide a consistent comparison between the ground motions generated by a numerical model that can resolve shear-wave velocities as low as 250-m/sec and an approach that combines the motions from a numerical model resolving a minimum shear-wave velocity of 500-m/sec modified with empirical factors.

To process the simulated ground motions, transfer functions (TF) are derived as spectral ratios, determining how each spectral period (or frequency) is amplified by the soil deposits. That is, $TF(T_i) = S_{target}\left(T_i, V_{S30,T}\right)/S_{original}\left(T_i, V_{S30,O}\right)$, where T_i is the spectral period of interest, $S_{target}\left(T_i, V_{S30,T}\right)$ is the spectral amplitude (either PSA or FAS, depending on the model) for the target Vs30 ($V_{S30,T}$), and $S_{original}\left(T_i, V_{S30,O}\right)$ is the spectral amplitude for the original Vs30 ($V_{S30,O}$) (Kramer, 1996). For each station in the computational domain, the following steps are taken to process the ground motions: (1) extract the site-specific input parameters to utilize as an input for the empirical models from the metadata associated with the simulated ground motions (i.e., $V_{S30,O} = V_{S30,500}$, and $V_{S30,T} = V_{S30,250}$, Z1.0, etc.); (2) calculate $TF(T_i)$ for both empirical models and taper it to unity from 5 to 10 sec period to mitigate the potential for overamplification of the longer periods, which are already included to a certain extent in the deterministic model (R. W. Graves & Pitarka, 2010); (3) multiply each term of the Fourier series of the two separate components of the simulated ground motions (fault normal and fault parallel) with $V_{s,min}$ = 500-m/sec by $TF(T_i)$ to produce the Fourier series of the ground surface motion with $V_{S30,T}$; (4) derive the ground motion incorporating the effect of softer soil in the time domain using the inverse Fast Fourier Transform.

4.4 Building Model

A three-dimensional ten-story reinforced concrete (RC) building located at a site in Berkeley (CA) with soil type D was designed following the provisions of (ASCE-7, 2016) and (ACI (American Concrete Institute, 2019) for risk category II. This building is selected as representative of a typical mid-rise structure in the San Francisco Bay Area. Factored self-weight, superimposed dead loads, and live loads were utilized in the load combinations for structural design. Building elevation and plan are represented in Figure **4.5**. The building utilizes special moment resisting frames as lateral-force-resisting system in the two principal directions.

A reduced-order modeling scheme was utilized to create a simulation model of the building with the OpenSees software (Zhu et al., 2018). Force-based fiber-section elements were employed to model beams and columns in both directions. Material nonlinearities were introduced by assigning nonlinear constitutive relationships to concrete and steel, namely Conrete01 and Steel01 with 7% isotropic hardening. Normal strength concrete with $f'_c = 6.9MPa$ $(5\ ksi)$ and grade 60 steel were utilized. The properties of confined concrete were calculated based on the actual confinement provided by the transverse reinforcement with the relationships proposed by (Mander et al., 1988). Geometrical nonlinearities were incorporated through the consideration of P-Delta effects. Beams and columns were discretized into four elements and the Gauss-Lobatto integration scheme with five-point integration along the element length was utilized. A consistent mass matrix was created for the bare frame through the definition of elements geometry and material mass density, while the additional mass representing slabs self-weight and superimposed dead loads was simulated through concentrated masses lumped at the beam nodes. Rayleigh damping with damping ratio of 5% anchored to the structure first and third modes was utilized. The building model was fixed at the base, thus excluding considerations related to soil-structure interaction. While it is recognized that this simplifying assumption may introduce approximations in the assessment of the building response, it ensures consistency in the comparison of the structural performance obtained across different modeling approaches for the soft sediments and shallow basins across the considered computational domain. With such features, the building has fundamental periods $T_1 = 1.7\ sec$ (transverse mode in the X direction with 78% participating mass), $T_2 = 1.5\ sec$ (longitudinal mode in the Y direction with 79% participating mass), and $T_3 = 1.4\ sec$ (torsional mode with 79% participating mass).

The engineering demand parameters (EDPs) utilized to assess the structural response are the peak interstory drift ratio (PIDR) and the global torsion (φ). Specifically, $PIDR = \max(\Delta_n)$, where $n = 1,2,..10$ is the number of stories, and $\Delta_n = \sqrt{\Delta_{X_j}^2 + \Delta_{Y_j}^2}$, with $j = 1, 2, 3, 4$ being the building corners, and Δ_{X_i} and Δ_{Y_i} are the drift ratios calculated along each component (X and Y) at each corner i. Global torsion did not demonstrate to be critical and therefore the regional-scale maps of the torsion are reported in the supplemental material only (Figure 4.17).

4.5 Ground-Motion Intensity Measure Estimates with Different Modelling Approaches

The effects of the correction for both linear and nonlinear effects on the ground motions are herein analyzed with respect to the IMs relevant to the response of the case study structure: namely, PSA(T1) and PSA(T2), where T1 and T2 are the fundamental periods of the building in the two principal directions, and PGV.

To visualize the differences in the prediction of the considered IMs across the computational domain, maps of both the absolute values and the ratio of the IMs predicted by the different modeling approaches to the IMs predicted by the simulated ground motions with $V_{s,min}$ = 500-m/sec are generated and discussed.

Figure **4.6** A through D show the distribution of the PSA(T2) for the fault normal component of the ground motions across all modeling approaches. Specifically, (A) and (B) show the PSA(T2) obtained from the simulation models characterized by $V_{s,min}$ = 500-m/sec and 250-m/sec, respectively; while (C) and (D) show the PSA(T2) obtained from the simulation model with $V_{s,min}$ = 500-m/sec and processed with the BSSA14 and BA18 empirical factors, respectively, to obtain the same V_{S30} calculated with $V_{s,min}$ = 250-m/sec. The spectral accelerations at T2 = 1.5-sec are seen to vary significantly across the domain for all modeling approaches. Generally, larger values of the PSA and for a significantly larger number of stations are seen when the motions are processed with the empirical models rather than obtained from simulations that resolve a $V_{s,min}$ of 250-m/sec. The maps of the PSA(T1) for the fault parallel component of the ground motions can be found in the supplemental material (Figure 4.18).

Figure **4.7** shows the regional-scale maps of the ratio of the PSA at T1 = 1.7-sec (top row) and T2 =1.5-sec (bottom row) obtained from the simulated ground motions with $V_{s,min}$ = 250-m/sec to the simulated motions with $V_{s,min}$ = 500-m/sec ($R_{PSA,Sim}$ in A and D); the simulated ground motions with $V_{s,min}$ = 500-m/sec processed with the BSSA14 empirical factors to the simulated motions $V_{s,min}$ = 500-m/sec ($R_{PSA,BSSA14}$ in B and E); and the simulated ground motions with $V_{s,min}$ = 500-m/sec processed with the BA18 empirical factors to $V_{s,min}$ = 500-m/sec, ($R_{PSA,BA18}$ in C and F). Colors towards brown indicate that the PSA obtained when the sediments with low V_s are modeled using a $V_{s,min}$ of 250-m/sec is larger than that obtained when a $V_{s,min}$ of 500-m/sec is employed; likewise, colors toward purple signify that the PSA is smaller than that obtained when $V_{s,min}$ = 500-m/sec; finally, white indicates a ratio of one, pointing to an unmodified PSA at the considered spectral period. For the sake of conciseness, only the maps showing the PSA ratios for the fault normal component are presented and commented. However, the considerations made for such component hold for the parallel component too, and the corresponding maps are reported in the supplemental material (Figure 4.19).

The information in Figure **4.2**-A and in Figure **4.7** demonstrates that, es expected, the spectral accelerations are modified in all the areas where the Vs30 calculations are affected by the cap on the $V_{s,min}$ = 500-m/sec, which impedes the frequency dependent progress of linear amplification at the soft sites as discussed in (Rodgers et al., 2020). However, when the purely simulation-based approach is employed (Figure **4.7**-A), modifications to the PSA are observed also at sites that are not directly affected by the cap on the $V_{s,min}$ but are in the direction of waves that travel through sites with Vs30 affected by the cap on the $V_{s,min}$. As expected, such phenomenon is captured by the purely simulation-based approach only, which can fully model event and region-specific path effects. As an example, the sites towards the south-west edge of the computational domain are characterized by stiffer soil with $V_{S30}{\sim}500\ m/sec$ and reside next to sites with soft shallow layers (west of the fault) with $V_{S30,USGS}{\sim}100\ m/sec$ and $V_{S30,250} = 250\ m/sec$. $R_{PSA,Sim}$'s < 1 (light purple stations at 20 to 30-km from the fault) demonstrate that the motions are modified not only strictly based on the local site conditions, but also by wave path effects across softer sedimentary layers. A further example of this effect can be seen for a small population of stations located south of the Pleasanton-Livermore Valley, towards the south-east edge of the computational domain, where the $R_{PSA,Sim}$ attains values above unity (light brown stations). In addition, the $R_{PSA,Sim}$ maps demonstrate a pronounced site-to-site variability with peak ratios around 2 and values below unity at selected sites. In contrast, the distribution of R_{PSA} obtained from the combination of simulations and empirical factors is markedly uniform, with values steadily above unity across all the areas characterize by softer layers. To interpret this pattern, it should be noted that the source and path terms are cancelled out when computing the transfer function, leaving it function of the V_{S30} only. A comparison of the distribution of $R_{PSA,BSSA14}$ and $R_{PSA,BA18}$ in Figure **4.7**-B and C also shows that the predictions of PSA at T1 and T2 obtained with the BSSA14 and BA18 empirical factors are quite similar for the Pleasanton-Livermore Valley and the Southern region of the San Francisco Peninsula with values around 1.2 and 1.3, respectively. However, a pronounced difference is seen west of the Hayward Fault and in the Santa Clara Valley, with ratios of 1.5 and 2 for BSSA14 and BA18, respectively.

Figure **4.8** and Figure **4.9** show the regional-scale maps of the PGV and PGV ratios (R_{PGV}), respectively, for the fault normal component of the ground motions. The PGV maps for the fault parallel component are provided in the supplemental material (Figure 4.20). The symbols have the same meaning explained above for the R_{PSA} maps. The distribution of R_{PGV} follows a pattern similar to R_{PSA}, with a pronounced scattering observed for $R_{PGV,Sim}$, reflecting a site-to-site variability that the purely simulation-based approach can capture through path and site effects. Processing the ground motions with the empirical factors is seen to smoothen such an effect leading to uniform distributions of the ratio across the domain (plots B and C).

To better interpret such differences, two sites are selected to inspect the observed motions and spectral amplitudes as a function of the site conditions, potential rupture directivity, wave-path, and three-dimensional focusing and defocusing effects.

The first site is in the Santa Clara Valley (black square by 'SC' in Figure **4.7**) and is characterized by Z1.0 = 0.6-km and Rrup = 19.9-km. For the fault normal component, $R_{PSA,Sim}$ = 0.9 and 1.5 at T1 and T2, respectively, $R_{PSA,BSSA14}$ = 1.5 at T1 and T2, and $R_{PSA,BA18}$ = 1.9 at T1 and T2. Figure **4.10**-A and C show the PSA for the two separate components. The comparison between the spectra obtained with the simulation-based approach with $V_{s,min}$ = 500 and 250-/sec (red and green lines) demonstrates no substantial modification of the spectral amplitude and shape at periods longer than ~3-sec, and amplifications by a factor of 1.5-2 at periods shorter than ~3-sec. The BSSA14 (black) and BA18 (blue) empirical models, instead, yield a consistent amplification across the full spectral period bandwidth (0.3 to 10-sec), with peak values of the spectral ratios around 1.5 for BSSA14 and 2 for BA18, between 1-sec and 2-sec. At periods shorter than about 1-sec, the empirical models incorporate the competing effect of decreased shear-wave velocity and increased damping caused by potential nonlinearities occurring in soft soil under strong shaking, which are known to cause a deamplification of the ground motions at short periods. The simulated ground motions, instead, do not model soil nonlinearities, leading to expected overestimates of the spectral amplitudes at shorter periods. To better assess the differences introduced by the assumptions behind the different modeling approaches, Figure **4.10**-C shows the transfer functions derived across all methods for the RotD50 of the motions. The solid lines (black for BSSA14 and blue for BA18) represent the functions derived from the empirical models incorporating both linear and nonlinear effects (L+NL), while the dotted lines denote the functions incorporating the linear effects only (L). The red line, instead, represents the transfer function obtained from the simulations. The observed trend confirms the effect of nonlinearities at periods shorter than about 2-sec for BSSA14 and 1-sec for BA18, pointing to a large discrepancy (factor of about 1.2) between the spectral amplitudes between 0.3 and 0.5-sec when considering the linear effects only. Finally, Figure **4.10**-D shows the velocity time histories for the two separate components of the ground motion as obtained from the different modeling approaches, demonstrating differences up to 45% in the prediction of the PGV, with effects on the structural response that will be discussed in the next section.

An additional aspect to consider when comparing the ground-motion spectra and time histories across the different modeling approaches relates to the way the acceleration components are treated. The ground motions obtained from the physics-based simulations implicitly account for any modification due to the site conditions, wave path, and source effects for the fault normal and the fault parallel motions. On the contrary, the empirical factors are derived for the median horizontal intensity (RotD50), and then applied to both components to obtain the modified motions. As a result, the simulated motions inherently incorporate all the features of the ground-motion components obtained for different $V_{s,min}$, reflecting the effect of the incidence of the 3D seismic waves in generating different motions in the two directions. Whereas the motions processed with the empirical factors only carry the information on the set of site-specific variables utilized in as an input for the empirical model without reflecting any component-specific feature. This includes, for example, the PGA of the RotD50 that is calculated at the reference rock based on the site-specific parameters. Simple techniques to utilize the component-specific PGA to obtain the component-specific empirical factors can be implemented. Yet, this is still expected to yield estimates different from those obtained from simulation-based approaches.

The second site considered in this study is in the Pleasanton-Livermore Valley (black square by ‘PL’ in Figure **4.7**), with Z1.0 = 1.46-km, Rrup = 21-km. For the fault normal component, $R_{PSA,Sim}$ = 1.1 at T1 and T2, $R_{PSA,BSSA14}$ = 1.2 at T1 and T2, and $R_{PSA,BA18}$ = 1.2 at T1 and T2.

Figure **4.11** shows the same set of plots analyzed in Figure **4.10**, demonstrating a substantial agreement among the predictions obtained from the considered modeling approaches, particularly when comparing the models incorporating the linear effects only. Such consistency is attributed to the combined effect of the limited changes in the Vs30 introduced by the $V_{s,min}$ when $V_{S30,T}$ is 401-m/sec and the Z1.0 of 1.46-km, the latter making the site conditions at PL closer to the sites characterizing most ground-motion data utilized to obtain the empirical factors (e.g., basins typical of Southern California, Wald & Graves, 1998).

The analyses carried out for SC and PL were extended to all the stations across the computational domain. Figure **4.12** shows the transfer functions for all the sites with $V_{S30} < 500\ m/sec$ obtained with the BSSA14 model in black, the BA18 model in blue, and the simulations in red. The transfers functions for the empirical models incorporate both the linear and nonlinear terms. The thin lines represent each individual site, while the thick lines the median across all sites. The comparison of the medians confirms the observations made for SC and PL, demonstrating that the purely simulation-based approach does not yield (in the average) substantial amplifications at periods longer than ~4-sec, and generally smaller amplifications than those obtained with the empirical factors at periods longer than ~1 sec.

Figure **4.13** shows the V_s profiles of arrays of stations sampled on a 10-km grid along the strike (10 to 110-km) at increasing distances from the fault (from ~0-km to ~10-km) obtained from the USGS seismic velocity model (Aagaard & Hirakawa, 2021), indicating that the majority of the sites east of the fault are characterized by basins that are relatively shallow compared to other regions, with strong impedance contrasts. At these sites, the quarter-wavelength approximation for standing body waves (Boore & Joyner, 1997) results in resonance frequencies of approximately 0.3 to 1-Hz in the average. Such considerations are limited to the assumption of 1D wave propagation, which cannot capture the complexity of phenomena taking place in real geological structures (Baise et al., 2003). However, they provide a basis for the interpretation of the simulation results and can be used to inform the development of site-specific tapering functions for empirical amplification factors, by deriving the motion amplification ratios when the shallow layers in the Vs profile are modified. An additional element to consider when comparing the transfer functions in Figure **4.12** is the paucity of data used to constrain the empirical models for large magnitude events, recorded at short distance and with geological characteristics typical of the San Francisco Bay Area.

4.6 Structural Response at The Regional Scale

The ten-story building presented in the section ‘Building Model’ is utilized to assess the impact of the different approaches for modeling the soft shallow layers on the response of a realistic structure. The three-dimensional building is subject to bidirectional excitation, with the fault parallel component of the motion applied along the X-direction of the building plan, and the fault normal along the Y-direction (see Figure **4.5**).

Figure **4.14**-A though D show the distribution of the PIDR across the computational domain as obtained from the simulation model characterized by (A) $V_{s,min}$ = 500-m/sec, (B) $V_{s,min}$ = 250-m/sec, (C) $V_{s,min}$ = 500-m/sec processed with BSSA14, (D) $V_{s,min}$ = 500-m/sec processed with BA18.

The structural response ranges from slight damage (0.3%) up to complete damage (4%) (FEMA, 2022) across all modeling approaches , with the highest demands observed in the near field, west of the Hayward fault, when the soft layers of the geological structure are modeled. The building is seen to approach complete damage for an increasingly larger number of sites when the simulated ground motions are processed with the empirical factors in BSSA14 (map C) and BA18 (map D). A pattern in the increase of the demand in the forward directivity direction is captured in the simulation-based approach ($V_{s,min}$ of 250-m/sec) and partially preserved when the motions are processed with the BSSA14 empirical factors.

Two sites are selected to analyze the differences in the structural demands across the adopted modeling methods, one by Hayward, CA (black square by ‘HW’ in Figure **4.14**) and one in the Santa Clara Valley (black square by ‘SC’ in Figure **4.14**). The comparison of the structural response at the HW site in Figure **4.14**-E shows that employing a $V_{s,min}$ of 250-m/sec instead of 500-m/sec leads to differences in the building peak response by a factor of 1.15 in the X-direction (fault normal) and 1.26 in the Y-direction (fault parallel), pointing to a significant change in the structural behavior in response to relatively limited modifications to the velocity profile. Differences in the estimates of the building response become significant when extending the comparison to the motions processed with the empirical factors, with peak differences attaining factors as large as 1.65 between the response obtained from the simulation with $V_{s,min}$ = 250-/sec and the simulations processed with BA18. These differences in the prediction lead to an estimate of damage from moderate/extensive to complete (FEMA, 2022). At site SC, instead, the building is seen to remain linear across all modeling approaches, with differences that attain a peak factor of 1.43 between the model adopting $V_{s,min}$= 250-m/sec and BA18, and a notable agreement between the predictions of the simulation with $V_{s,min}$ = 250-/sec and BSSA14.

Figure **4.15** shows the distribution of the PIDR along the building height obtained from all modeling approaches investigated in this study for the sites with $V_{S30} < 500\ m/sec$. The maximum median response is seen to vary by a factor of about 1.25 when the simulations employ a $V_{s,min}$ of 500-m/sec as opposed to 250-m/sec; and by a factor of 1.1 and 1.2 when the motions with $V_{s,min}$= 500-m/sec are processed with the BSSA14 and the BA18 models, respectively. The localization of the maximum demand does not vary (in the average) across the modeling methods. However, a station-by-station comparison of the type shown in Figure **4.14**-E demonstrates a high variability in the localization of the maximum demand along the building height, pointing to significant differences in the structural assessment outcomes.

To evaluate the differences in the structural response across the full computational domain on a site-by-site basis, Figure **4.16** shows the maps of the ratio of the PIDR obtained with the different modeling approaches. Similarly to the notation adopted for the PSA and the PGV, $R_{PIDR,Sim}$ = $PIDR_{Sim250}/PIDR_{Sim500}$, $R_{PIDR,BSSA14}$ = $PIDR_{BSSA14}/PIDR_{Sim500}$, and $R_{PIDR,BA18}$ = $PIDR_{BA18}/PIDR_{Sim500}$. Generally, higher response ratios are observed when the motions are processed with the empirical models, with $R_{PIDR,BA18}$ attaining values above 2 for the majority of the stations west of the fault. The spatial variability of the structural demand reflects the site-to-site variability of the analyzed IMs and remains pronounced for the purely simulation-based approach, where the structural response is seen to also change outside the areas in which the soft layers modeling is affected by the cap on the $V_{s,min}$. Remarkably, $R_{PIDR,Sim}$ is seen to vary from a minimum of 0.51 to a maximum of 3.76, pointing to substantial differences in the structural response assessments for small variations introduced in the velocity profiles.

4.7 Concluding Remarks and Future Work

This study evaluates the effect of two approaches for modeling soft sediments on the seismic response of an archetypal three-dimensional building: one method is based on the utilization of high-resolution physics-based simulations that can resolve a minimum shear wave velocity of 250-m/sec; the other relies on the combined use of simulations resolving a minimum shear wave velocity of 500-m/sec and empirical factors to achieve the same target time-averaged shear wave velocity in the upper 30-m (i.e., Vs30 obtained with $V_{s,min}$ = 250-m/sec).

The primary objective is to assess the effectiveness of methods that combine physics-based simulations with empirical models in providing ground motions that can be reliably utilized by engineers in seismic analyses and offer insights into the reasons behind potential misestimates introduced by the use of such factors. This is motivated by the possible unavailability of a sufficient number of simulated ground motions resolving low shear-wave velocities for a specific region or site of interest to perform structural performance evaluations.

To this aim, two empirical models were employed, namely the NGA-W2 equations for PGA, PGV, and PSA by Boore et al. (2014), and the empirical model for FAS by Bayless & Abrahamson (2018). The region and earthquake selected for this work are the San Francisco Bay Area and an M7 strike-slip shallow crustal earthquake on the Hayward fault. A three-dimensional RC moment-resisting frame building is utilized as a typical mid-rise structure in the San Francisco Bay Area. Differences in the ground motions generated with the two methods are assessed across the computational domain with respect to the IMs most relevant to the response of the considered structure, that is, the PSA at the fundamental periods of the building and the PGV. Structural responses are evaluated in terms of PIDR and global torsion.

Results show fundamental differences in the prediction of the ground-motion IMs and building responses at the sites with a Vs30 directly affected by the computational cap on the $V_{s,min}$ and, noteworthy, at the sites in their vicinity. The analyses performed across the region with tapering techniques discussed in the literature (de la Torre et al., 2020; R. W. Graves & Pitarka, 2010; Lee et al., 2022) demonstrated that the largest differences in the average spectral predictions are seen at spectral periods longer than approximately 1 second. This evidence highlights the criticality of deriving appropriate tapering functions, specific to the amplification expected in the geological structures of the region under consideration if methods that combine physics-based simulations and empirical models are employed. At the sites not directly affected by the cap on the $V_{s,min}$ and located in the vicinity of soft sites, differences arise from wave-propagation phenomena across soft and stiff layers that can be fully captured only by the simulation-based approach in which low shear-wave velocity are modeled ($V_{s,min}$= 250-m/sec in this study). Site-specificity of ground-motion amplitudes is partially preserved when simulated motions are corrected with empirical factors.

When utilizing pure simulation-based approaches where the $V_{s,min}$ is made to vary from 250 to 500-m/sec, differences in the building PIDR attain ratios of 0.51 (min) and 3.76 (max), pointing to the significant impact of even small variations in the velocity profile on the response of structures of the type considered in this study (mid-rise structure with fundamental periods between 1 and 2 sec). Average PIDRs are seen to vary by a factor of 1.1 and 1.2 when comparing the pure simulation-based approach and methods coupling simulations and the BSSA14 and BA18 empirical factors, respectively. However, such differences become significantly larger when conducting a site-by-site comparison, leading to response assessments from moderate to complete damage. Predictions of global torsion were also found to be different across the considered modeling approaches, but without attaining values critical for structural safety assessments.

Findings from this study are related to the specific features of the USGS seismic velocity model utilized in the ground-motion simulations, the employed (ergodic) empirical models, and the employed structural model. However, the outcomes remain relevant for a correct interpretation of the differences introduced in the structural response assessments by physics-based simulation models that do not resolve low shear wave velocities and methods that integrate simulations and empirical factors.

Moving forward, it would be useful to expand studies of this type to include comparisons against non-ergodic GMMs specific to the region under consideration and the utilization of models that resolve shear-wave velocities larger than 500-sec. This should be done especially for region lacking representation in historical record catalogs, making the empirical factors not well constrained for specific sought conditions (large magnitude events, short distance, fort layers of sediments).

Acknowledgements

The development of the simulated ground motions utilized in this study was supported by the U.S. Department of Energy Office of Cyber Security, Energy Security and Emergency Response at Lawrence Berkeley National Laboratory. The authors thank Dr. Robert Graves and Dr. Arben Pitarka for their valuable comments and suggestions and for helping with the ground-motion processing.

References

Aagaard, B. T., Brocher, T. M., Dolenc, D., Dreger, D., Graves, R. W., Harmsen, S., Hartzell, S., Larsen, S., & Zoback, M. Lou. (2008). Ground-motion modeling of the 1906 San Francisco earthquake, part I: Validation using the 1989 Loma Prieta earthquake. *Bulletin of the Seismological Society of America*, *98*(2), 989–1011. https://doi.org/10.1785/0120060409

Aagaard, B. T., & Hirakawa, E. T. (2021). *San Francisco Bay region 3D seismic velocity model v21.1*. Earthquake Hazards Program, USGS.

ACI (American Concrete Institute). (2019). 318-19 Building Code Requirements for Structural Concrete and Commentary. In *318-19 Building Code Requirements for Structural Concrete and Commentary*. https://doi.org/10.14359/51716937

Ancheta, T. D., Darragh, R. B., Stewart, J. P., Seyhan, E., Silva, W. J., Chiou, B. S. J., Wooddell, K. E., Graves, R. W., Kottke, A. R., Boore, D. M., Kishida, T., & Donahue, J. L. (2014). NGA-West2 Database. *Https://Doi.Org/10.1193/070913EQS197M*, *30*(3), 989–1005. https://doi.org/10.1193/070913EQS197M

ASCE-7. (2016). *Minimum Design Loads and Associated Criteria for Buildings and Other Structures*.

ASCE/SEI7. (2022). *Minimum Design Loads and Associated Criteria for Buildings and Other Structures*. American Society of Civil Engineers.

Baise, L. G., Dreger, D. S., & Glaser, S. D. (2003). The Effect of Shallow San Francisco Bay Sediments on Waveforms Recorded during the M W 4.6 Bolinas, California, Earthquake. In *Bulletin of the Seismological Society of America* (Vol. 93, Issue 1). http://pubs.geoscienceworld.org/ssa/bssa/article-pdf/93/1/465/2715548/465_ssa01213.pdf?casa_token=0BoDNMbhltIAAAAA:3VYc9PZPsgh5KZU_3RlOmmCOG-mR7xvaffT1qoSO8FPyl_5SX3wZFKWliDYtAP0b

Bao, H., Bielak, J., Ghattas, O., Kallivokas, L. F., O'Hallaron, D. R., Shewchuk, J. R., & Xu, J. (1996). *Earthquake Ground Motion Modeling on Parallel Computers*. https://doi.org/https://doi.org/10.1145/369028.369053

Bayless, J., & Abrahamson, N. (2018). *An Empirical Model for Fourier Amplitude Spectra using the NGA-West2 Database*.

Bonilla, L. F., Archuleta, R. J., & Lavallée, D. (2005). Hysteretic and dilatant behavior of cohesionless soils and their effects on nonlinear site response: Field data observations and modeling. *Bulletin of the Seismological Society of America*, *95*(6), 2373–2395. https://doi.org/10.1785/0120040128

Boore, D. M., & Joyner, W. B. (1997). Site Amplifications for Generic Rock Sites. In *Bulletin of the Seismological Society of America* (Vol. 87, Issue 2).

Boore, D. M., Stewart, J. P., Seyhan, E., & Atkinson, G. M. (2014). NGA-West2 equations for predicting PGA, PGV, and 5% damped PSA for shallow crustal earthquakes. *Earthquake Spectra*, *30*(3), 1057–1085. https://doi.org/10.1193/070113EQS184M

Campillo, B. M., Gariel, C., nzI, K., & Sanchez-sesma, F. J. (1989). DESTRUCTIVE STRONG GROUND MOTION IN MEXICO CITY: SOURCE, PATH, AND SITE EFFECTS DURING GREAT 1985 MICHOACAN EARTHQUAKE. In *Bulletin of the Seismological Society of America* (Vol. 79, Issue 6). http://pubs.geoscienceworld.org/ssa/bssa/article-pdf/79/6/1718/5334806/BSSA0790061718.pdf?casa_token=1mZJwYqT-z8AAAAA:zi0NGU4tNL_UI10UCwfIkLrZjuA

de la Torre, C. A., Bradley, B. A., & Lee, R. L. (2020). Modeling nonlinear site effects in physics-based ground motion simulations of the 2010–2011 Canterbury earthquake sequence. *Earthquake Spectra*, *36*(2), 856–879. https://doi.org/10.1177/8755293019891729

FEMA. (2012). *Hazus ®-MH 2.1 Technical Manual*. www.msc.fema.gov

FEMA. (2022). *Hazus Earthquake Model Technical Manual*.

Graves, R., & Pitarka, A. (2016). Kinematic ground-motion simulations on rough faults including effects of 3D stochastic velocity perturbations. *Bulletin of the Seismological Society of America*, *106*(5), 2136–2153. https://doi.org/10.1785/0120160088

Graves, R. W., & Pitarka, A. (2010). Broadband ground-motion simulation using a hybrid approach. *Bulletin of the Seismological Society of America*, *100*(5 A), 2095–2123. https://doi.org/10.1785/0120100057

Hanks, T. C., & Krawinkler, H. (1991). THE 1989 LOMA PRIETA EARTHQUAKE AND ITS EFFECTS: INTRODUCTION TO THE SPECIAL ISSUE. *Bulletin of the Seismological Society of America*, *81*(5), 1415–1423. http://pubs.geoscienceworld.org/ssa/bssa/article-pdf/81/5/1415/5340514/bssa0810051415.pdf?casa_token=LY1k3Mc-wZAAAAAA:-MdGIj70CNRhSKAIB3wObvBQT

Hashash, Y. M. A., Harmon, J., Ilhan, O., Stewart, J. P., Rathje, E. M., Campbell, K. W., Silva, W. J., & Goulet, C. A. (2018). Modelling of Site Amplification via Large Scale Nonlinear Simulations with Applications to North America. In *Geotechnical Earthquake Engineering and Soil Dynamics V* (pp. 523–537). https://doi.org/10.1061/9780784481462.051

Kramer, S. L. (1996). *Geotechnical Earthquake Engineering* (1st ed.). Pearson.

Lee, R. L., Bradley, B. A., Stafford, P. J., Graves, R. W., & Rodriguez-Marek, A. (2022). Hybrid broadband ground-motion simulation validation of small magnitude active shallow crustal earthquakes in New Zealand. *Earthquake Spectra*, *38*(4), 2548–2579. https://doi.org/10.1177/87552930221109297

Maechling, P. J., Silva, F., Callaghan, S., & Jordan, T. H. (2015). SCEC broadband platform: System architecture and software implementation. *Seismological Research Letters*, *86*(1), 27–38. https://doi.org/10.1785/0220140125

Mander, J. B., Priestley, M. J. N., & Park, R. (1988). Theoretical Stress-Strain Model for Confined Concrete. *Journal of Structural Engineering*, *114*(8), 1804–1826. https://doi.org/10.1061/(ASCE)0733-9445(1988)114:8(1804)

Matinrad, P., & Petrone, F. (2023). ASCE/SEI 7-compliant site-specific evaluation of the seismic demand posed to reinforced concrete buildings with real and simulated ground motions. *Earthquake Engineering and Structural Dynamics*, *52*(15), 4987–5009. https://doi.org/10.1002/eqe.3995

Maufroy, E., Cruz-Atienza, V. M., Cotton, F., & Gaffet, S. (2015). Frequency-scaled curvature as a proxy for topographic site-effect amplification and ground-motion variability. *Bulletin of the Seismological Society of America*, *105*(1), 354–367. https://doi.org/10.1785/0120140089

McCallen, D., Petersson, A., Rodgers, A., Pitarka, A., Miah, M., Petrone, F., Sjogreen, B., Abrahamson, N., & Tang, H. (2021). EQSIM—A multidisciplinary framework for fault-to-structure earthquake simulations on exascale computers part I: Computational models and workflow. *Earthquake Spectra*, *37*(2), 707–735. https://doi.org/10.1177/8755293020970982

Nakata, R., McCallen, D., Pitarka, A., Pinilla Ramos, C., & Tang, H. (2023). *Evaluation of broadband M7 Hayward fault physics-based simulations* (In Preparation).

Paolucci, R., Mazzieri, I., Smerzini, C., & Stupazzini, M. (2014). Physics-Based Earthquake Ground Shaking Scenarios in Large Urban Areas. In A. Ansal (Ed.), *Perspectives on European Earthquake Engineering and Seismology, Geotechnical,* *Geological and Earthquake Engineering* (Vol. 34, pp. 331–359). Springer Cham Heidelberg New York Dordrecht London. https://doi.org/DOI 10.1007/978-3-319-07118-3_10

Petrone, F., Abrahamson, N., McCallen, D., & Miah, M. (2020). Validation of (not-historical) large-event near-fault ground-motion simulations for use in civil engineering applications. *Earthquake Engineering and Structural Dynamics*. https://doi.org/10.1002/eqe.3366

Petrone, F., Abrahamson, N., McCallen, D., Pitarka, A., & Rodgers, A. (2021). Engineering evaluation of the EQSIM simulated ground-motion database: The San Francisco Bay Area region. *Earthquake Engineering and Structural Dynamics*, *April*, 1–23. https://doi.org/10.1002/eqe.3540

Petrone, F., Taslimi, A., Mohammadi Nia, M., David McCallen, & Arben Pitarka. (2024). *Ground Motions Site and Event Specificity: Insights from Assessing a Suite of Simulated Ground Motions in The San Francisco Bay Area* (Earthquake Spectra. Submitted).

Pitarka, A., Akinci, A., De Gori, P., & Buttinelli, M. (2022). Deterministic 3D Ground-Motion Simulations (0–5 Hz) and Surface Topography Effects of the 30 October 2016 Mw 6.5 Norcia, Italy, Earthquake. *Bulletin of the Seismological Society of America*, *112*(1), 262–286. https://doi.org/10.1785/0120210133

Pitarka, A., Graves, R., Irikura, K., Miyakoshi, K., & Rodgers, A. (2019). Kinematic Rupture Modeling of Ground Motion from the M7 Kumamoto, Japan Earthquake. *Pure and Applied Geophysics*. https://doi.org/10.1007/s00024-019-02220-5

Rodgers, A. J., Pitarka, A., Pankajakshan, R., Sjögreen, B., & Petersson, N. A. (2020). Regional-Scale 3D Ground-Motion Simulations of Mw 7 Earthquakes on the Hayward Fault, Northern California Resolving Frequencies 0–10 Hz and Including Site-Response Corrections. *Bulletin of the Seismological Society of America*, *110*(6), 2862–2881. https://doi.org/10.1785/0120200147

Roten, D., Olsen, K. B., & Pechmann, J. C. (2012). 3D simulations of M 7 earthquakes on the Wasatch fault, Utah, Part II: Broadband (0-10 Hz) ground motions and nonlinear soil behavior. *Bulletin of the Seismological Society of America*, *102*(5), 2008–2030. https://doi.org/10.1785/0120110286

Sjögreen, B., & Petersson, N. A. (2012). A fourth order accurate finite difference scheme for the elastic wave equation in second order formulation. *Journal of Scientific Computing*, *52*(1), 17–48. https://doi.org/10.1007/s10915-011-9531-1

Taborda, R., López, J., Karaoglu, H., Urbanic, J., & Bielak, J. (2010). *Speeding Up Finite Element Wave Propagation for Large-Scale Earthquake Simulations*.

Wald, D. J., & Graves, R. W. (1998). The Seismic Response of the Los Angeles Basin, California. In *Bulletin of the Seismological Society of America* (Vol. 88, Issue 2). http://pubs.geoscienceworld.org/ssa/bssa/article-pdf/88/2/337/5761863/BSSA0880020337.pdf?casa_token=tD1wXKIGIWgAAAAA:3hE_KpMUQK651L77uVqmVZmxUdJsyIKz-fRi8vnSDxm_g1PVKquNTmF_Ynt3T

Zhu, M., McKenna, F., & Scott, M. H. (2018). OpenSeesPy: Python library for the OpenSees finite element framework. *SoftwareX*, *7*, 6–11. https://doi.org/https://doi.org/10.1016/j.softx.2017.10.009

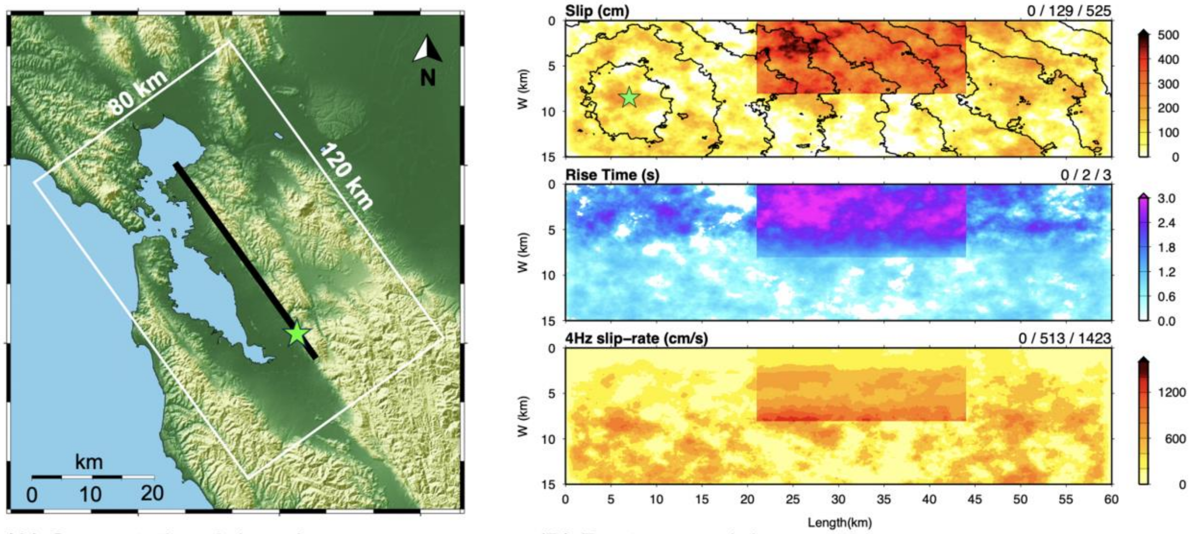

(A) Computational domain (B) Rupture model

Figure 4.1. (A) 80-km x 120-km computational domain covering the San Francisco Bay Area: the black line represents the projection of the Hayward Fault; the green star indicates the location of the epicenter. (B) Rupture model: slip distribution in cm with the hypocenter indicated by the green star (top row); rise time in sec (middle row); 4-Hz slip rate in cm/sec (bottom row) across the 15-km x 60-km rupture plane.

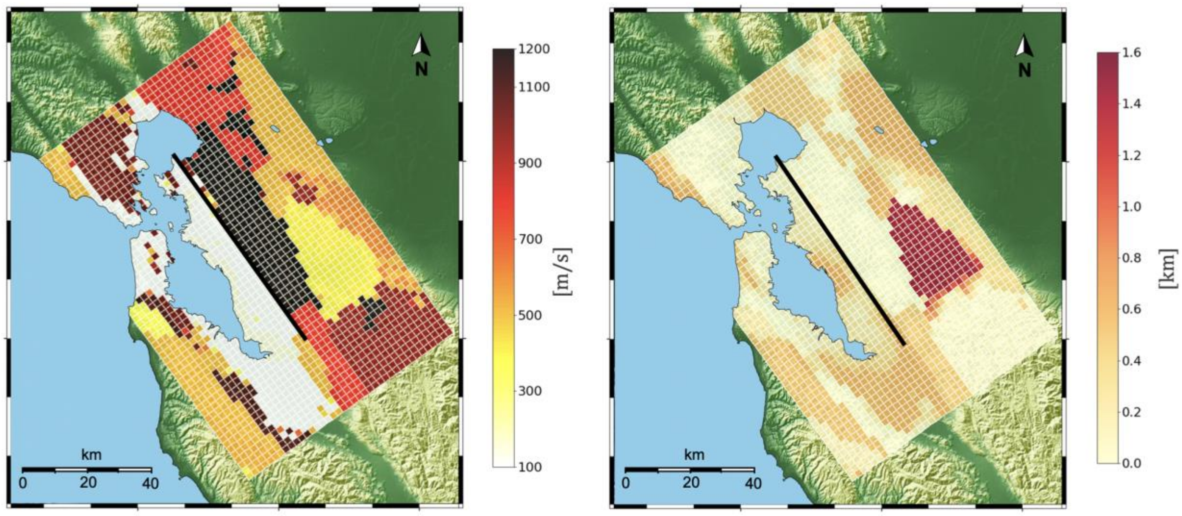

(A) Vs30 (USGS model)

(B) Z1.0 (USGS model)

Figure 4.2. Maps of the (A) Time-averaged shear wave velocity in the upper 30-m (Vs30) across the computational domain in m/sec; and (B) Depth to the 1.0-km/sec shear wave velocity (Z1.0) in km across the computational domain. Both parameters follow the USGS model (v.21.1, Aagaard & Hirakawa, 2021). The black line indicates the projection of the segment of the Hayward Fault considered in this study.

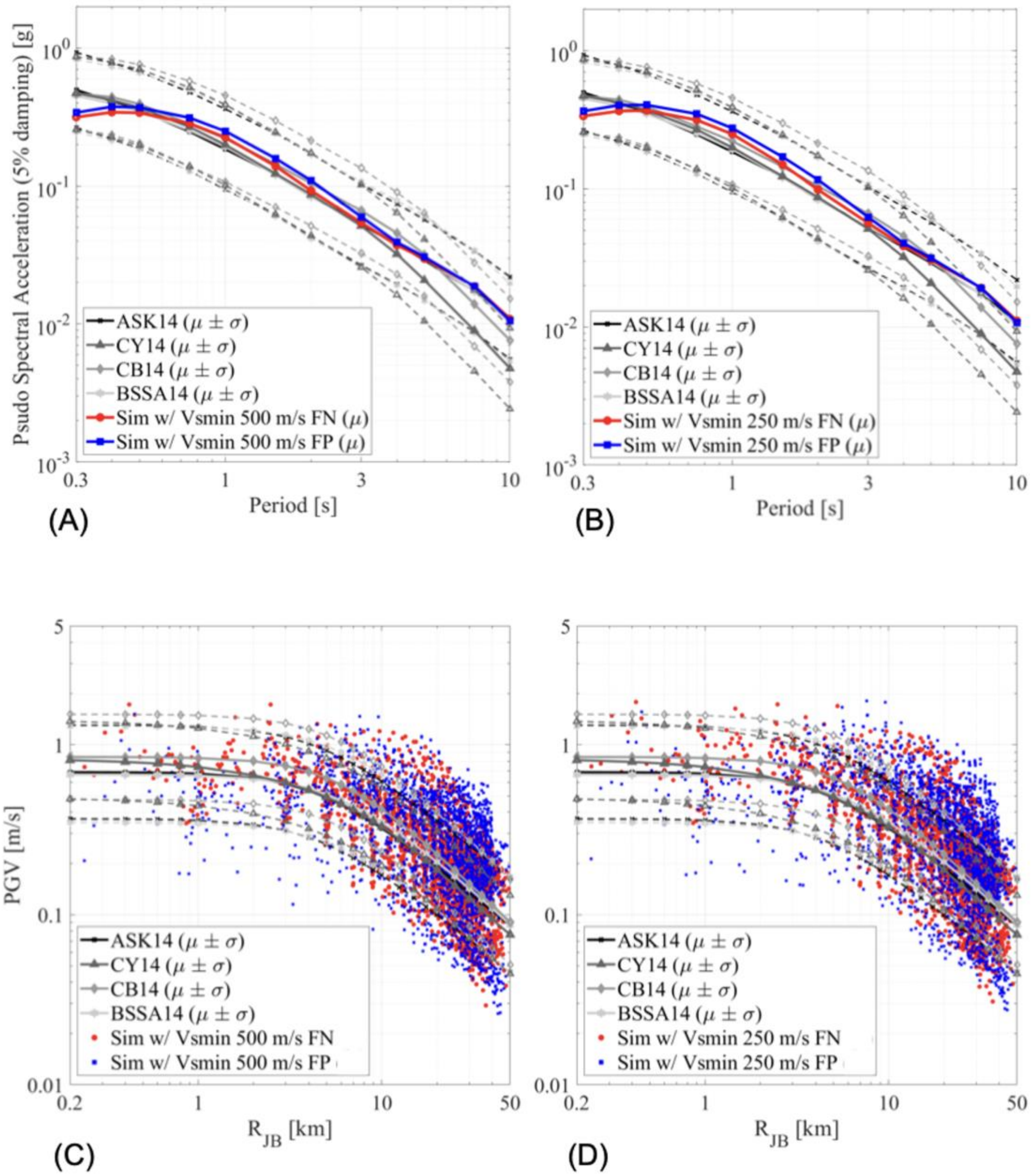

Figure 4.3. Comparison of simulated ground motions and the NGA-W2 ground-motion models for selected IMs. (A and B) PSA vs spectral periods; and (C and D) PGV vs distance, for the two separate components, FN and FP.

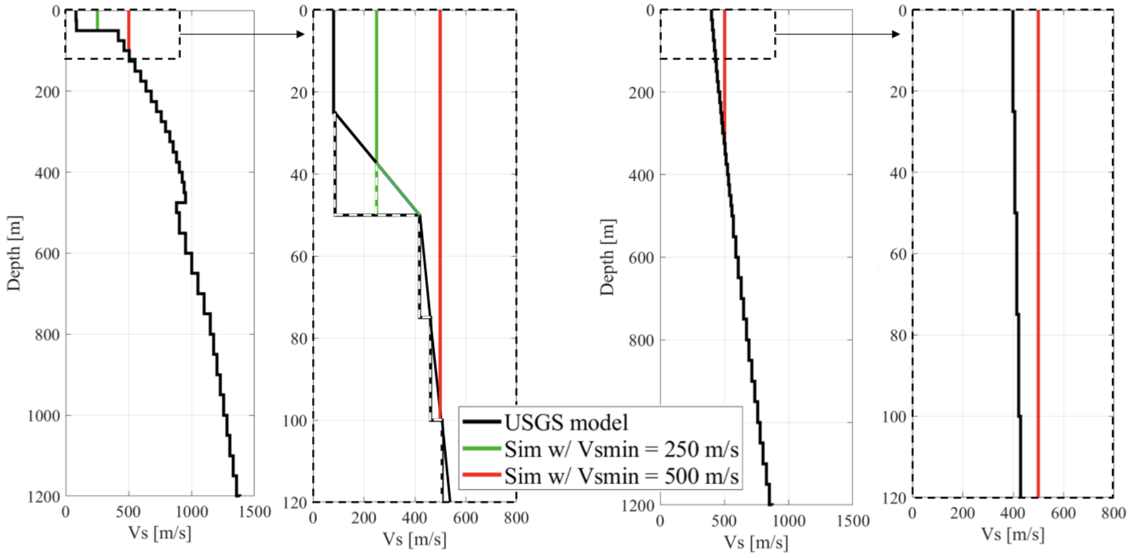

(A) Santa Clara Valley site

(B) Pleasanton-Livermore Valley site

Figure 4.4. Velocity profiles obtained from the USGS velocity model (black), the USGS velocity model with a $V_{s,min}$ of 250-m/sec (green) and a 500-m/sec (red) for two sites in the computational domain. (A) Santa Clara Valley; and (B) Pleasanton-Livermore Valley. The dotted lines represent the actual velocity profile, and the solid lines the velocity profile modeled in SW4.

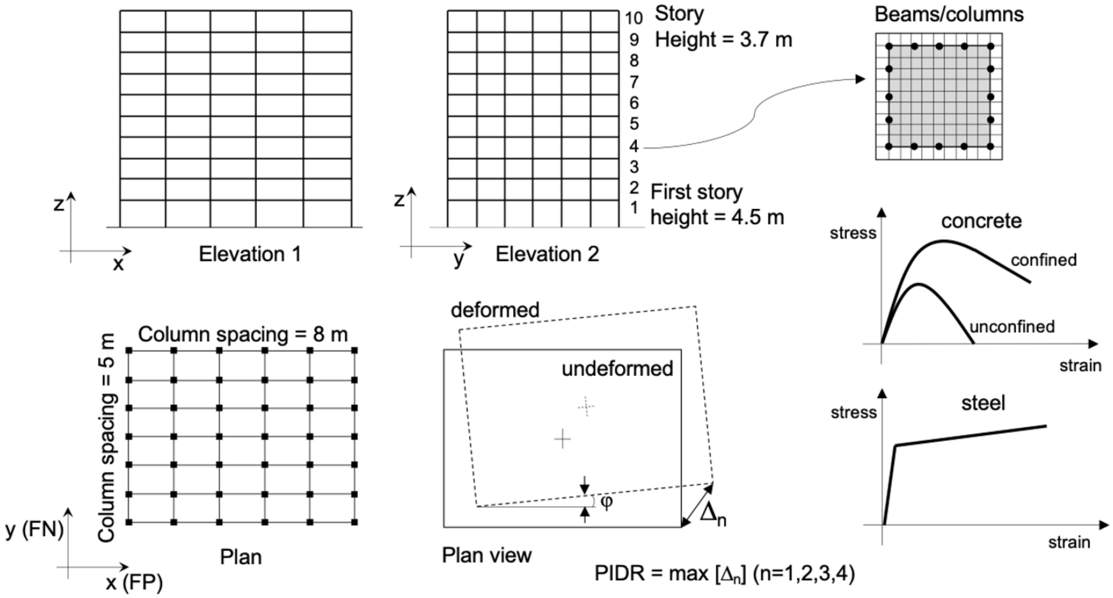

Figure 4.5. Three-dimensional reinforced concrete 10-story building model. (A) Elevation view along the two principal directions, X and Y; (B) Plan view with a schematic of the building deformed shape; (C) Detail of the fiber section model adopted (beams and columns) and materials constitutive laws (steel and concrete).

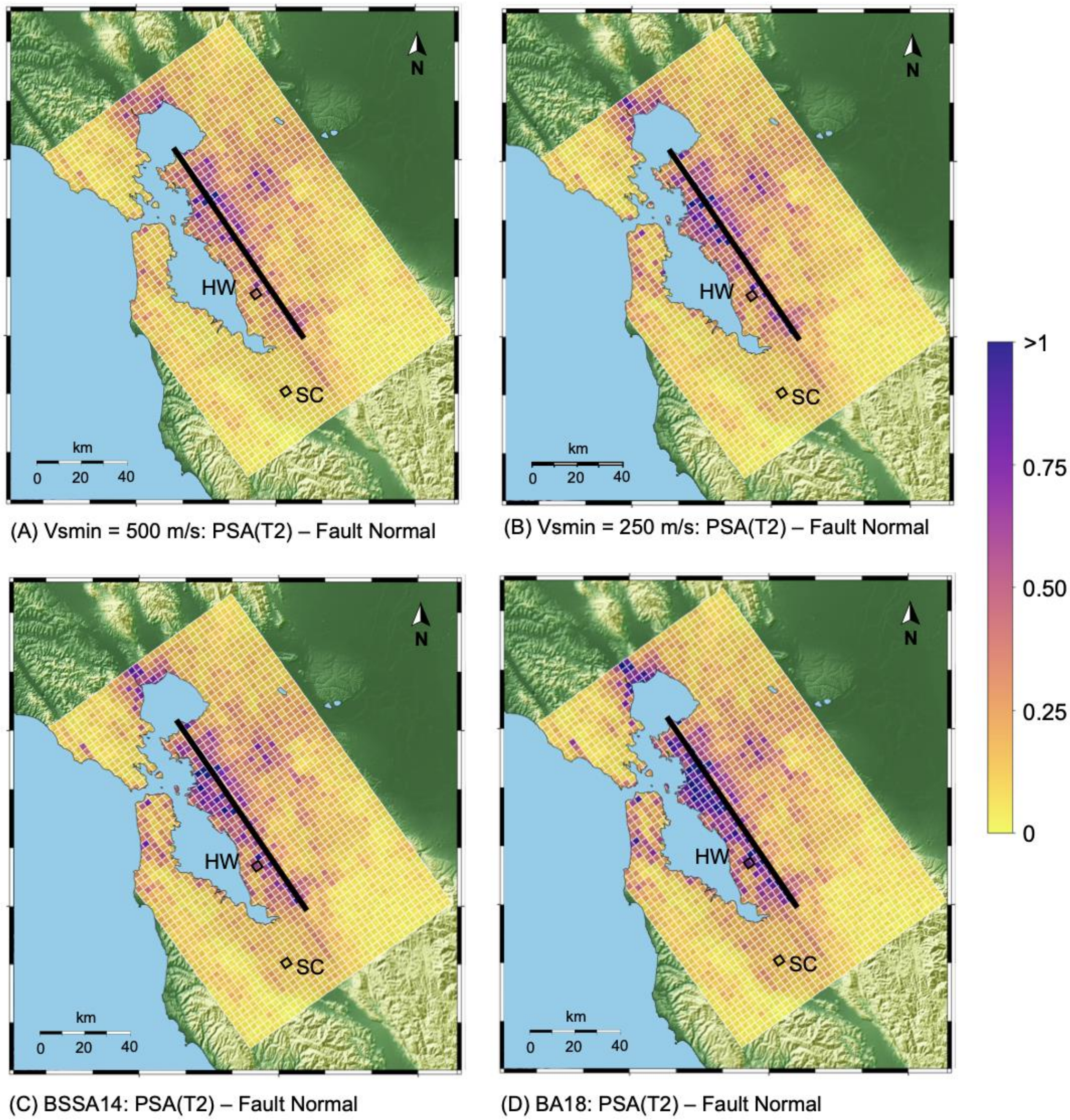

Figure 4.6. Pseudo-Spectral Acceleration at T2 - PSA(T2). Maps for the fault normal component of the ground motions: simulation model with (A) $V_{s,min}$ = 500-m/sec and (B) $V_{s,min}$ = 250-m/sec; simulation model with $V_{s,min}$ = 500-m/sec processed with (C) BSSA14 and (D) BA18 to obtain the same V_{S30} calculated with $V_{s,min}$ = 250-m/sec.

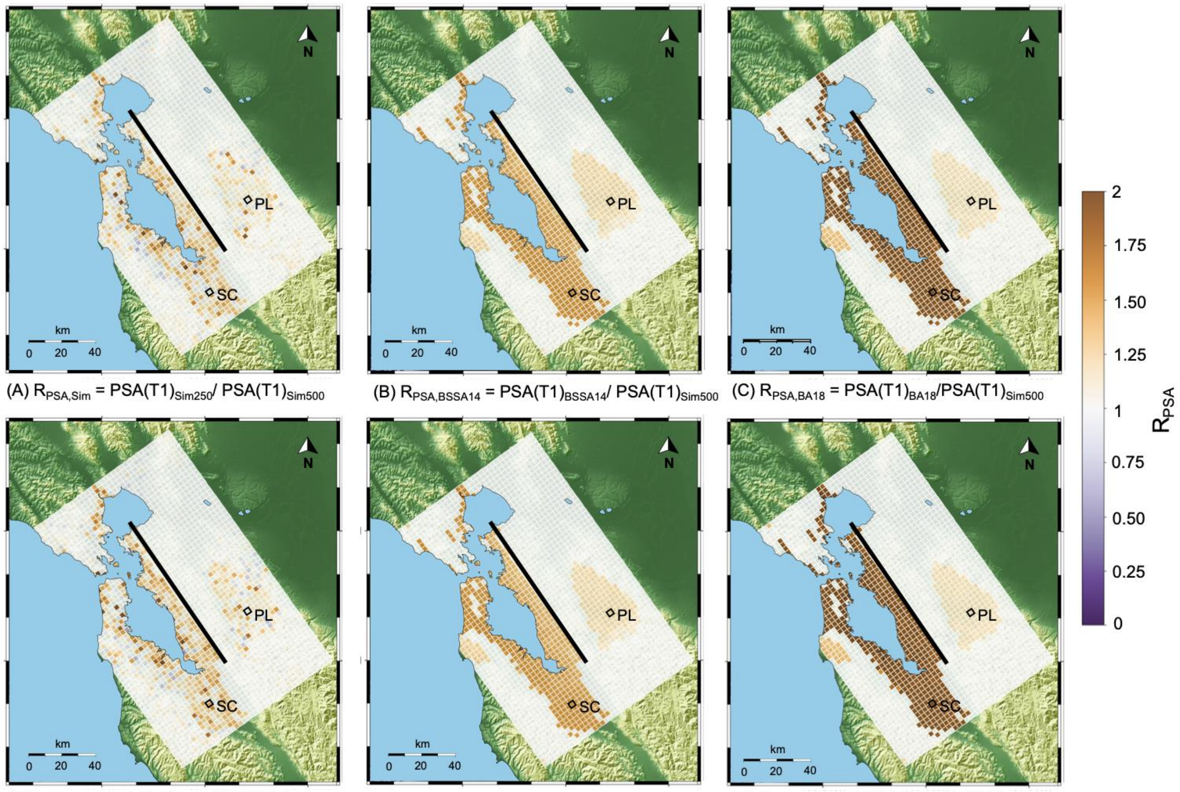

(A) $R_{PSA,Sim}$ = $PSA(T1)_{Sim250}$/ $PSA(T1)_{Sim500}$ (B) $R_{PSA,BSSA14}$ = $PSA(T1)_{BSSA14}$/ $PSA(T1)_{Sim500}$ (C) $R_{PSA,BA18}$ = $PSA(T1)_{BA18}$/$PSA(T1)_{Sim500}$

(D) $R_{PSA,Sim}$ = $PSA(T2)_{Sim250}$/ $PSA(T2)_{Sim500}$ (E) $R_{PSA,BSSA14}$ = $PSA(T2)_{BSSA14}$/ $PSA(T2)_{Sim500}$ (F) $R_{PSA,BA18}$ = $PSA(T2)_{BA18}$/$PSA(T2)_{Sim500}$

Figure 4.7. Pseudo Spectral Acceleration ratios (R_{PSA}) of the fault normal component of the ground motions at the fundamental periods of vibration of the ten-story building (T1 = 1.7-sec and T2 = 1.5-sec): (A and D) PSA from the simulation model with $V_{s,min}$ = 250-m/sec to the PSA from the simulation model with $V_{s,min}$ = 500-m/sec; (B and E) PSA from the BSSA14 empirical model to the PSA from the simulation model with $V_{s,min}$ = 500-m/sec; and (C and F) PSA from the BA18 empirical model to the PSA from the simulation model with $V_{s,min}$ = 500-m/sec.

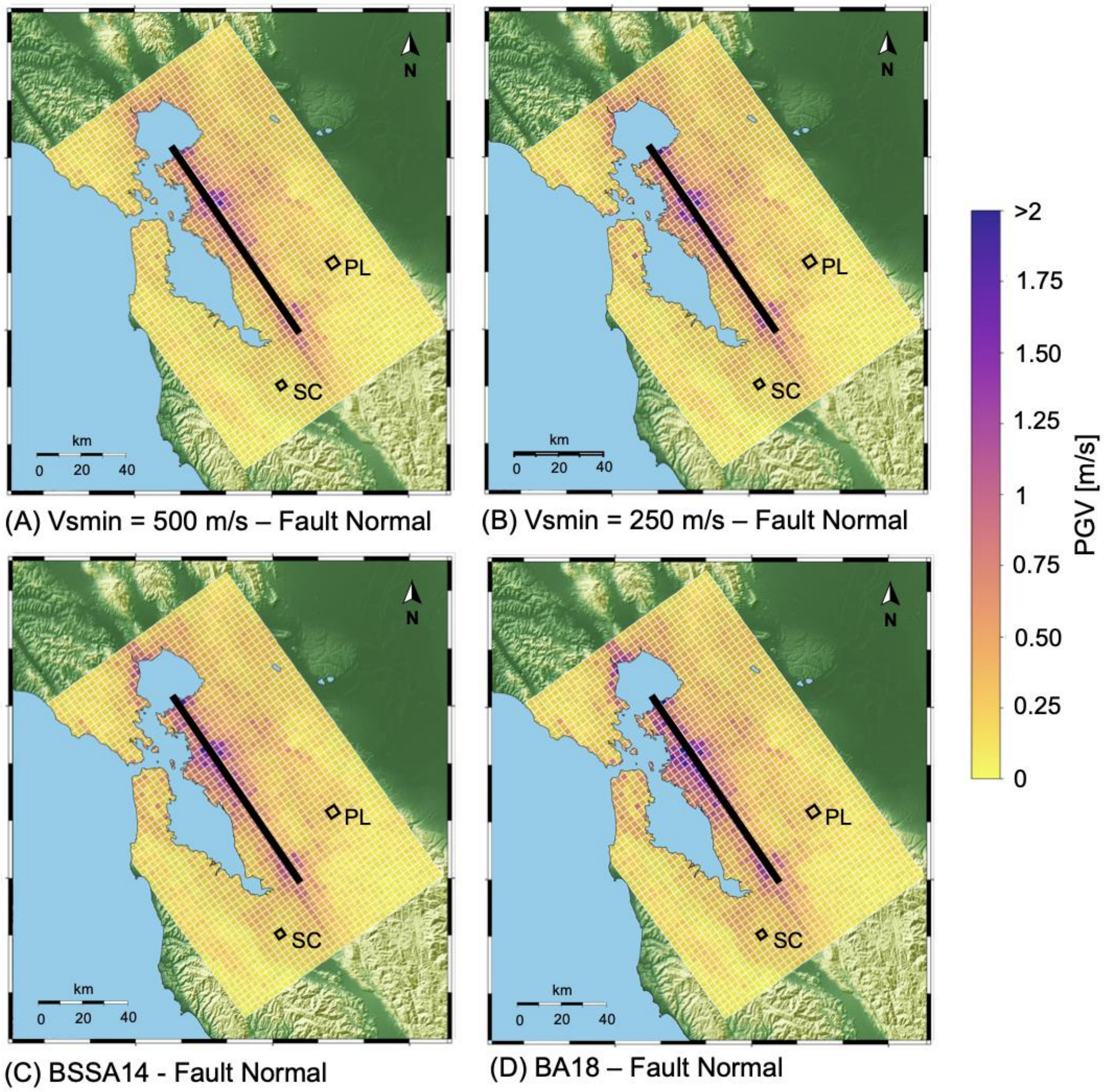

(A) Vsmin = 500 m/s – Fault Normal

(B) Vsmin = 250 m/s – Fault Normal

(C) BSSA14 - Fault Normal

(D) BA18 – Fault Normal

Figure 4.8. Peak Ground Velocity (PGV) maps for the fault normal component of the ground motions: (A) simulation model with $V_{s,min}$ = 500-m/sec; (B) simulation model with $V_{s,min}$ = 250-m/sec; (C) simulation model with $V_{s,min}$ = 500-m/sec processed with BSSA14; and (D) simulation model with $V_{s,min}$ = 500-m/sec processed with BA18.

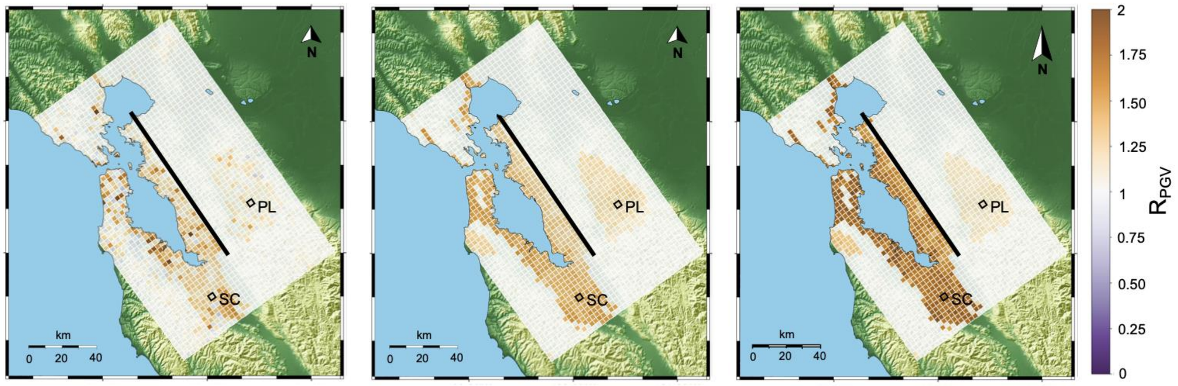

(A) $R_{PGV,Sim} = PGV_{Sim250}/ PGV_{Sim500}$ (B) $R_{PGV,BSSA14} = PGV_{BSSA14}/ PGV_{Sim500}$ (C) $R_{PGV,BA18} = PGV_{BA18}/PGV_{Sim500}$

Figure 4.9. Peak Ground Velocity ratios (R_{PGV}) for the fault normal component of the ground motions: (A) PGV from the simulation model with $V_{s,min}$ = 250-m/sec to the PSA from the simulation model with $V_{s,min}$ = 500-m/sec; (B) PGV from the BSSA14 empirical model to the PSA from the simulation model with $V_{s,min}$ = 500-m/sec; and (C) PGV from the BA18 empirical model to the PSA from the simulation model with $V_{s,min}$ = 500-m/sec.

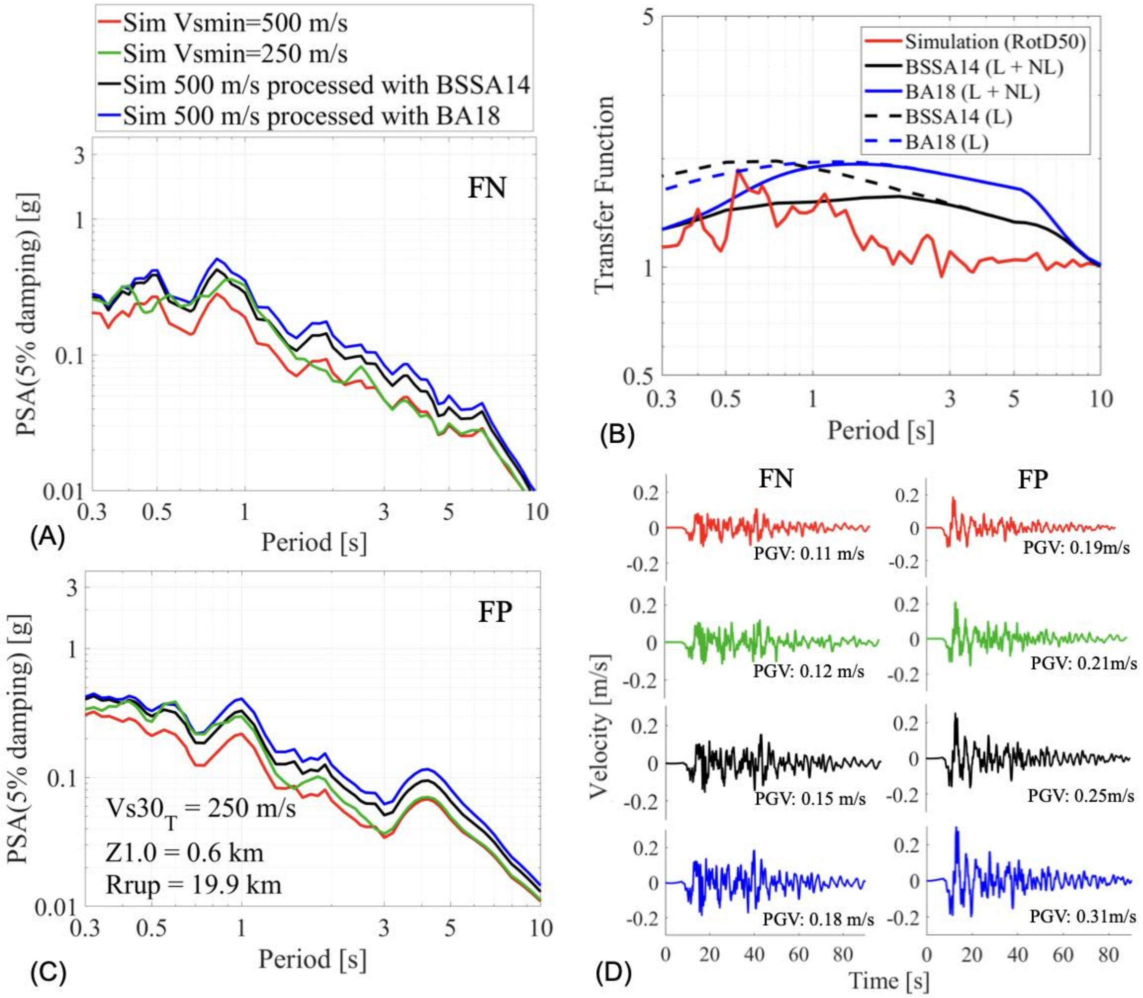

Figure 4.10. Site in the Santa Clara Valley (SC) characterized by Vs30$_T$ = 250-m/sec, Z1.0 = 0.6-km and Rrup = 19.9-km. (A and C) PSA of the fault normal and fault parallel components; (B) empirical models' transfer functions accounting for both linear and nonlinear effects (blue and black solid lines) and linear effects only (blue and black dotted lines) and simulation models' transfer function (red solid line); (D) velocity time-histories of the fault normal and fault parallel components obtained from the different modeling approaches.

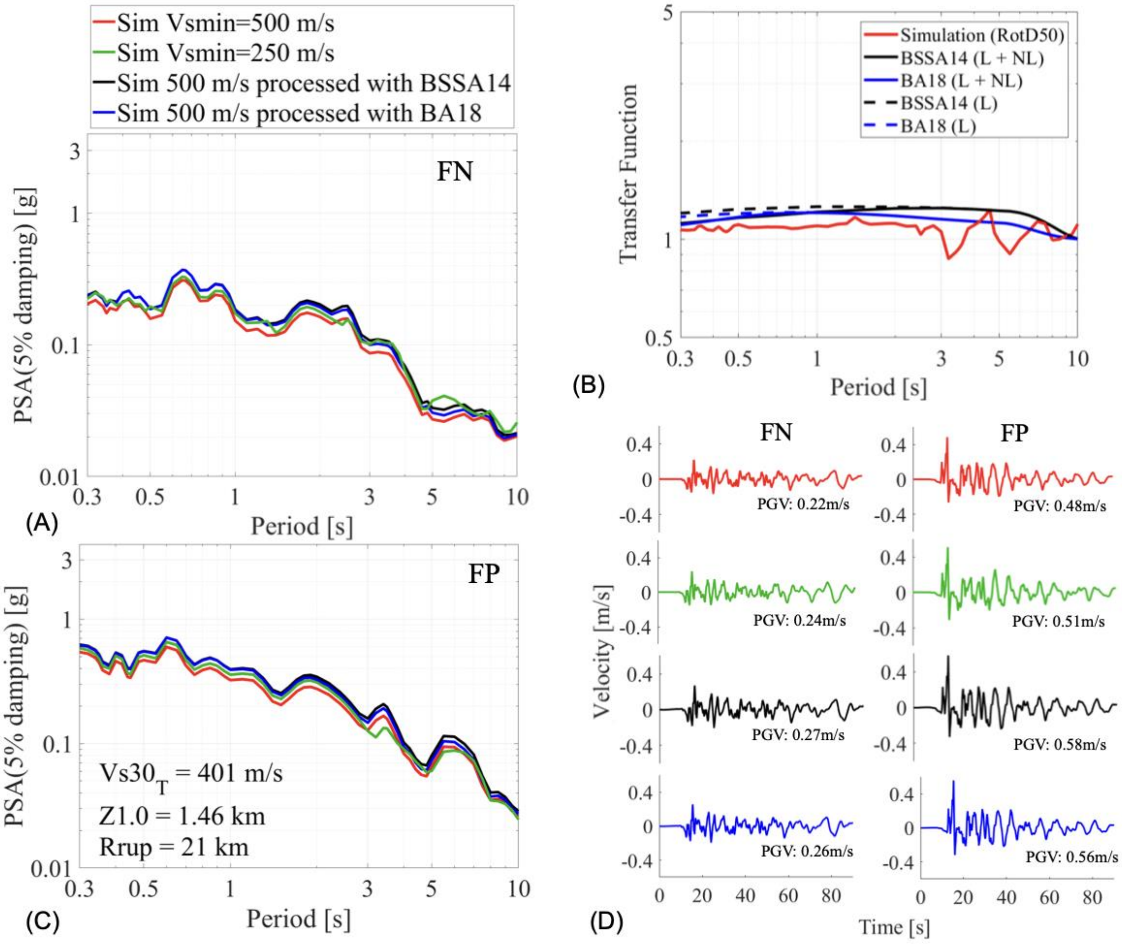

Figure 4.11. Site in the Pleasanton-Livermore Valley (PL) characterized by Vs30$_T$ = 401-m/sec, Z1.0 = 1.46-km and Rrup = 21-km. (A and C) PSA of the fault normal and fault parallel components; (B) empirical models' transfer functions accounting for both linear and nonlinear effects (blue and black solid lines) and linear effects only (blue and black dotted lines) and simulation models' transfer function (red solid line); (D) velocity time-histories of the fault normal and fault parallel components obtained from the different modeling approaches.

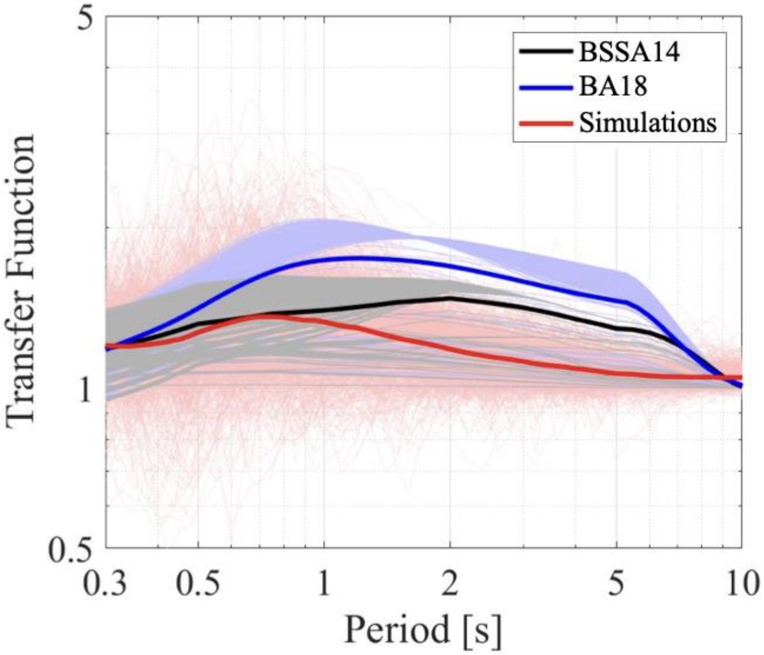

Figure 4.12. Transfer functions obtained with the considered modeling approaches (RotD50). The thin lines represent the transfer function at each site, and the thick line the median across all sites with $V_{S30} < 500\ m/sec$. Black and blue are used for the approach combining the simulations with $V_{s,min}$ = 500-m/sec with the BSSA14 and BA18 empirical factors, respectively, and red for the purely simulation-based approach.

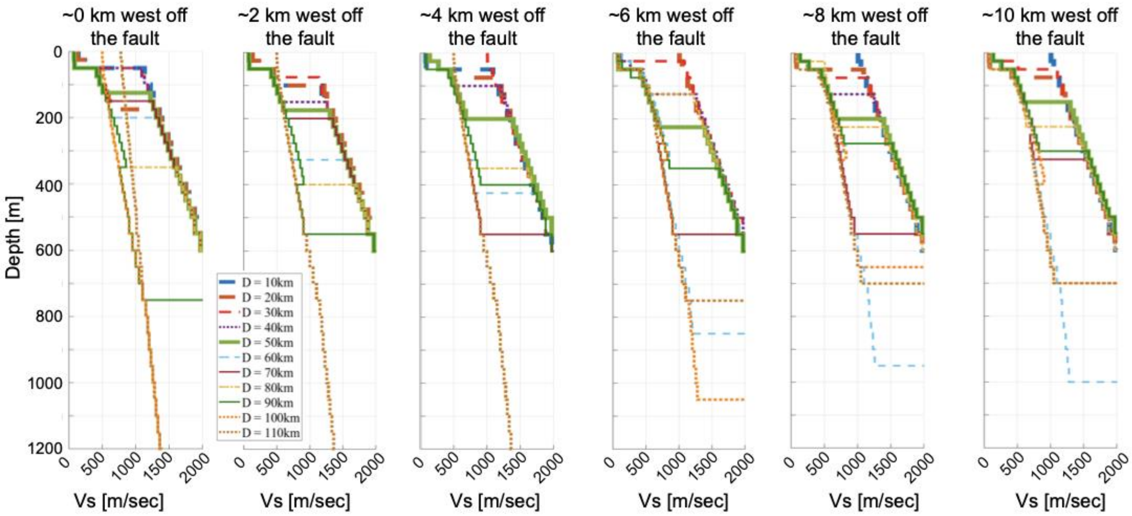

Figure 4.13. V_s profiles of arrays of stations sampled on a 10-km grid at increasing distances from the fault (from ~0-km to ~10-km) obtained from the USGS seismic velocity model (Aagaard and Hirakawa, 2021).

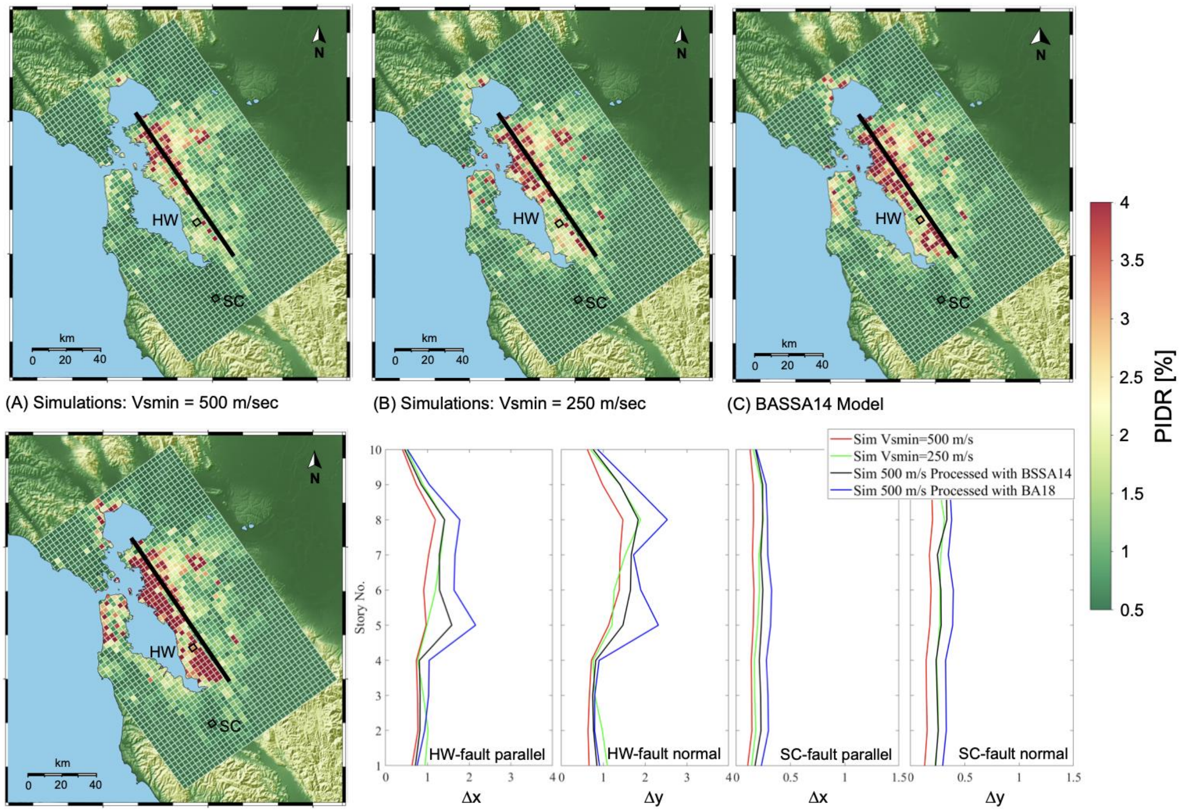

(A) Simulations: Vsmin = 500 m/sec (B) Simulations: Vsmin = 250 m/sec (C) BASSA14 Model

(D) BA18 Model (E) Drift envelopes at sites HW and CS

Figure 4.14. Ten-story building response maps. PIDR obtained from the different methods to model the soft soil. (A) Simulations with $V_{s,min}$= 500-m/sec; (B) Simulations with $V_{s,min}$= 250-m/sec; (C) Simulations with $V_{s,min}$= 500-m/sec processed with BSSA14; and (D) Simulations with $V_{s,min}$= 500-m/sec processed with BA18.

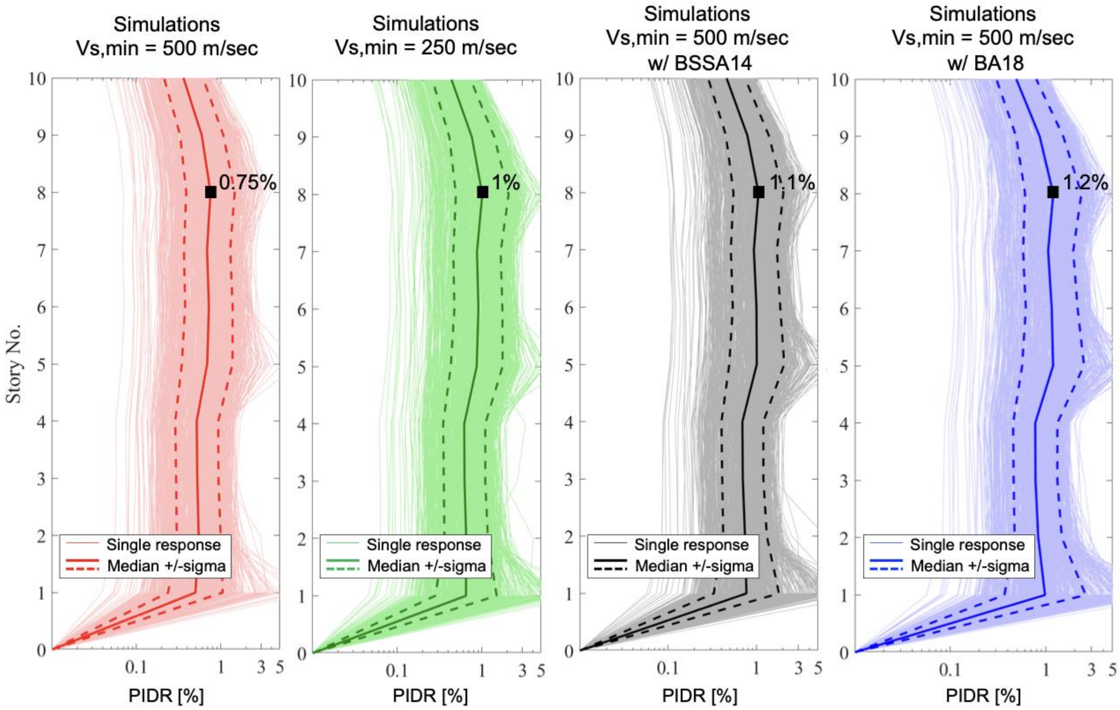

Figure 4.15. Distribution of the PIDR along the building height and across all modeling approaches and for the sites with $V_{S30} < 500\,m/sec$: response from single motion (thin lines), median and standard deviation (thick lines).

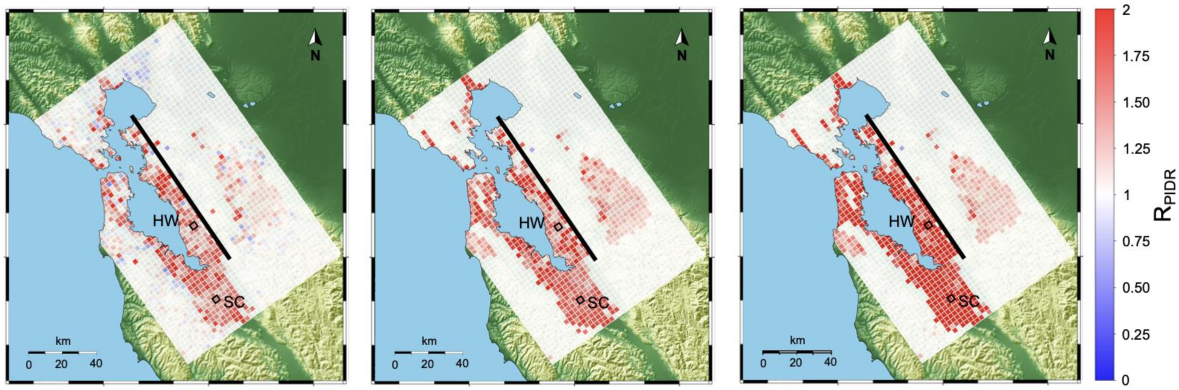

(A) $R_{IDR,Sim}$ = $PIDR_{Sim250}/PIDR_{Sim500}$ (B) $R_{IDR,BSSA14}$= $PIDR_{BSSA14}/PIDR_{Sim500}$ (C) $R_{IDR,BA18}$ = $PIDR_{BA18}/PIDR_{Sim500}$

Figure 4.16. Ratio maps (R_{PIDR}) of the ten-story building response obtained from the different modeling methods. (A) $PIDR_{Sim250}/PIDR_{Sim500}$, (B) $PIDR_{BSSA14/}PIDR_{Sim500}$, (C) $PIDR_{BA18/}PIDR_{Sim500}$

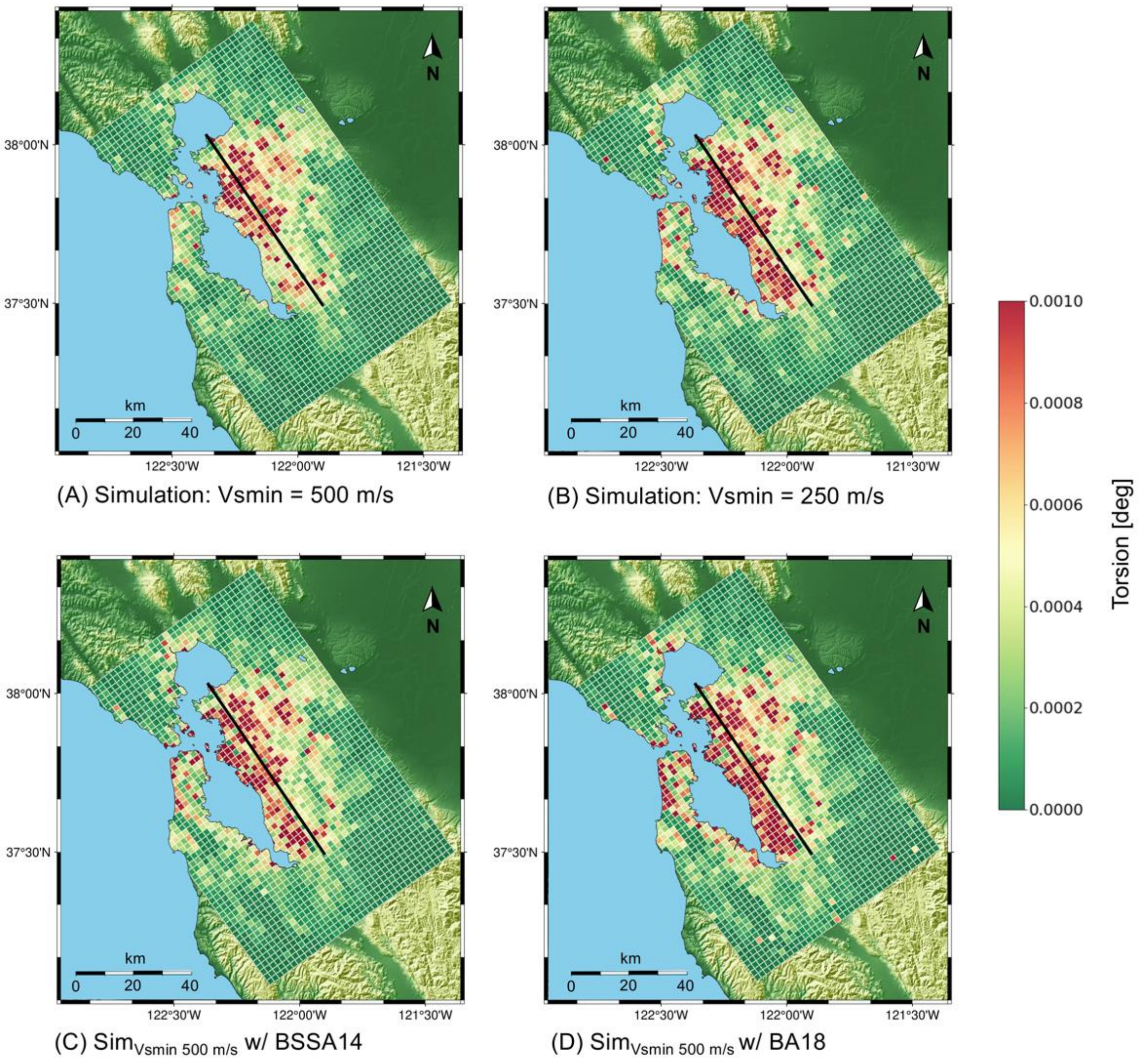

(A) Simulation: Vsmin = 500 m/s

(B) Simulation: Vsmin = 250 m/s

(C) $\mathrm{Sim}_{\mathrm{Vsmin\ 500\ m/s}}$ w/ BSSA14

(D) $\mathrm{Sim}_{\mathrm{Vsmin\ 500\ m/s}}$ w/ BA18

Figure 4.17. Map of torsion for the ten-story building. Peak torsion obtained from the different methods to model the soft soil. (A) Simulations with $V_{s,min}$= 500-m/sec; (B) Simulations with $V_{s,min}$= 250-m/sec; (C) Simulations with $V_{s,min}$= 500-m/sec processed with BSSA14; and (D) Simulations with $V_{s,min}$= 500-m/sec processed with BA18.

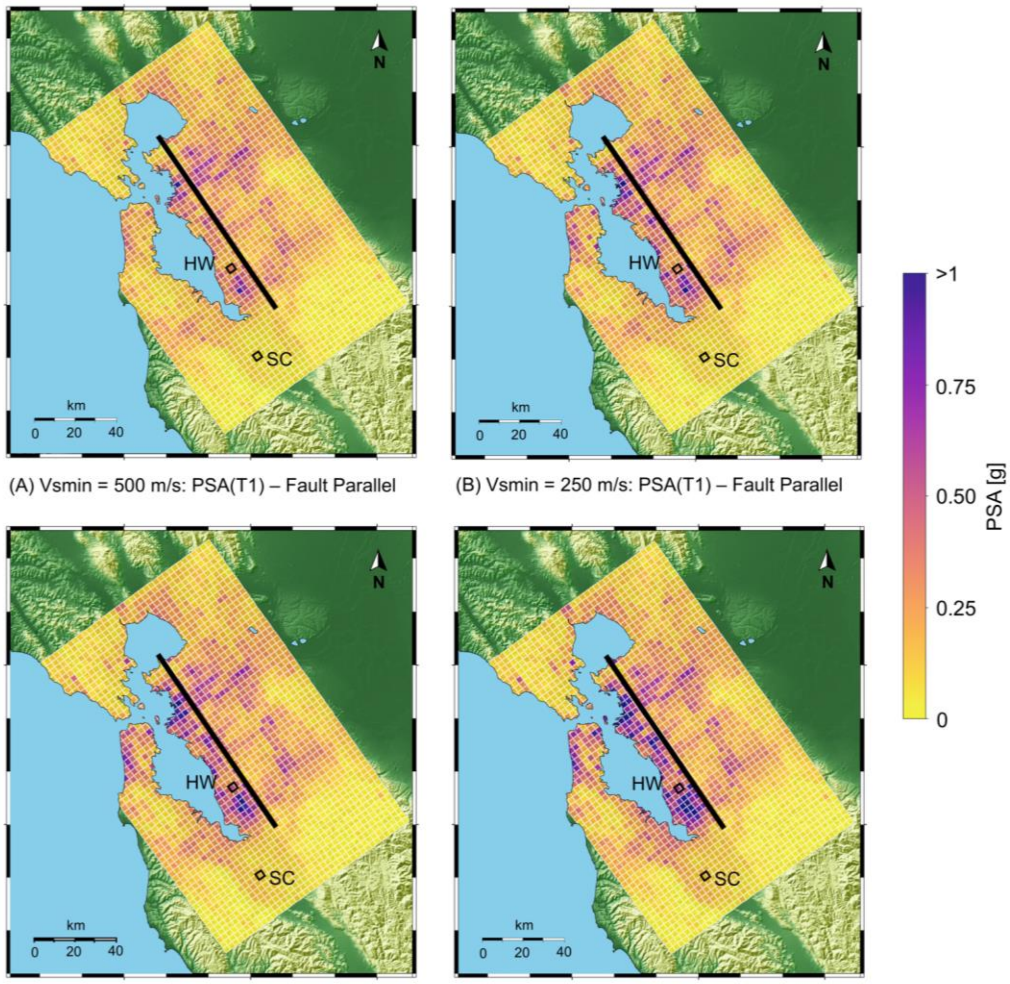

(A) Vsmin = 500 m/s: PSA(T1) – Fault Parallel

(B) Vsmin = 250 m/s: PSA(T1) – Fault Parallel

(C) BSSA14: PSA(T1) – Fault Parallel

(D) BA18: PSA(T1) – Fault Parallel

Figure 4.18. Pseudo-Spectral Acceleration at T1 - PSA(T1). Maps for the fault parallel component of the ground motions: simulation model with (A) $V_{s,min}$ = 500-m/sec and (B) $V_{s,min}$ = 250-m/sec; simulation model with $V_{s,min}$ = 500-m/sec processed with (C) BSSA14 and (D) BA18 to obtain the same V_{S30} calculated with $V_{s,min}$ = 250-m/sec.

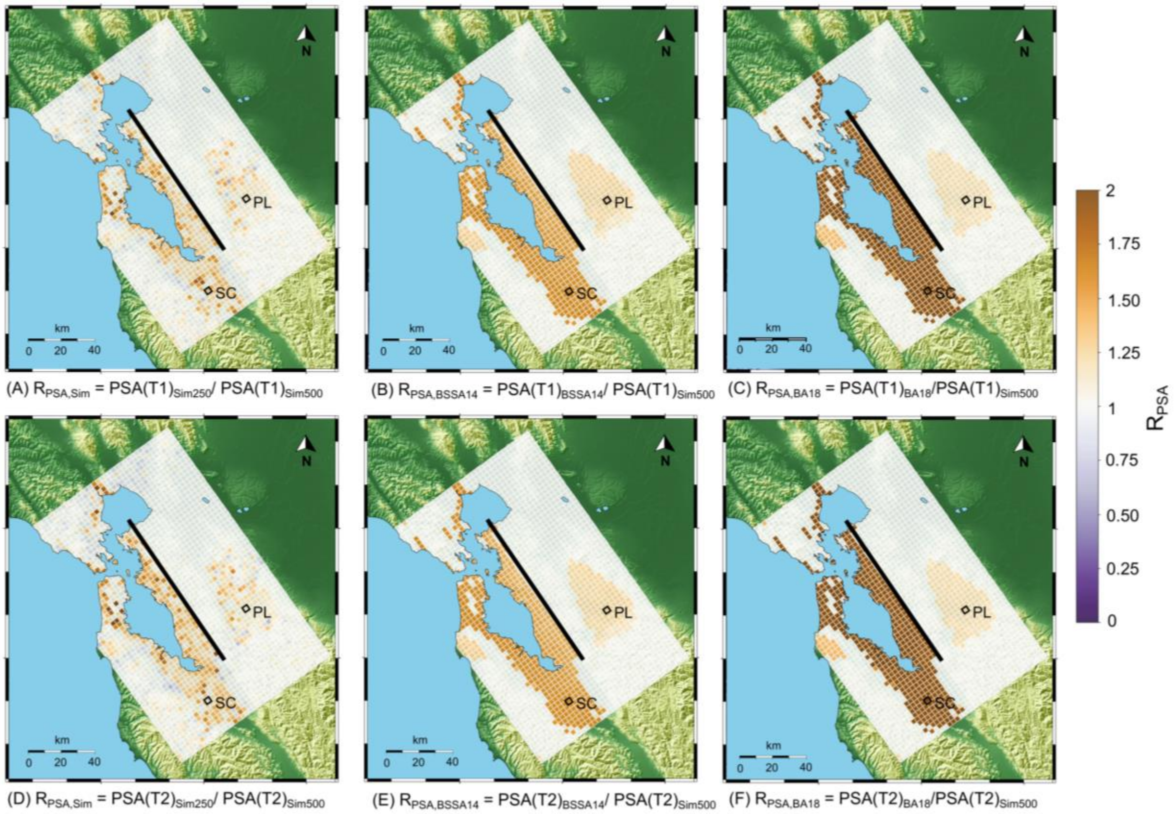

(A) $R_{PSA,Sim} = PSA(T1)_{Sim250}/ PSA(T1)_{Sim500}$ (B) $R_{PSA,BSSA14} = PSA(T1)_{BSSA14}/ PSA(T1)_{Sim500}$ (C) $R_{PSA,BA18} = PSA(T1)_{BA18}/PSA(T1)_{Sim500}$

(D) $R_{PSA,Sim} = PSA(T2)_{Sim250}/ PSA(T2)_{Sim500}$ (E) $R_{PSA,BSSA14} = PSA(T2)_{BSSA14}/ PSA(T2)_{Sim500}$ (F) $R_{PSA,BA18} = PSA(T2)_{BA18}/PSA(T2)_{Sim500}$

Figure 4.19. Pseudo Spectral Acceleration ratios (R_{PSA}) of the fault parallel component of the ground motions at the fundamental periods of vibration of the ten-story building (T1 = 1.7-sec and T2 = 1.5-sec): (A and D) PSA from the simulation model with $V_{s,min}$ = 250-m/sec to the PSA from the simulation model with $V_{s,min}$ = 500-m/sec; (B and E) PSA from the BSSA14 empirical model to the PSA from the simulation model with $V_{s,min}$ = 500-m/sec; and (C and F) PSA from the BA18 empirical model to the PSA from the simulation model with $V_{s,min}$ = 500-m/sec.

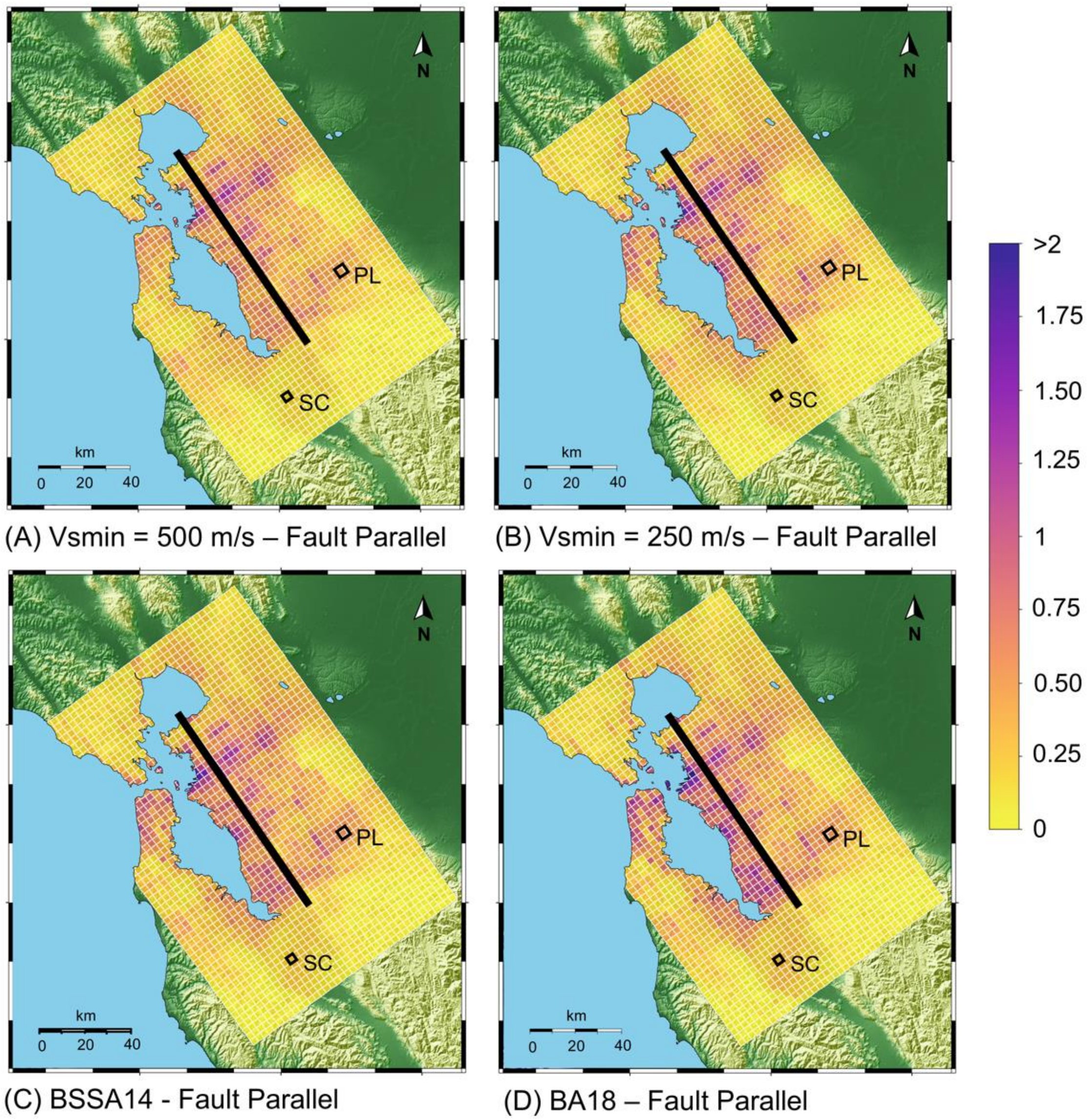

(A) Vsmin = 500 m/s – Fault Parallel

(B) Vsmin = 250 m/s – Fault Parallel

(C) BSSA14 - Fault Parallel

(D) BA18 – Fault Parallel

Figure 4.20. Peak Ground Velocity (PGV) maps for the fault parallel component of the ground motions: (A) simulation model with $V_{s,min}$ = 500-m/sec; (B) simulation model with $V_{s,min}$ = 250-m/sec; (C) simulation model with $V_{s,min}$ = 500-m/sec processed with BSSA14; and (D) simulation model with $V_{s,min}$ = 500-m/sec processed with BA18

5 SIMULATED GROUND-MOTIONS SELECTION FOR COMPONENT-SPECIFIC TARGET SPECTRAL AMPLITUDE AND VARIABILITY

This chapter of the dissertation is ready to submit in the journal of Earthquake Engineering and Structural Dynamics.

5.1 Introduction

Ground-motion selection is known as a significant and impactful step for nonlinear response-history analysis. Unsuitable selected earthquake records can cause bias in structural seismic performance evaluations. The selection procedure in the near field of major active faults is challenged by the scarcity of historical earthquake records [1,2]. Simulated ground motions obtained from three-dimensional physics-based wave propagation models have therefore emerged as a fundamental resource to inform seismic structural risk assessments for earthquake scenarios not well represented in the existing catalogs of records. The densely populated San Francisco Bay Area (SFBA) provides a good example of one of such regions where a large-magnitude event on the Hayward Fault is now expected at any time and for which consistent historical records are not available. Nevertheless, the region continues to witness the proliferation of structure and infrastructure construction [3].

Recent research has evaluated the performance of buildings and bridges subjected to the simulated ground motions and compared them with the existing historical real records [4–

6]. These studies determined the relevance of the utilization of site-specific synthetic earthquake motions, particularly in the near field.

Conventional ground-motion selection methods use spectral scaling and matching to approach target spectra [7]. As extensively discussed in the literature, scaling and matching can make records consistent with the targeted level of spectral amplitudes and shapes but significantly interfere with the frequency content, thus changing the seismic characteristics of the ground motions and affecting the resultant structural responses.

Moreover, sorting and selecting the ground motions based on the error calculated in approaching a mean target spectrum without any consideration for the target variance hinders the capability to properly assess the expected variability in the structural response.

This work proposes a methodology for the selection of simulated records to perform structural performance analyses when a large population of site-specific simulated ground motions is available. The proposed methodology defines component-specific target spectra for both amplitude and variability. This is done to address two key aspects in structural seismic assessments: (1) the first is related to the evidence that near-field ground motions tend to be highly polarized in the fault normal component, which is not properly addressed in current code-compliant ground-motion selection and scaling procedures; (2) the second concerns the variability of the ground motions at a site of interest, which should reflect the expected aleatory variability associated with the earthquake event(s) controlling the hazard but, if following current codes, it is simply a byproduct of records selection and scaling. The proposed method is herein demonstrated utilizing twenty-five realizations of an M7 strike-slip earthquake on the Hayward Fault. However, it remains valid for any (potentially larger) population of simulated motions.

5.2 Simulated Ground Motions

This study utilizes simulated ground motions obtained from twenty-five realizations of an M7 Hayward Fault strike-slip faulting mechanism event simulated over a 120-km x 80-km x 30km computational domain covering the San Francisco Bay Area (SFBA), as illustrated in Figure 5.1. The considered realizations differ from each other for the features of the rupture model including the distribution of the slip and location of the hypocenter, as shown in Figure 5.2. The simulations are performed in SW4 (seismic Waves, fourth order) within the EQSIM framework [8–10]. The rupture models adopt the Graves and Pitarka method [11]. The simulated ground motions obtained from the three-dimensional physics-based wave propagation model can resolve frequencies up to 5 Hz and employs the USGS 3D velocity model (v.21.1) with the minimum shear wave velocity of 250 m/s [12]. Five stations close to the fault were selected to demonstrate the proposed method.

It is notes that the twenty-five realizations utilized in this study are meant to only provide an initial estimate of the expected aleatory variability associated with an M7 strike-slip earthquake at the considered sites.

Table 5.1 summarizes the key information about the selected stations. According to the ASCE/SEI7 soil classification, the sites are located on dense soil, soft rock and rock. Table 5.2 indicates the impulsive characteristics of the simulated ground motions based on the algorithm proposed by Shahi and Baker [13]. The results in Table 5.2 show that between 50 to 70 percent of the considered synthetic ground motions are impulsive.

Figure 5.3 shows the comparison between the spectral acceleration predicted by four NGA-W2 ground-motion models (RotD50) versus the spectral acceleration of the single ground-motion components. The simulations are seen to fall within +/- one standard deviation of the empirical models, providing confidence in the utilization of the motions in the present study. It is also noted that the ground motions at the selected sites are, as expected, characterized by a pronounced polarization, with the spectral amplitudes in the fault normal component being larger than the amplitudes in the fault parallel component. This further supported the development of target spectra for the separate components.

5.3 Archetype Building Models

A ten-story reinforced concrete (RC) special moment resisting frame (SMRF) building is designed for a site in Berkeley, California. The SMRF RC building is designed following the provisions of ASCE7-22 and ACI 318 for risk category II. A three-dimensional model is developed in ETABS to design the building utilizing the modal response spectrum analysis. After defining structural element dimensions and detailing, a three-dimentional nonlinear structural model for the building was developed with OpenSees software. The columns and beams are modeled with force-beam column elements with five integration points and fiber sections [14,15]. Material nonlinearities are considered by utilizing Concrete-01 and Steel-01 materials in OpenSees. The parameters for confined concrete are derived based on the shear and flexural reinforcement detailing, following the model proposed by Mander (1988). Steel is characterized by 7% isotropic hardening. P-Delta effects are incorporated into the model. The damping matrix is constructed using Rayleigh damping for the 5% damping ratio. The fundamental periods of the model are T1 = 1.7 sec (X-direction), T2 = 1.5 sec (Y-direction) and T3 = 1.4 sec (Torsional mode).

The simulated ground motions are applied to the three-dimensional nonlinear structural model in OpenSees. The Y-direction of the building is aligned with the fault normal component of the ground motions, and the X-direction of the building with the fault parallel component. The drift is reported as the resultant drift calculated by the SRSS of the drift in the X and Y directions.

5.4 Six-step procedure for ground-motion selection

The proposed method for simulated ground-motion selection consists of six steps, as discussed below:

Step 1. Determine the site-specific design spectrum for the location and hazard level of interest.

Step 2. Compute the Component-Variability Ratio (CRV) vector based on the simulated ground motions available for the site of interest and for each direction (fault-normal and fault-parallel). This calculation is herein performed based on the twenty-five realizations presented in the previous section. However, the same approach can be followed for any (preferably larger) number of available two-component motions.

Step 3. Derive the median and standard deviation of the component-specific target spectrum by multiplying the CRV vector of medians computed in Step 2 by the target spectrum determined in Step 1. The median component-specific spectra so obtained are utilized as target spectra for the ground-motion selection; while the standard deviation of the target spectra (i.e., its variability) is taken equal to the variability of each component across all available realizations (twenty-five in this case study).

Step 4. Perform hazard disaggregation at the site of interest and, based on the event(s) governing the seismic hazard, modify the ground motions. This process entails the calculation of transfer functions for the spectral amplitudes based empirical ground motion models to obtain earthquake records with characteristics (M, Vs30, etc.) that are consistent with the hazard at the site(s) of interest.

Step 5. Randomly select m sets of simulated ground motions (e.g., each set is made of eleven motions if following the ASCE/SEI 7 provisions) and compute the normalized error resulting from the two ground-motion components (RNE) of mean and variance between the ground motions and the component-specific target spectrum. m should be large enough to allow finding the suite of motions with mean and variance that match the mean and variance of the target spectrum obtained in Step 3.

Step 6. Sort (from lowest to highest) the ground-motion sets based on RNE and check that the set of motions with the lowest RNE has a percentage of impulsive motions equal to the percentage from the full set of available motions (twenty-five).

In the following, each step is developed and discussed in more detail, utilizing the simulated ground motions and the structure presented in the previous sections as a case study.

5.4.1 Step 1: Determine the site-specific spectra.

The site-specific target spectra considered in this study are defined following the ASCE/SEI 7-22 provisions [16] for the deterministic maximum considered earthquake (MCER). The spectrum is herein obtained considering the geometric mean of the 84th percentile for four NGA-W2 empirical models, namely Abrahamson et al. (2014), Chiou and Youngs (2014), Campbell and Bozorgnia (2014), and Boore et al. (2014) [17–20]. The input parameters for the ground-motion models are determined based on the event controlling the hazard at the site of interest. The USGS hazard disaggregation tool [21] is utilized to this aim, considering a return period corresponding to the design spectrum at the fundamental period of the considered building (T = 1.5 sec). Table 5.3 summarizes the magnitude and distance of the Hayward fault earthquakes controlling the seismic hazard at the selected sites and Figure 5.3 shows the deterministic spectra for the five sites considered in this study.

5.4.2 Step 2: Compute the component-variability ratio (CVR).

The CVR_{ij} vector is calculated following the methods proposed by Zengin and Abrahamson [22], that is:

$$CVR_{i,k}^{j} = \frac{Sa_{i,k}^{H_j,sim}}{Sa_{i,k}^{RotD50,sim}} \tag{1}$$

where $Sa_{i,k}^{H_j,sim}$ is the spectral acceleration of the simulated ground motion i (with $i = 1,2 \dots 25$), in the direction j (1 = fault parallel and 2 = fault normal) and for the spectral period k; and $Sa_{i,k}^{RotD50,sim}$ is the spectral acceleration of the median horizontal ground motion across all nonredundant azimuths ($RotD50$) of the simulated ground motion i. The component-specific target spectrum $Sa_{i,k}^{H_j,sim,T}$ for each earthquake i is calculated as follows:

$$Sa_{i,k}^{H_j,sim,T} = CVR_{i,k}^{j} \times Sa_{i,k}^{D} \tag{2}$$

Where Sa_{i}^{D} is the spectrum determined in step 1.

As an example, Figure 5.5 shows the calculation of the component-specific spectra for three sites (A, C and D) and events (1, 2 and 19), demonstrating differences in the spectral amplitudes of the two ground-motion components.

5.4.3 Step 3. Derive the median and standard deviation of the component-specific target spectrum.

Once the calculation of $CVR_{ij,k}$ in step 2 is repeated for all twenty-five simulated earthquakes ($i = 1,2 \dots n$ with $n = 25$), the median and standard deviation of the component-specific spectra for each location are computed as follows:

$$\mu\left(Sa^{H_j,sim,D}\right)_k^j = \mu_k^j = \frac{\sum_{i=1}^{n} \log\left(Sa_{i,k}^{H_j,sim,T}\right)}{n} \tag{3}$$

where μ represents the median target spectrum for the component j and for the spectral period k (with $k = 0.3, 0.31 \dots p$ with p = 10), and the other symbols have the same meaning explained above.

The standard deviation of the component-specific target spectrum is simply calculated as:

$$\sigma\left(Sa^j\right)_k = \sigma_k^j = stdev[\log\left(Sa_{i,k}^j\right)] \tag{4}$$

where $Sa_{i,k}^j$ represents the spectral acceleration of component j, at spectral period k, for ground motion i.

Note that the distribution of the component-specific spectra will be characterized by a standard deviation calculated as $\sigma\left(Sa^{H_j,sim,D}\right)_k = \sigma_k = stdev[\log\left(Sa_i^{H_j,sim,T}\right)$, which simply reflets the variability of the polarization.

Figure 5.6 shows the median and standard deviation of the site and component-specific design spectra for the five considered locations.

5.4.4 Step 4: Process simulated ground motions (if needed)

Since the simulated motions utilized in this study are for an M7 earthquake and the events controlling the hazard are for larger magnitudes (Table 5.3), the motions are modified using the magnitude term from the NGA-W2 empirical models [17–20] Specifically, this is achieved by defining transfer functions $TFs_k = PSA_{T,k}/PSA_{O,k}$, where $PSA_{T,k}$ is the pseudo-spectral acceleration for the target magnitude at the spectral period k obtained from the four NGA-W2 empirical models, and $PSA_{O,k}$ is the pseudo-spectral acceleration for the original magnitude at the spectral period k. Tapering is applied to the transfer functions following the recommendations in Graves and Pitarka [23]. The factors so obtained are multiplied by the Fourier spectrum of each component of the original ground motions ($FS_{O,k}$), that is $FS_{T,k} = TFs_k \times FS_{O,k}$. Finally, the inverse Fourier transform is utilized to obtain the ground-motion time histories for a magnitude consistent with the event(s) controlling the hazard at the considered station.

Figure 5.7 illustrates the PSA of the RotD100 of the motions for the original (black) and target (green) magnitudes. The plots report both the single motions with thin lines and the median and standard deviation with thick lines. As expected, differences are minimal particularly at sites D and E where the target magnitudes are close to the simulated magnitude. The ground-motion processing is included in the proposed methodology to address all possible analysis scenarios. However, it should be noted that processing ground motions can be avoided if a sufficient number of simulated motions consistent with the event(s) controlling the hazard and the site conditions at the considered sites is available.

5.4.5 Step 5: Randomly select n sets of ground motions.

One hundred sets of eleven ground motions ($q = 1,2 \ldots m$, with $m = 100$) are randomly selected from the available poll of twenty-five simulations and NE is calculated for each component as follows:

$$NE_q^{j=1} = NE_q^{FP} = \sum_{k=1}^{p}\left[\left(\frac{{m_{q,k}}^{FP} - {\mu_k}^{FP}}{{\mu_k}^{FP}}\right)^2 + \left(\frac{{s_{q,k}}^{FP} - {\sigma_k}^{FP}}{{\sigma_k}^{FP}}\right)^2\right] \tag{5}$$

$$NE_q^{j=2} = NE_q^{FN} = \sum_{k=1}^{p}[\left(\frac{{m_{q,k}}^{FN} - {\mu_k}^{FN}}{{\mu_k}^{FN}}\right)^2 + \left(\frac{{s_{q,k}}^{FN} - {\sigma_k}^{FN}}{{\sigma_k}^{FN}}\right)^2] \tag{6}$$

$$RNE_q = \sqrt{{NE_q^{FP}}^2 + {NE_q^{FN}}^2} \tag{7}$$

where NE_q^{FP} and NE_q^{FN} are the normalized errors for the set q of eleven ground motions for the fault-parallel and fault-normal component, respectively; $m_{q,k}$ and $s_{q,k}$ are the mean and standard deviation of the ground-motion set q at spectral period k; μ_k and σ_k are the target mean and standard deviation at spectral period k, as derived in step 3 [note that the index j is not reported here since the two components are presented separately in equations (6) and (7)]; RNE_q is the resultant normalized error for the set q of ground motions.

The computation of the error can be performed across any bandwidth. If following the ASCE/SEI 7 provisions, the bandwidth of interest is $0.2T_1$ - $2T_1$, where T_1 is the fundamental period of the considered structure, and this is the approach followed in this case study. This process is then repeated $m = 100$ times, thus yielding one hundred values of RNE.

Figure 5.8 shows the final set of eleven motions with the minimum RNE (single motions, median and standard deviation in red); the full set of motions from the twenty-five realizations (median and standard deviation in black), and the component-specific deterministic spectrum (median and standard deviation). It is seen that the selected set of eleven records all approach the target amplitudes more closely than the full set of motions while preserving the variability of the full set of motions (twenty-five).

5.5 Structural Response

The two components (fault normal and fault parallel) of the simulated selected ground motions from the twenty-five realizations are simultaneously applied to the three-dimensional 10-story reinforced concrete building model presented earlier and the structural responses are recorded in both directions (X and Y). Specifically, the peak inter-story drift ratio ($PIDR$) is utilized as the reference engineering demand parameter. $PIDR = \max(\Delta_q)$, where $q = 1,2,..10$ is the number of stories, and $\Delta_q = \sqrt{\Delta_{X_r}^2 + \Delta_{Y_r}^2}$, with $r = 1, 2, 3, 4$ being the building corners, and Δ_{X_r} and Δ_{Y_r} are the drift ratios calculated along each component (X and Y) at each corner r. This process is repeated for each station. The median and standard deviation of the resultant PIDR obtained from the final set of eleven ground motions are compared with the statistics of the PIDR obtained from the full set of twenty-five ground motions. This comparison is demonstrated in Figure 5.9. The structural variability along the building height is substantially preserved for all sites, with medians reposes that are systematically larger than the responses obtained with the full set of motions, demonstrating the efficacy of the proposed model.

5.6 References

1. Smerzini C, Amendola C, Paolucci R, Bazrafshan A. Engineering validation of BB-SPEEDset, a data set of near-source physics-based simulated accelerograms. *Earthquake Spectra* 2023; **40**(1): 420–445. DOI: 10.1177/87552930231206766.

2. Petrone F, Abrahamson N, McCallen D, Pitarka A, Rodgers A. Engineering evaluation of the EQSIM simulated ground-motion database: The San Francisco Bay Area region. *Earthquake Engineering & Structural Dynamics* 2021; **50**(15): 3939–3961.

3. Mohammadi R, Motamed R, Faeli Z. Numerical Modeling of Soil-Shaft Interaction Validated Using the Instrumented Hayward Bridge in California. *DFI 48th Annual Conference on Deep Foundations*, 2023.

4. Matinrad P, Petrone F. ASCE/SEI 7-compliant site-specific evaluation of the seismic demand posed to reinforced concrete buildings with real and simulated ground motions. *Earthquake Engineering and Structural Dynamics* 2023; **52**(15): 4987–5009. DOI: 10.1002/eqe.3995.

5. Taslimi A, Petrone F. Informing the Seismic Risk Assessment of Distributed Infrastructure Using a Suite of Physics-Based Simulated Ground-Motion Realizations. *Structures Congress 2023 - Selected Papers from the Structures Congress 2023*, 2023. DOI: 10.1061/9780784484777.013.

6. Arsam T, Floriana P. Assessment of the Seismic Demands Posed to Suspension Bridges in the Near Field with Site-Specific Arrays of Simulated Ground Motions. *Journal of Bridge Engineering* 2024; **29**(5): 4024018. DOI: 10.1061/JBENF2.BEENG-6353.

7. Manfredi V, Masi A, Özcebe AG, Paolucci R, Smerzini C. Selection and spectral matching of recorded ground motions for seismic fragility analyses. *Bulletin of Earthquake Engineering* 2022; **20**(10): 4961–4987. DOI: 10.1007/s10518-022-01393-0.

8. Sjögreen B, Petersson NA. A fourth order accurate finite difference scheme for the elastic wave equation in second order formulation. *Journal of Scientific Computing* 2012; **52**: 17–48.

9. McCallen D, Petersson A, Rodgers A, Pitarka A, Miah M, Petrone F, *et al.* EQSIM—A multidisciplinary framework for fault-to-structure earthquake simulations on exascale computers part I: Computational models and workflow. *Earthquake Spectra* 2021; **37**(2): 707–735. DOI: 10.1177/8755293020970982.

10. McCallen D, Petrone F, Miah M, Pitarka A, Rodgers A, Abrahamson N. EQSIM—A multidisciplinary framework for fault-to-structure earthquake simulations on exascale computers, part II: Regional simulations of building response. *Earthquake Spectra* 2021; **37**(2): 736–761. DOI: 10.1177/8755293020970980.

11. Graves R, Pitarka A. Kinematic ground-motion simulations on rough faults including effects of 3D stochastic velocity perturbations. *Bulletin of the Seismological Society of America* 2016; **106**(5): 2136–2153.

12. USGS. Seismic Velocity Model 2020. https://www.usgs.gov/programs/earthquake-hazards/science/3-d-geologic-and-seismic-velocity-models-san-francisco-bay.

13. Shahi SK, Baker JW. An Efficient Algorithm to Identify Strong-Velocity Pulses in Multicomponent Ground Motions. *Bulletin of the Seismological Society of America* 2014; **104**(5): 2456–2466. DOI: 10.1785/0120130191.

14. McKenna F, Fenves GL, Scott MH. Open System for Earthquake Engineering Simulation. *University of California, Berkeley* 2000. https://opensees.berkeley.edu/.

15. Zhu M, McKenna F, Scott MH. OpenSeesPy: Python library for the OpenSees finite element framework. *SoftwareX* 2018; **7**: 6–11. DOI: https://doi.org/10.1016/j.softx.2017.10.009.

16. ASCE/SEI 7-22. *Minimum Design Loads and Associated Criteria for Buildings and Other Structures*. ASCE/SEI 7. American Society of Civil Engineers; 2021. DOI: 10.1061/9780784415788.

17. Abrahamson NA, Silva WJ, Kamai R. Summary of the ASK14 Ground Motion Relation for Active Crustal Regions. *Earthquake Spectra* 2014; **30**(3): 1025–1055. DOI: 10.1193/070913EQS198M.

18. Chiou BSJ, Youngs RR. Update of the Chiou and Youngs NGA Model for the Average Horizontal Component of Peak Ground Motion and Response Spectra. *Earthquake Spectra* 2014; **30**(3): 1117–1153. DOI: 10.1193/072813EQS219M.

19. Campbell KW, Bozorgnia Y. NGA-West2 Ground Motion Model for the Average Horizontal Components of PGA, PGV, and 5% Damped Linear Acceleration Response Spectra. *Earthquake Spectra* 2014; **30**(3): 1087–1115. DOI: 10.1193/062913EQS175M.

20. Boore DM, Stewart JP, Seyhan E, Atkinson GM. NGA-West2 Equations for Predicting PGA, PGV, and 5% Damped PSA for Shallow Crustal Earthquakes. *Earthquake Spectra* 2014; **30**(3): 1057–1085. DOI: 10.1193/070113EQS184M.

21. USGS. Unified Hazard tool 2017. https://earthquake.usgs.gov/hazards/interactive/.

22. Zengin E, Abrahamson NA. A procedure for matching the near-fault ground motions based on spectral accelerations and instantaneous power. *Earthquake Spectra* 2021; **37**(4): 2545–2561. DOI: 10.1177/87552930211014540.

23. Graves RW, Pitarka A. Broadband ground-motion simulation using a hybrid approach. *Bulletin of the Seismological Society of America* 2010; **100**(5A): 2095–2123.

Table 5.1. Characteristics of the considered stations.

Station	**RJB** [km]	**Rrup** [km]	**Vs30** [m/sec]	**Site class** (ASCE/SEI 7)	**Z1.0** [km]	**Z2.5** [km]
A	5.04	5.04	781	BC	0.46	3.38
B	0.45	0.45	552	C	0.18	1.10
C	0.63	0.64	1196	B	-	3.21
D	0.86	0.86	1196	B	-	3.08
E	1.54	1.55	502	C	0.6	1.02

Table 5.2. Impulsive motions.

Station	Shahi and Baker (2014)
A	12
B	17
C	18
D	14
E	16

Table 5.3. Hazard disaggregation based on the NSHM Conterminous U.S. 2018.

Station	M	Distance (km)
A	7.19	3.93
B	7.17	2.13
C	7.13	2.72
D	6.98	3.35
E	6.96	2.56

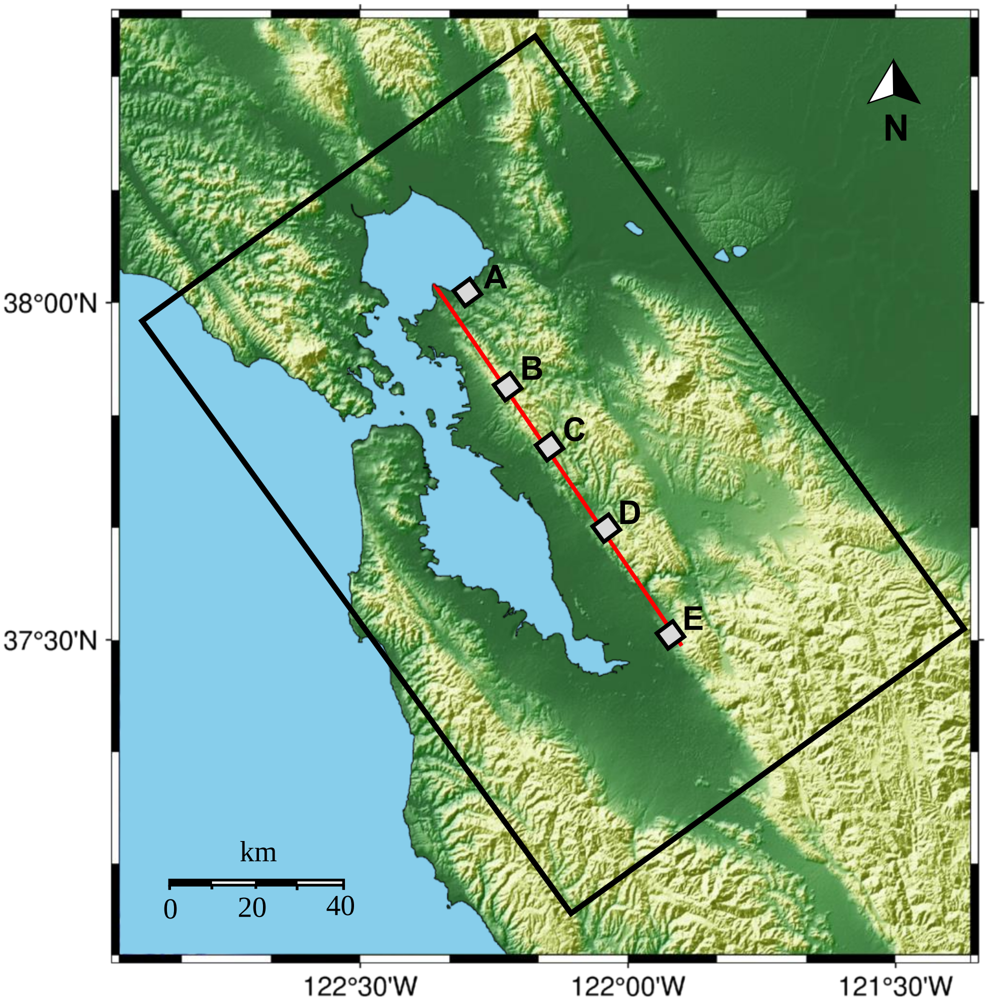

Figure 5.1. 80-km x 120km computational domain covering San Francisco Bay Area: the red line determines the Hayward Fault and the considered stations for the ground motion selection analysis.

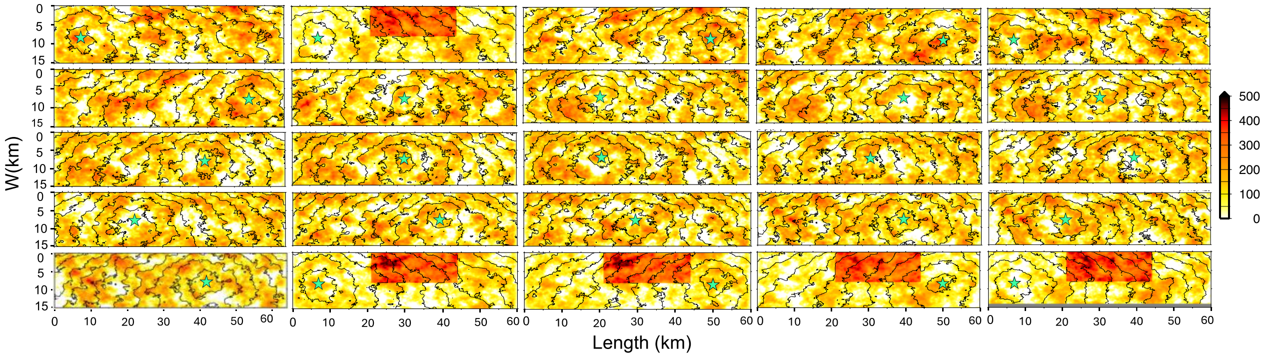

Figure 5.2. Slip distribution of the rupture models utilized for the twenty-five simulated realizations of a M7 earthquake. The green star indicates the location of the hypocenter.

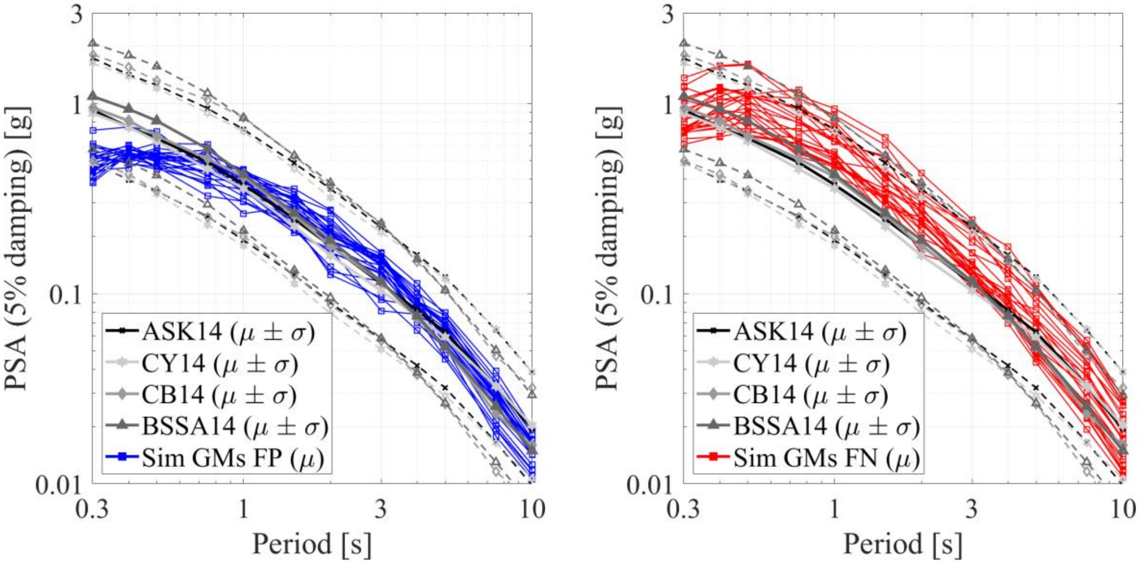

Figure 5.3. PSA of the simulated motions from the twenty-five considered events against the four NGA-W2 ground-motion models. Fault parallel (left); fault normal (right).

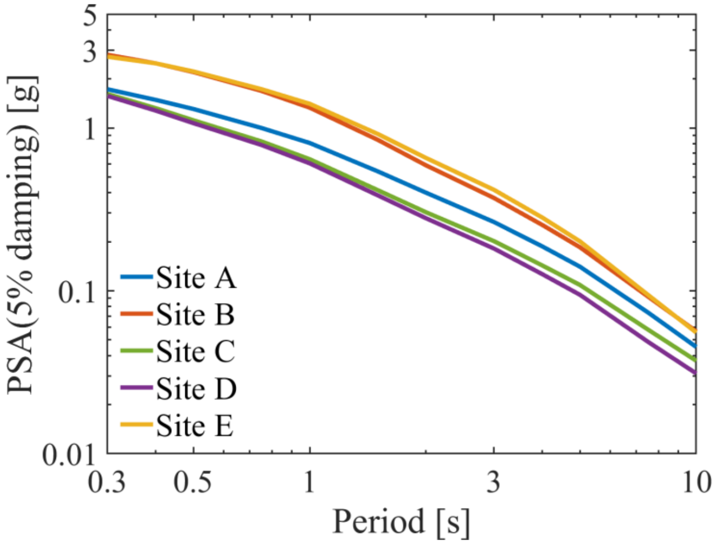

Figure 5.4. Site-specific design spectra for the sites considered in this study.

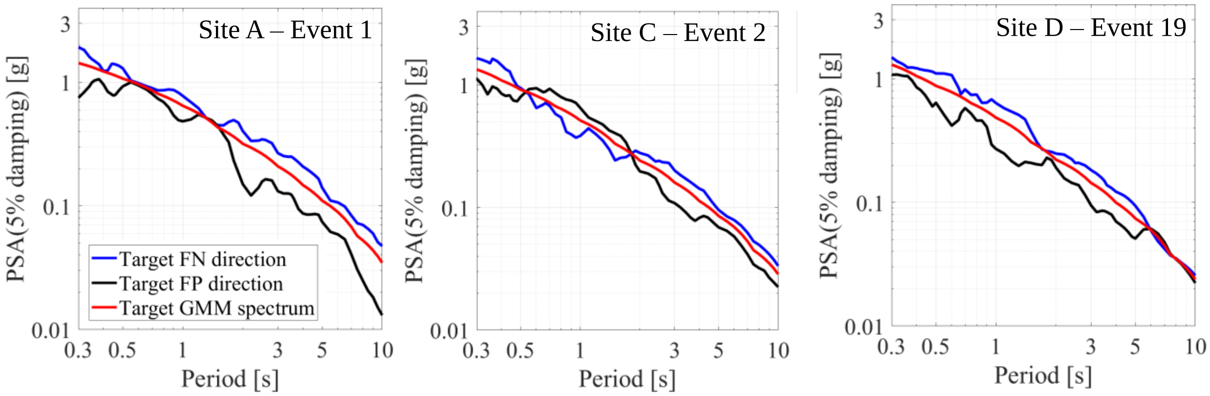

Figure 5.5. Component-specific target spectrum versus the actual spectral acceleration of the simulated ground motions for A) site A, Event. B) site C, Event 2. C) site D, Event 19.

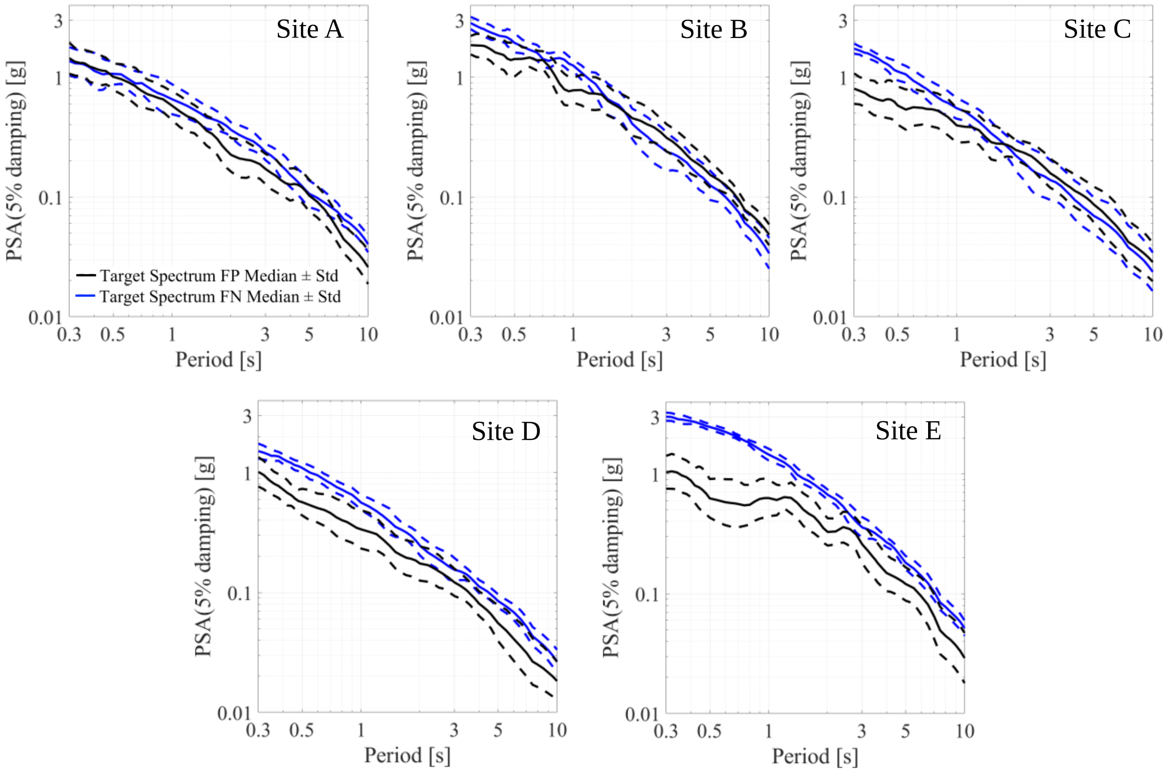

Figure 5.6. Component-specific target spectrum with calculated dispersion A) site A. B) site B. C) site C. D) Site D. E) Site E.

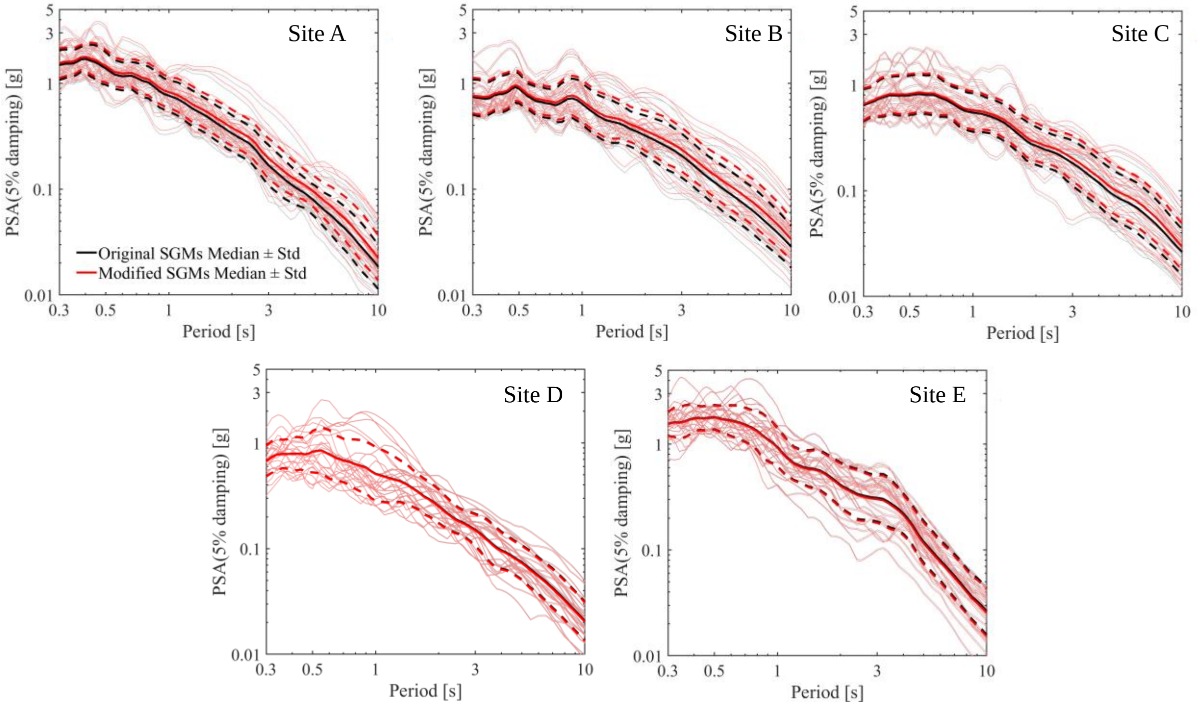

Figure 5.7. RotD100 of the original and processed simulated ground motions (single motions, median and standard deviation) across all sites.

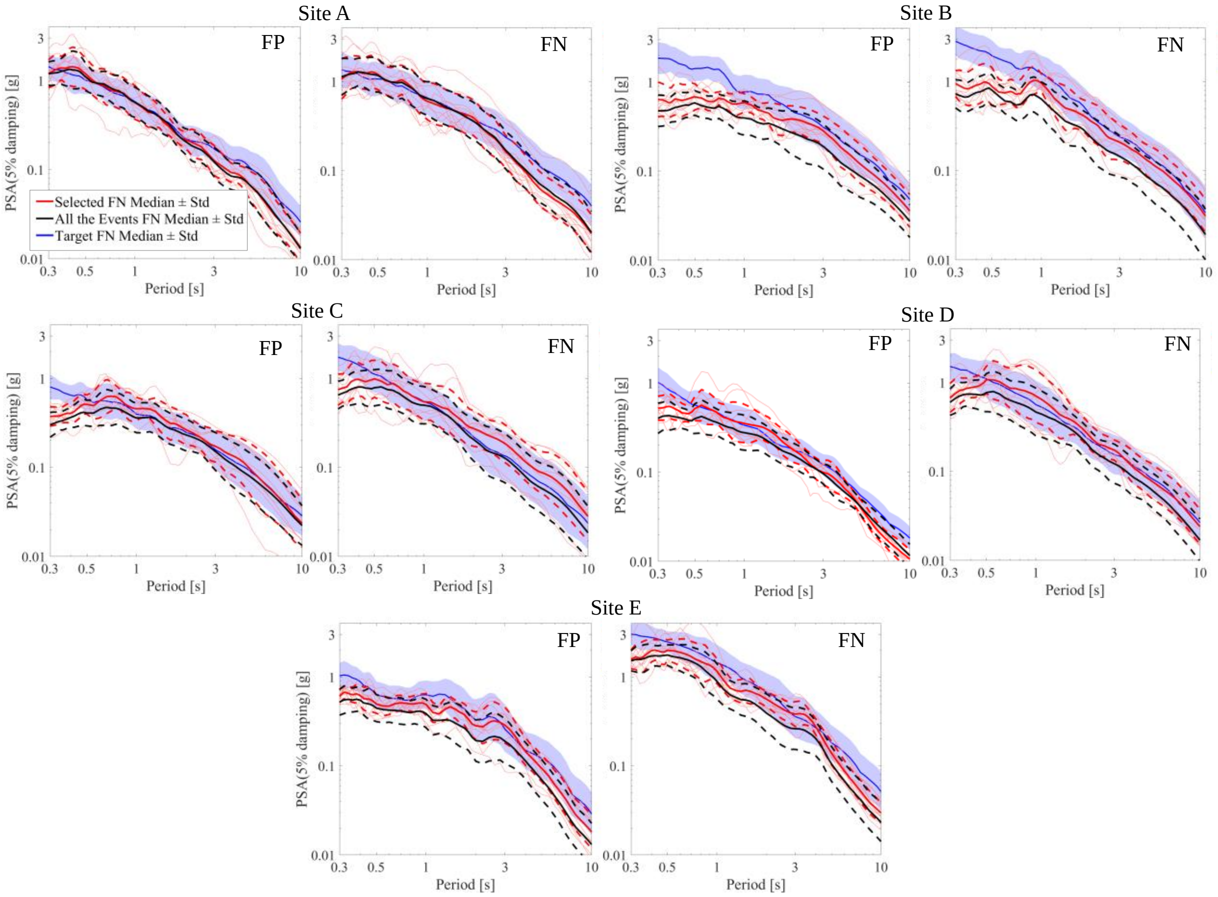

Figure 5.8. Set of eleven selected ground motions (single motions, median and standard deviation, in red); Set of original ground motions (median and standard deviation, in black); component-specific target spectrum (median and standard deviation).

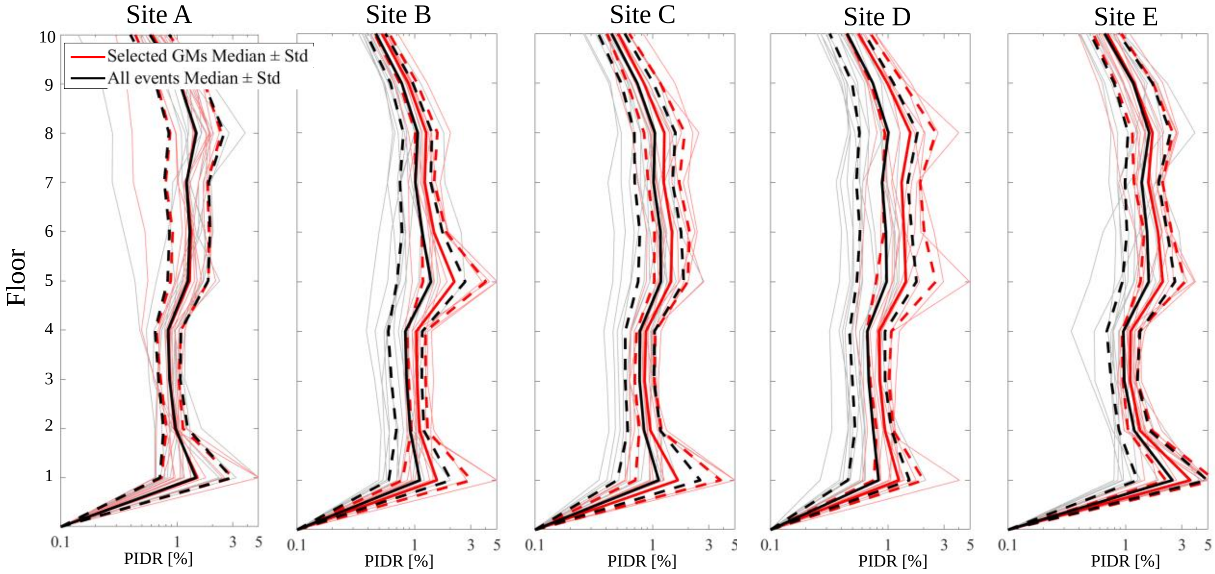

Figure 5.9. Comparison of structural response between the selected ground motions and entire the population of the records.

6 CONCLUSION

6.1 Key Observations and Concluding Remarks

This section offers a summary of the main research findings. A more detailed discussion can be found in the concluding sections of each chapter.

An integrated computational framework was developed in Python and MATLAB to conduct code-compliant site-specific building analyses across the San Francisco Bay Area. The structural demands obtained from the sets of real and simulated ground motions for a three-story and a twenty-story reinforced concrete building were compared in terms of median and dispersion of peak interstory drift and localization along the building height.

- Results show differences in the structural demands as large as by a factor of 1.5 (or above for selected sites), as either overestimate or underestimate of the (maximum) median values for both the low and high-rise buildings. Such differences are markedly site-specific and difficult to predict starting from the demand distributions obtained from historical records. Although site-specific procedures are utilized, a distance-dependent variation of the median demand calculated from the real motions is observed at stations characterized by similar site conditions. This is an effect of the criteria utilized for selecting the records based on magnitude, rupture distance, and site conditions, which lead to the utilization of similar sets of records that are scaled by factors that decrease at longer distances. On the contrary, the demand distributions obtained from the simulated ground motions, although scaled to match the same design spectra, are highly site-specific and not distance dependent. While forward-directivity effects can be incorporated with appropriate selection of the historical records, path and site-condition effects remain critical to capture.

- The analysis of the demand posed in the fault-normal and fault-parallel direction highlighted significant differences in the polarization and spectral shape between real and simulated motions. If following code-compliant methods for spectral scaling, this translates into spectral amplitudes that can be well below the target (or design) spectrum in one component and well above the design spectrum in the other.
- The fragility curves derived from a total of 30,552 nonlinear time-history analyses demonstrated a higher probability of exceeding extensive damage for the three-story building and complete damage for the twenty-story building when utilizing real ground motions rather than simulated ground motions. This points to a potential misestimate of structural responses obtained from records that do not necessarily reflect the conditions of the region and seismic event under consideration.

The analysis of the structural response at the regional scale took a step forward to (i) quantify the differences in structural response estimates introduced by the explicit modeling of soft sediments; and (ii) assess the efficacy of less computationally intensive approaches for modeling soft soil. Two simulation models characterized by a minimum resolved shear wave velocity of 250 and 500 m/sec were utilized, and the ground motions resolving 500 m/sec were processed with empirical site amplification factors. This analysis was demonstrated on a three-dimensional mid-rise reinforced concrete building.

- Results show differences in the prediction of the ground-motion intensity measures and building responses at the sites with a Vs30 directly affected by the computational cap on the $V_{s,min}$ and, noteworthy, at the sites in their vicinity.
- Appropriate tapering functions, specific to the amplification expected in the geological structures of the region under consideration must be derived if methods that combine physics-based simulations and empirical models are employed.
- At the sites not directly affected by the cap on the $V_{s,min}$ and located in the vicinity of soft sites, differences arise from wave-propagation phenomena across soft and stiff layers that can be fully captured only by the simulation-based approach in which low shear-wave velocities are modeled. The site-specificity of ground-motion amplitudes is partially preserved when simulated motions are corrected with empirical factors.

The findings summarized above motivated the definition of a ground-motion selection method for large populations of site-specific physics-based simulated motions. This method derives component-specific target spectra that incorporate both amplitude and variability to preserve seismic characteristics, structural response variability, and polarization of the motions, with consideration of the impulsive characteristics of the motions. Specifically, code-compliant target spectra are modified to explicitly incorporate ground-motion polarization, and a target variance is imposed by utilizing the dispersion of the ground-motion intensity measure(s) of the site-specific simulated motions as representative of the expected aleatory variability. The proposed method is demonstrated on the three-dimensional ten-story reinforced concrete building.

- Results show that the proposed method can yield a population of site-specific simulated ground motions that approach target amplitudes and variability.
- Structural responses obtained with a set of eleven simulated motions (ASCE/SEI 7) are seen to have the same variability that would be obtained if the full population of available simulated motions (twenty-five in this study) was utilized, while preserving the amplitudes associated with the target spectra.

6.2 Future Work

The following is a short summary of topics related to the research presented in this dissertation that should be considered for further investigation:

- Analyses of the type presented in this study should be extended to a larger population of simulated motions to better understand and capture the expected aleatory variability at the sites under consideration. This must incorporate the consideration of ground-motion simulation parameters that lead to extreme yet realistic earthquake scenarios.
- A larger portfolio of structures and infrastructure should be considered to conduct comparative studies that utilize real and simulated motions.
- Non-ergodic GMMs specific to the region under consideration should be utilized to inform the derivation of more accurate transfer functions. This will allow to further investigate the efficacy of methods that combine physics-based simulations and empirical factors.

- 1D wave propagation solutions should be utilized for the derivation of region-specific tapering functions and their accuracy should be tested against 3D numerical solutions.
- The analyses of the type presented in this dissertation should be extended to other seismic active regions to provide a broader basis for fully informing the utilization of simulated ground motions in engineering domains.